UNICA

UNIVERSITÀ
DEGLI STUDI
DI CAGLIARI

Ph.D. DEGREE IN
Physics
Cycle XXXV

TITLE OF THE Ph.D. THESIS

Degradation studies on different pigments and binders: new approaches to diagnostics in cultural heritage

Scientific Disciplinary Sector(s)

FIS/07

Ph.D. Student:	Francesca Assunta Pisu
Supervisor	Daniele Chiriu
Co-Supervisor	Carlo Maria Carbonaro

Final exam. Academic Year 2021/2022
Thesis defence: March 2023 Session

CONTENTS

INTRODUCTION

Studying the state of degradation, alteration and conservation of an artwork is the starting point of a restoration process. This first step is commonly known in the field of cultural heritage as "diagnostics".
A careful diagnosis allows choosing the best restoration approach for a sample under examination. The diagnostics of an artwork permits not only a complete characterization of materials realized by an artist, but also the identification of the degradation products generated over time. These are often due to different causes: physical, chemical, and biological. Finally, a good choice of the employed techniques allows also dating and authentication purposes.
A diagnosis can be made in invasive or non-invasive ways: this depends on the techniques available and on what kind of information the experts want to emphasize. The first choice is always a non-invasive approach, obtainable with different analytical techniques such as Raman spectroscopy, X-ray fluorescence, multi-spectral imaging, and luminescence. Sometimes it is necessary to follow a succession of a first non-invasive diagnostic step and then an invasive one. The latter requires a micro-sampling from the object under examination, to obtain, for example, a given stratigraphy, date the artwork, or confirm the data obtained from the first non-invasive step of investigation.
Therefore, the diagnosis is translatable into the implementation of two actions: 1) the choice of appropriate diagnostic methodologies, and 2) the interpretation of the obtained results. The former grants the constant need of developing new non-destructive and non-invasive methodologies of analysis for cultural heritage.
We will try to conduct this purpose in the overall thesis, and in particular in chapter 3, where the first studies on a new stratigraphic analysis method will be presented. This work is carried out in collaboration with the research centre FORTH (Crete) and it is based on the photoacoustic effect coupled with SORS (Spatially Off-set Raman Spectroscopy). It will be tested on artificial frescoes mock-ups and on real frescoes fragments, in order to obtain compositional information and stratigraphic imaging on the samples. This is the first time that the technique has been used for stratigraphic imaging, and its totally non-destructive and non-invasive implementation is the final goal of our future studies.
The interpretation of the experimental data requires a prior and comprehensive knowledge of the materials used and their alteration state. It is not possible to make a definitive diagnosis if there is not the

complete knowledge about the materials under analysis. In addition, different environmental conditions lead to diverse alteration products, so the identification of the latter is the essential point to understand what happened to an heritage object and understand how to preserve it. Therefore, it is necessary to carry out studies aiming at obtaining as much information as possible on the process of degradation of each single element that constitutes the work under examination. In our case the study we focused our attention on the pictorial layer.
From here comes the intent of facing selective degradation studies on different pigments (calcium hydroxide, CdS, HgS) to help in the exhaustive knowledge of the degradation path of pigments, responsible for chromatic alterations in paintings. As previously stated, the degradation path is linked to the altering agents to which the work is subjected and their effects manifest over time.
By monitoring in accelerated protocols the kinetics in which the chemical reactions take place, we can develop new diagnostic non-invasive procedures aimed at dating purposes. In chapter 1, it will be shown an example of construction of dating model starting from the kinetics of alteration of calcium hydroxide, obtained with the use of Raman spectroscopy.

The main intent of this work is to expand the diagnostic research both from a descriptive point of view for the degradation process of the painted surface, and from the point of view of new approaches and methodologies for diagnostics. For what concerns the first one, we worked with two main purposes: kinetics studies in the case of San Giovanni white with the help of a non-invasive technique, presented in chapter 1; and the characterization of the degradation path and individuation of the respective alteration products in the case of Red vermilion and Cd-pigments in chapter 2, always favouring the choice of a non-destructive techniques, conventional or not, such as non-linear optics. Regarding the development of new approaches and methodologies, it will be presented in chapter 3 dedicated to the photo-acoustic method coupled with SORS as a new tool for stratigraphy analyses.

This thesis derives from the reworking of several articles and original works.

- In detail, chapter one is based on:
  - Francesca Assunta Pisu et al. "Defect Related Emission in Calcium Hydroxide: The Controversial Band at 780 cm^{-1}". In: Crystals 10.4 (2020). issn: 2073-4352. doi: 10.3390/cryst10040266
  - Francesca Assunta Pisu et al. "Fresco Paintings: Development of an Aging Model from 1064 nm Excited Raman Spectra". In: Crystals 11.3 (2021). issn: 2073-4352. doi: 10.3390/cryst11030257
- The second chapter is based on:
  - Francesca Assunta Pisu et al."Degradation of CdS Yellow and Orange Pigments: A Preventive Characterization of the Process through Pump–Probe, Reflectance, X-ray Diffraction, and Raman Spectroscopy". In: Materials(2022), doi: 10.3390/ma15165533;
  - Francesca Assunta Pisu et al. "Transient absorption study on Red Vermilion darkening in presence of chlorine ions and after UV exposure". In: analitical Chemistry, (2022), doi: 10.1016/j.jphotochem.2022.114291.
- The third chapter is based on:
  - Francesca Assunta Pisu et al." Stratigraphy of ancient frescoes: a new approach with photoacoustic and SORS imaging ". In:Journal of Imaging , (2023), doi: 10.3390/jimaging9010016.

1 CARBONATION OF CALCIUM HYDROXIDE

Fresco technique boasts ancient origin in centuries of history [1]. It was already known during the Aegean civilization, and the oldest surviving fresco paint is dated as approximately in 1600 B.C. The technique was also used by Greeks, Etruscans, Romans, and during the middle-ages. As shown by numerous and famous artworks, the fresco was one of the most employed painting techniques. The fresco is one of the most durable painting arts because the pigment is linked to the lime wall when the latter is still wet [2, 3]. The drying process is related to the carbonation of calcium hydroxide, the main component of the substrate.

The fresco paint consists of several layers, mainly three of which can be identified: the rinzaffo, the arricio and the velo.

The rinzaffo is a smoothed layer of mortar, consisting of rather coarse

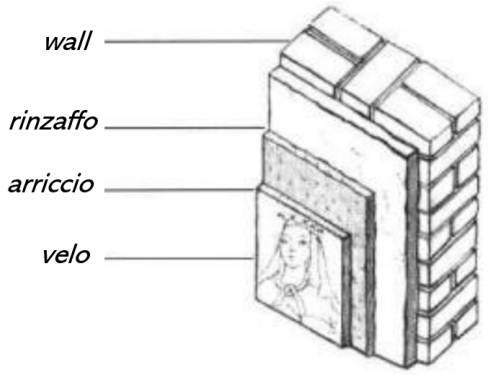

Figure 1: Fundamental layers of a fresco.

sand, that can extend from one to two centimetres. extend from one to two centimetres. It is spread directly on the wall with the help of a trowel and must appear slightly smooth and grainy to the touch, so that the next layer, the next layer, the arriccio.

The arriccio must be applied with a thickness of a few millimeters when the rendering is dry. The mortar used has the finest sand grains, it also has pozzolan or baked clay finely sieved. On this layer, the preparatory drawing is made. The "velo" is then applied, a very fine layer like a film, whose mortar may present marble dust to make the surface smoother.

The velo, also called tonachino or intonachino is the real pictorial support, the one on which the fresco colour will be applied, it's spread with variable thickness ranging between 100 and 400μm, When it was

applied on the arriccio, being fine and still fresh, it was possible to detect the underlying layer, hence the preparatory drawing, which was used by the artist as an aid to spread the colour.

Calcium hydroxide, well-known by the term "hydrated lime", reacts with the carbon dioxide, taken from air and water, leading to the formation of calcium carbonate. We can summarize the process with the following Equation (1):

$$\begin{aligned} CaCO_3 + heat &\rightarrow CaO + CO_2 \\ CaO + H_2O &\rightarrow Ca(OH)_2 \\ Ca(OH)_2 + CO_2 &\rightarrow CaCO_3 + H_2O \end{aligned} \tag{1}$$

The carbonation process of lime on painted walls is a crucial phenomenon in fresco artworks, and it is of paramount importance in the conservation field to consider it both for diagnostic and dating purposes. The kinetics of carbonation process were studied by several authors. Camerini et al. [4] suggested a kinetic model based on surface boundary nucleation followed by growth and penetration in depth: the carbonation starts on the surface of the particles (grain boundary nucleation) and grows along the particles surface, eventually covering them; finally, carbonated regions coalesce from adjacent particles. Montes-Hernandez et al. [5] studied the carbonation process of commercial lime in high pressure-temperature conditions and proposed a carbonation model described by a pseudo-second-order kinetic model. They noted also the earlier formation of amorphous $CaCO_3$ followed by calcite. Later on, they examined the intensity variation of OH-stretching band in the absorption spectrum during the carbonation process, obtaining a good agreement with the proposed pseudo-second- order model [6]. In addition, Rodriguez-Navarro [7] studied the carbonation process of nano-limes in humid air at room temperature. In this case, the carbonation process involves the initial formation of amorphous calcium carbonate before the final calcite. The model proposed was a first order kinetic. In [8], the carbonation of $Ca(OH)_2$ in humid N_2 was studied at 60–90°C, and it was well described by an asymptotic equation assuming chemical reaction control and considering the surface formation of calcium carbonate clusters on calcium hydroxide pores.

Taking into account that these kinds of artworks are in most cases unmovable, unique, and unrepeatable relics, to develop a dating model for frescoes the use of a portable, non-invasive, and non-destructive technique, such as Raman spectroscopy, is the best choice. Indeed, the exploitation of a portable Near Infrared (NIR) -Raman technique revealed high potential in its usefulness in a cultural heritage field [9–12], and it was previously proposed to study the ag-

ing model of ancient paper [13] and pigments [14]. So, the aim of this work consists of developing a dating model for frescoes and wall paintings using information on carbonation processes obtained from the Raman spectrum of the fresco binder.

In order to develop this study, a complete characterization of the Raman spectrum of the phases involved is necessary, however calcium hydroxide exhibits a controversial band at 780 cm^{-1} whose attribution is still debated, mainly because of the excitation dependence. The behaviour of this band appears correlated to the carbonation process, since its intensity presents a progressive decreasing as the time increases, whilst at the same time the formation of the typical band at 1087 cm^{-1} of calcium carbonate is observed [15]. This particular trend can be clearly associated to the reaction of slaked lime to the environmental atmosphere. For this reason, the mentioned band elicited our attention as a specific marker for those processes in which a reaction driven by environmental conditions takes place. That is the case of frescoes or paintings and in general Cultural Heritage $Ca(OH)_2$-containing relics where a possible degradation should be monitored.

In the literature there are several hypotheses on the 780cm^{-1} band formation in the Raman spectrum of calcium hydroxide.
For example Schmida and Dariz [16] studied the Raman and luminescence spectra of CaO, Ca(OH)2 , and $CaCO_3$ with three different excitation wavelengths (514.5 nm, 632.8 nm, and 784.8 nm) and excluded the vibrational nature of this band, hypothesizing a luminescence effect derived by impurity (rare earth) elements. On the same grounds, other authors [17] investigated the fluorescence of some calcium minerals, correlating the above mentioned band to rare earth impurities associated with a particular structure or phase of this compound. Chaix-Pluchery et al. [16, 18] studied the Raman spectrum of calcium hydroxide ($\lambda_{exc} = 514nm$) at different temperatures and identified the formation of a luminescence band around 1650 cm^{-1} (that is, 562 nm) [18], but no evidence could be found in their spectra of the 780cm^{-1} band. The possibility that this band derives from the luminescence of unreacted CaO or from a carbonation product ($CaCO_3$) was also considered. Actually, the luminescence properties of CaO are well known, and they show a luminescence band out of the above-mentioned luminescence range recorded for hydroxide [19]. On the other hand, a study of calcite luminescence [20] suggests that the emission recorded in the UV range, much more energetic than the one observed in calcium hydroxide, could be related, once again, to the presence of Mn_2^+ , Ce_3^+ , or Eu_3^+ ion impurities [21]. From the reported results, it is clear that the possible presence of impurities in the compounds involved in the calcination cycle could be the origin of the emissions recorded in the near infrared (NIR) range under 1064 nm laser excitation.

Another possibility is the formation of some kind of defects during the carbonation/calcination cycle itself. Indeed, depending on the environmental conditions (humidity and temperature), the cycle could re-start and proceed. Dubina et al. [22] reported that the lime conversion to calcium hydroxide and its subsequent carbonation strongly depends on the relative humidity (RH) at which the samples are held for 24 h in moist air at 80°C. Below 20% RH, the lime converts to portlandite without carbonation, while for a higher RH concentration the partial carbonation becomes relevant. However, the conversion process and its connection, if any, to the origin of the mentioned bands, is not ascertained.

In order to discriminate the origin of this band, assigning it to a definite luminescent or vibrational conclusive feature, the fist step of this work presented in next section consists in the characterization the lime paste by analyzing Raman spectra excited with visible and NIR excitations and carrying out different thermal treatments of the samples, also under different environment conditions, to support the assessment of a luminescence defect related to the carbonation/calcination cycle. A complete understanding of the nature of this band can be useful in the field of Cultural Heritage for dating purposes, as well as to determine the conservation state of mural relics to prevent the possible activation of degradation processes.

The second step will focus on developing a kinetic model of the carbonation process, evaluating the relative variation of the two Raman bands associated with the hydrate and carbonate phase over time, looking for a match with carbonation kinetics previously demonstrated in the literature.

1.1 MATERIALS AND METHOD

1.1.1 Analytical methodology

To construct a kinetic model on the carbonation process of $Ca(OH)_2$ based on its Raman spectrum, two basic steps will be followed. The first step is to characterize the nature of the band at $800 cm^{-1}$ found in the literature and in industral calcium hydroxide (synthesis involving a storage time). We proceeded with its synthesis starting with marble powder, heated it up to 1000°C, and then hydrated the CaO produced with distilled water. The sample obtained does not show the aforementioned band. In order to speed up the drying process and eliminate the presence of unbound water in the Raman signal, we subjected the sample to different heat treatments and in different environments to verify the role played by gases such as CO_2 and O_2

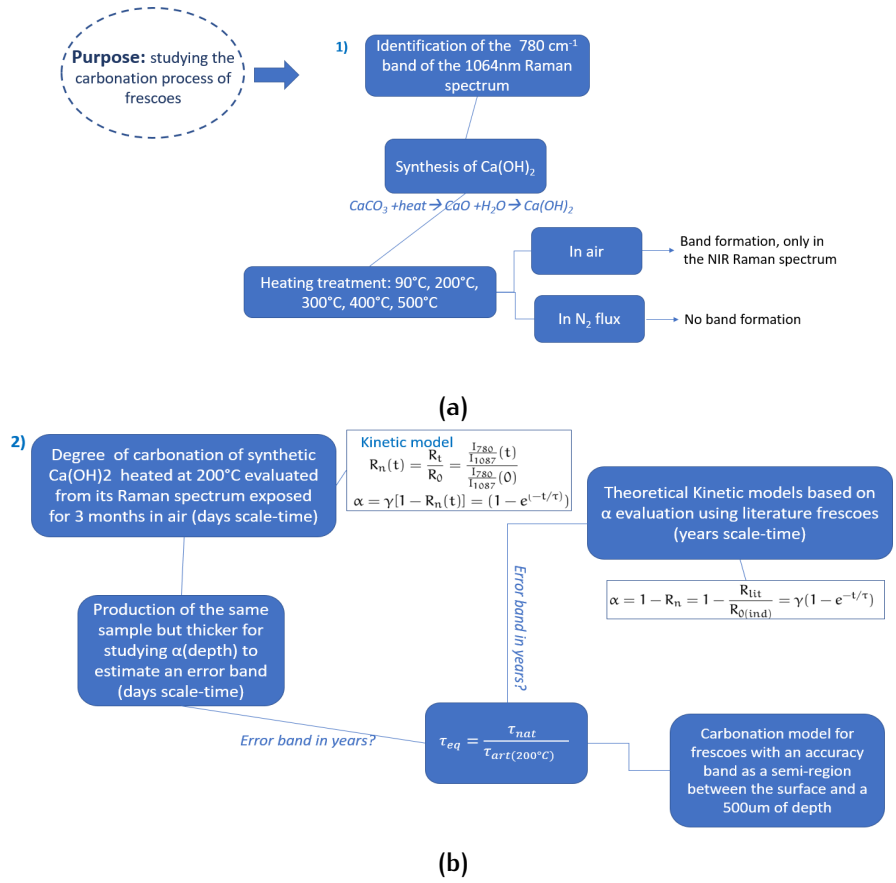

Figure 2: Schematic representation of the methodology followed for (a) the identification of the 780cm^{-1} band and (b) the creation of carbonation kinetics.

in the formation of this band. The use of different Raman excitation wavelengths is necessary to identify the nature of this band, the Raman signals are independent from the excitation wavelength. The samples synthesized were stored under standard conditions for three months, to evaluate the intensity ratio variation between the band associated with the carbonate phase (1087cm^{-1}) and the large band located at 780cm^{-1} associated with the hydrated phase at different day steps. This method permits to obtain the kinetics of the entire carbonation process.

The second step is to build a "dating" model of frescoes starting from the same experimental law obtained in the first step. A model was constructed in years by taking data from the literature, belonging to frescoes covering a period of approximately 2000 years, and applying the same kinetics to these data.The final aim was to impose an accuracy band for taking into account different sources of error in this "theoretical " model such as the variation of carbonation rate as a function of depth. Therefore, a thicker sample was made using the same methodology as above, heated at 200° C for 1 h , with a cylindrical shape and with the edges isolated to avoid unwanted penetration of

CO_2 from the sides. Five different depth levels were studied. This accuracy band, obtained in laboratory time-scale, can be then converted in years using the kinetics parameter (tau) evaluated for the literature points model.

1.1.2 Samples used for the thermal treatment

$CaCO_3$ powder were obtained by crushing pure commercial calcite stone (Sigma Aldrich, 99.95% Suprapur). The samples were calcinated at 1000 °C for two hours in order to obtain CaO powder. The product was then wetted with distilled water and mixed to complete the reaction. Finally, the obtained $Ca(OH)_2$ was heated at different temperatures (90–200–300–400–500°C) for 1 h to allow the formation of the 780 cm^{-1} band. The thermal treatment at 300°C was carried out both in air and in nitrogen atmosphere. The reported thermal treatments were carried out to achieve the same effect as the time decantation usually performed on slaked lime for several months (at least six months or more) in wide tanks in order to have a complete reaction of slaked calcium oxide with water and a complete oxygen substitution.

1.1.3 Samples Used to Evaluate the Carbonation in Depth

Marble stone powders were heated to 1000°C for 2 h. Distilled water was added to CaO compound in the stoichiometric ratio 1:1 and dried at 60°C for 1 h. Then, it was ground with mortar and pestle, the obtained powder was heated in oven at 200°C for 1 h inside a large container in order to expose a large thin layer of powder and to produce a homogeneous luminescent band in all the powder (the luminescent band obtained after a heated treatment involves only a superficial layer of 1.5 mm). Then, the treated material was compacted adding distilled water (1:1) to form a cylindrical shape with a height of 1 cm and radius of 2.5 cm. The edges were carefully isolated from CO2 absorption with an impermeable coating.

1.1.4 A list of samples used for a natural aged model, taken from Experimental Works found in Literature

The collected spectra were digitized and managed for applying the kinetic model. Two samples were experimentally studied by the authors:

- Palazzo Farnese fresco (ca. 500 years old) [23];
- Sala Vaccarini wall paintings (ca. 400 years old) [24];

- Entombment of Christ' fresco, ca. 1175 AD (ca 800 years old) [25];
- Lime walls of Southwell Minster (ca. 750 years old) [25];
- Winchester Cathedral fragment of wall painting (ca. 875 years old) [26];
- Sherborne Abbey fragment of wall painting (ca. 850 years old) [26];
- Ermita de San Pelayo fresco (ca. 900 years old) [27];
- Palace at Jerico (ca. 2100 year old) [28];
- Romano-British wall-paintings (ca. 1850 years old) [29];
- Monastery of San Baudelio (1000 years old) [30];
- San Giuseppe Church' s fresco dated around 1750–1850 (ca. 220 years ago) [31]— Experimental study.
- Branice Castel fragment (ca. 400 years old) [32];
- Amorites civilization wall painting fragment from Tell Atchana escavation—Ashmolean Museum Oxford (ca. 3500 years old) —Experimental study.

1.1.5 Experimental set-up

Raman set-up

NIR micro Raman scattering measurements were carried out in backscattering geometry with the 1064 nm line of an Nd:YAG laser. Measurements were performed in the air at room temperature with a compact spectrometer (BWTEK, Newark, NJ, USA) i-Raman Ex integrated system with a spectral resolution, as declared by the constructor, of less than 8 cm^{-1}. The spectra were collected with different acquisition times between 20 s and 80 s and power excitations between 20 and 40 mW concentrated in a spot of 0.3 mm^2 on the surface through the BAC151B Raman Video Micro-Sampling System equipped with a 20 Olympus objective to select the area on the samples.
Visible micro Raman scattering measurements were obtained in backscattering geometry through the 532 nm line by a wavelength stabilised diode module (LASOS DPSS series) coupled with a Reflecting Bragg Grating (Optigrate-Braggrade 405) to narrow the laser line. Measurements were performed in the air at room temperature with a triple spectrometer Jobin-Yvonne Dilor integrated system with a spectral resolution of about 1 cm^{-1}. Spectra were recorded in the Stokes

region by a 1200 grooves/mm grating monochromator and a charge-coupled device (CCD) detector system.

Photoluminescence (PL) and Photoluminescence Excitation (PLE) Measurements

Samples were excited with different laser sources at 405 nm, 532 nm, and 632.8 nm to collect the luminescence through a detection system composed by the spectrometer BWTEK (Newark, USA) with a spectral 1040–1460 nm IR range (corresponding to a 100–2500 cm^{-1} Raman shift). The emission signal was collected in front face mode by a wide spectral range optical fiber of 200 m diameter. In addition, we performed PLE measurements by selecting the light of a laser driven Xenon lamp (EQ- 99X) with a set of filters of 10 nm bandwidth and collecting the emission signal by means of the previous detection system. All the emission spectra were recorded in the air at room temperature, and proper longpass filters (in wavelength) were applied when needed to remove the residual scattered excitation signal.
Finally, the modifications of the spectra were monitored for a period of 90 days to check the aging effect on the calcium hydroxide samples under standard environmental conditions (average temperature 20°C, average pressure 1 atm, and 60% of average RH). This time period was estimated to be enough to evaluate the kinetic of the studied processes

DTA/TG Measurements

DTA/TG measurements were performed through the system PerkinElmer TGA7-DSC7 (PerkinElmer, Waltham, MA, USA) varying the temperature in a controlled ramp of 10°/min. The analyses were performed in N_2 and O_2 atmosphere ranging the temperature from 25°C to 600°C. Isothermal DTA/TG in N_2 and O_2 atmosphere was executed keeping the samples for 1 h at 200°C, simulating the same experimental condition of proposed synthetic samples.

X-ray Diffraction Measurements

XRD analysis was obtained by a diffractometer Rigaku Ultima IV (Rigaku, Tokyo, Japan). The XRD pattern was collected using as excitation the Cu-K (40 KV, 40 mA), varying the angle θ in the range 10°–60°C with resolution of 0.2° step/s. Obtained patterns were analyzed by EVA database in order to identify all the phases present in the starting material.

1.2 RESULTS

1.2.1 Thermal studies for the identification of 780 cm^{-1} band

The starting point is the vibrational spectrum of unheated fresh $Ca(OH)_2$ samples under different wavelength excitations (532 nm, 632.8 nm, and 1064 nm). In Figure 3, we compare a reference spectrum excited at 532 nm [33] to the spectra of our synthesised samples excited at 532 nm (fig.3a) and 1064 nm (samples not subjected to thermal treatments – fig.3b). The reference spectrum displays two narrow bands at about 252 and 357 cm^{-1} and a large composite band peaked at about 680 cm^{-1}, already assigned to the vibrations of the OH - against the cations (two translational and one rotational E_g and A_{1g} modes) [34]. As reported in the figure, the spectra of our samples

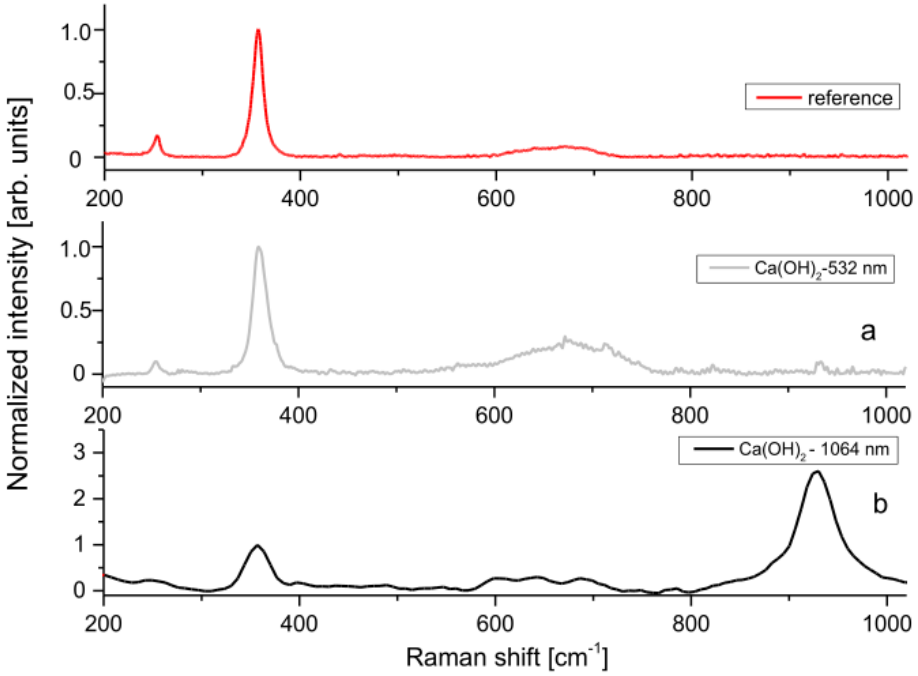

Figure 3: Raman spectrum of the lime paste: reference obtained with 532 nm excitation and the experimental sample, without thermal treatment, and with excitation at (a) 532 nm and (b) 1064 nm.

excited both in the visible and NIR range report the same vibration bands (the same result also holds for the 632.8 nm, not reported here for the sake of brevity). The spectrum excited at 1064 nm evidences a large band peaked at about 936 cm^{-1}, previously ascribed to the O–H out-of-plane bending mode of unbound water [35, 36]. The reported spectra do not show any contribution in the 700-800 cm^{-1} range irrespective of the laser excitation exploited, in contrast to the literature spectra of aged calcium hydroxide gathered under 1064 nm excitation.

To support these results, we analysed the PLE measurements by monitoring the IR emission range, with no evidence, also in these experiments, of any contribution around 1170 nm (corresponding to the 780 cm^{-1} Raman band under 1064 nm laser excitation). These observations support the idea that the Raman band in the 700–800 cm^{-1} range reported in some literature spectra [16] does not belong to vibrational features nor to luminescence characteristics of fresh pure calcium hydroxide.

To further analyse the origin of these optical findings, we considered the carbonation/calcination cycle reported in the introduction. As already observed, the Raman spectrum excited with 1064 nm excitation (Figure 3b) shows a large contribution of the band at 936 cm^{-1}, associated with the O–H out-of-plane bending mode of unbound water, suggesting a large content of water in our samples not reported in the literature spectra of aged lime. Indeed, the reported spectra were collected on the raw samples, not subjected to any heat treatment. To reduce the water content and speed up the drying process of the synthetised $Ca(OH)_2$, we heated the samples at different temperatures in the 90–500°C range. We measured the Raman spectra of the heated samples by exciting, once again, the vibration modes with visible and NIR laser sources (532, 632.8, and 1064 nm). Whilst no contributions were detected in the 700–800 cm^{-1} range with visible excitations, a large temperature-dependent band peaked at about 780 cm^{-1} is recorded when exciting at 1064 nm (Figure 4). This finding strongly supports the hypothesis that the recorded spectral feature is related to the carbonation/calcination cycle and could be ascribed to some luminescence centre promoted during the thermal treatment.

Figure 4 shows the Raman spectrum of the Ca(OH)2 -heated samples at different temperatures (all the thermal treatments were carried out for 1 h). Besides the three vibrational modes previously reported (at 252, 357, and 680 cm^{-1}), the spectra are characterised by a large and composite contribution at 780 cm^{-1} and two new smaller peaks at 283 and 1087 cm^{-1}. In order to evidence the dependence of the 780 cm^{-1} band on the temperature, the spectra were normalised to the calcium hydroxide contribution at 357 cm^{-1} (for this reason the Ca(OH)2 bands appear as faint contributions in the figure). The intensity of the 780 cm^{-1} band increases as the temperature increases up to 300°C; then, it largely decreases, as reported in the inset of the figure. At the final investigated temperature (500°C), the relative contribution of the two new bands at 283 and 1087 cm^{-1} increases, showing the formation of calcite (external E_g and internal A_{1g} modes, respectively) [37, 38].

The observation of the two calcite bands suggests that the carbonation process is ignited by the thermal treatment. In order to understand the possible connection between the formation of the 780 cm^{-1}

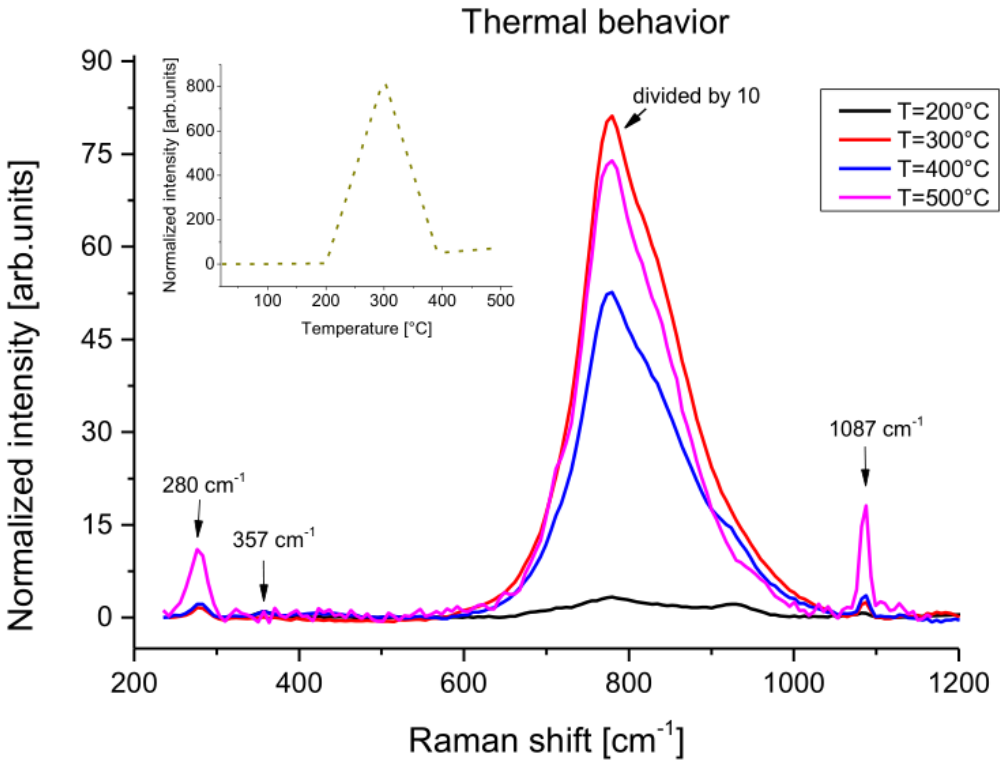

Figure 4: Raman spectra with 1064 source of lime paste heated at different temperatures for 1 hour in the air (the curve at 300°C was arbitrarily divided by 10 for clarity purposes). The insert shows the normalised intensity of the bands at 1170 nm for the different temperatures.

luminescence band and the carbonation process, we carried out the thermal treatment at 300°C (corresponding to the maximum recorded for the 780 cm^{-1} intensity) under different environments, namely in air and under nitrogen flux. The latter was exploited to eliminate the presence of other possible reactive gasses, such as CO_2 and O_2 present in air. The Raman spectra of lime paste heated in air and in nitrogen at 300°C and excited at 523 and 1064 nm are reported in Figure 5. The intensities are arbitrarily normalised to the peak of calcium hydroxide at 357 cm^{-1} .

Confirming the previous results, the 780 cm^{-1} band can only be detected under 1064 nm excitation, whilst no contribution is recorded under visible excitation. The spectra clearly indicate that the 780 cm^{-1} luminescence band is largely decreased when the thermal treatment is performed in nitrogen flux. We estimated the relative contribution of the 780 cm^{-1} band with respect to the calcium hydroxide 357 cm^{-1} band, the ratio increasing from 0.83 in nitrogen-treated samples up to 27 in the sample treated in the air.

As for the presence of calcite, we estimated its contribution by measuring the ratio of the 1087 cm^{-1} band with respect to the 357 cm^{-1}

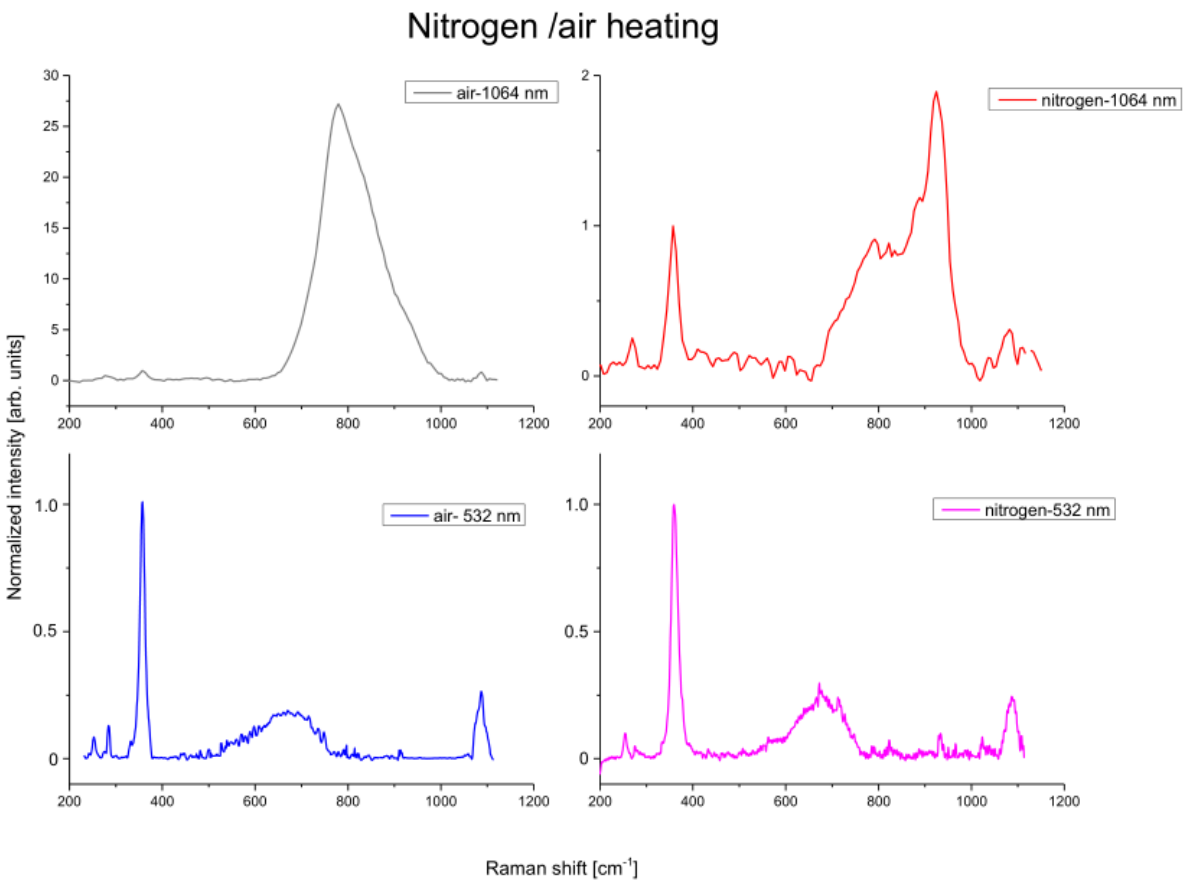

Figure 5: Raman spectra of paste lime heated in air and in N2 atmosphere for 1 h at 300°C with 532 and 1064 nm.

band. The calcite relative content is larger in the sample treated in the air (the ratio is 0.87) than in the sample treated in nitrogen (0.23). To validate the aging process by thermal treatment, we measured the XRD patterns and the high-resolution Raman spectra of the heated samples. As reported in Figure 6a and 6b, no other phases of the compounds are detected, revealing that the heating procedure does not modify our samples. This is confirmed by vibrational spectra, where we observed that the heat treatment slightly affects the position and shape of Raman peaks, due to a possible small structural variation (inset of Figure 6c).

DTA/TG analyses were performed through the system Perkin-Elmer TGA7-DSC7 varying the temperature in a controlled ramp of 10°/min. We performed the analysis in N_2 and O_2 atmospheres and we observed the same curve. Figure 6d and 6e reports the experimental data obtained in N_2 atmosphere. Our measurements confirm that below 370°C no mass loss of $Ca(OH)_2$ is detected and beyond this temperature takes place the conversion to CaO (a maximum of 440°C is recorded), confirming all the results obtained in literature. In particular, considering the temperature values used in this work (range

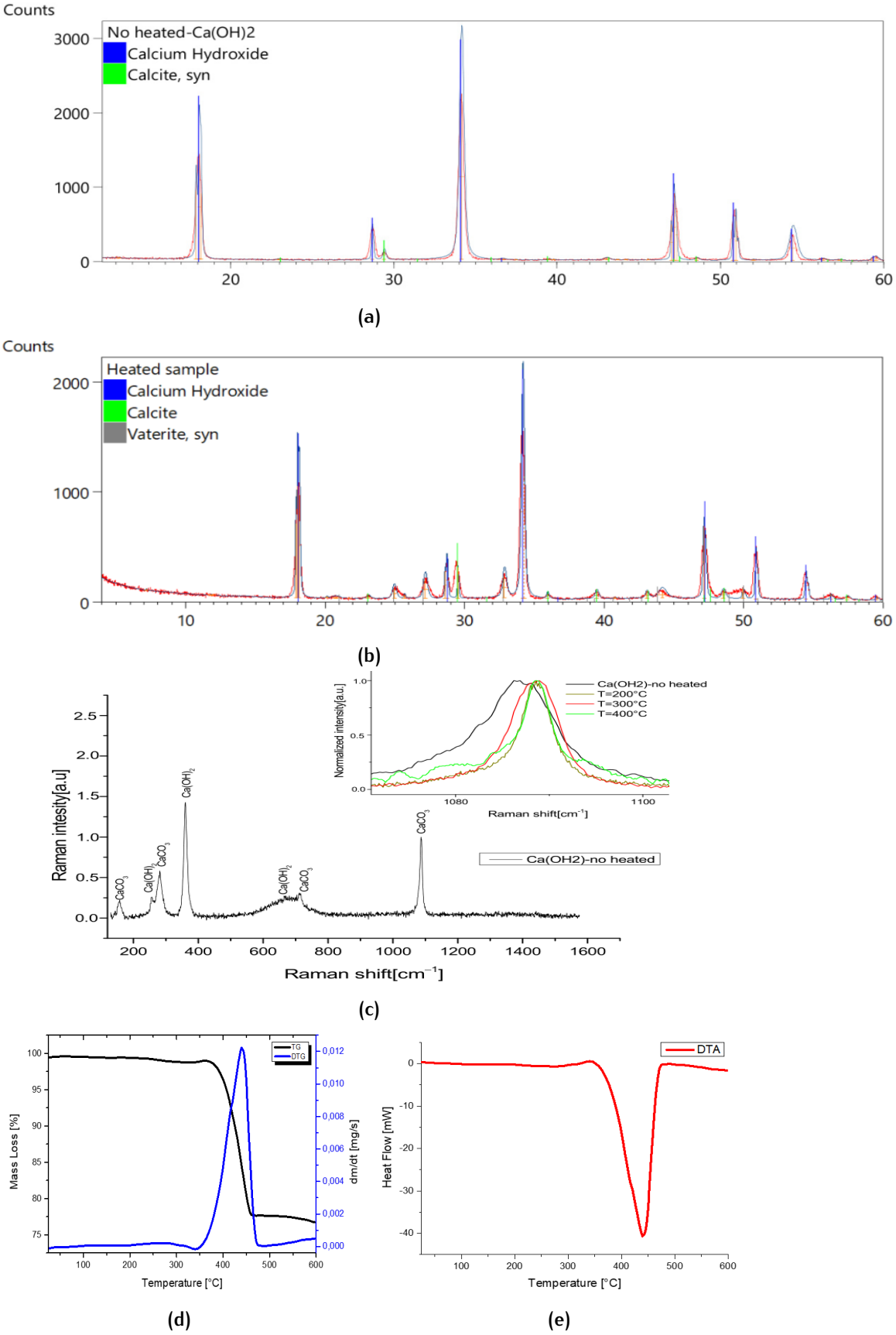

Figure 6: (a) XRD pattern of calcium hydroxide after synthesis; (b) XRD pattern of calcium hydroxide after 200°C-heated exposed to air for 20 days; (c) 785 nm high resolution Raman spectra of synthesized Calcium hydroxide exposed to air for 20 days; inset, the comparison between the no-heated and heated calcium hydroxide 785-Raman spectra, details of the 1087cm^1 band; (d) and (e)DTA/TG and DTG analysis of $Ca(OH)_2$ samples performed at N_2 and O_2 atmosphere.

90 – 500°C), we calculated the percentage of CaO in our samples, these results are reported in table 1. No carbonate phase is expected

Temperature	90	200	300	400	500
CaO (%)	0	0	0	20	100

Table 1: Percentage of CaO in the $Ca(OH)_2$ heated samples from DTA/TG analyses.

at these temperature in DTA/TG measurements as found in literature. Actually, as suggested by Koga et al. (Phys.Chem.Chem.Phys. 2018, 20, 26173), by adding a percentage of 15% of CO_2, the carbonation reaction take place beyond 600°C. Isothermal DTA/TG at 200°C executed for 1h (same experimental condition of proposed synthetic samples) does not reveal any mass variation both in O_2 and N_2 atmosphere.

Based on these results, two considerations can be deduced: first, the carbonation process is faster in oxidizing atmosphere; second, we found a confirmation that the band is indeed a luminescence one, and, in addition, we propose to assign it to some defect of the crystal structure possibly interacting with the O_2 molecule or promoted by the interaction/reaction with it. To further characterize the kinetics

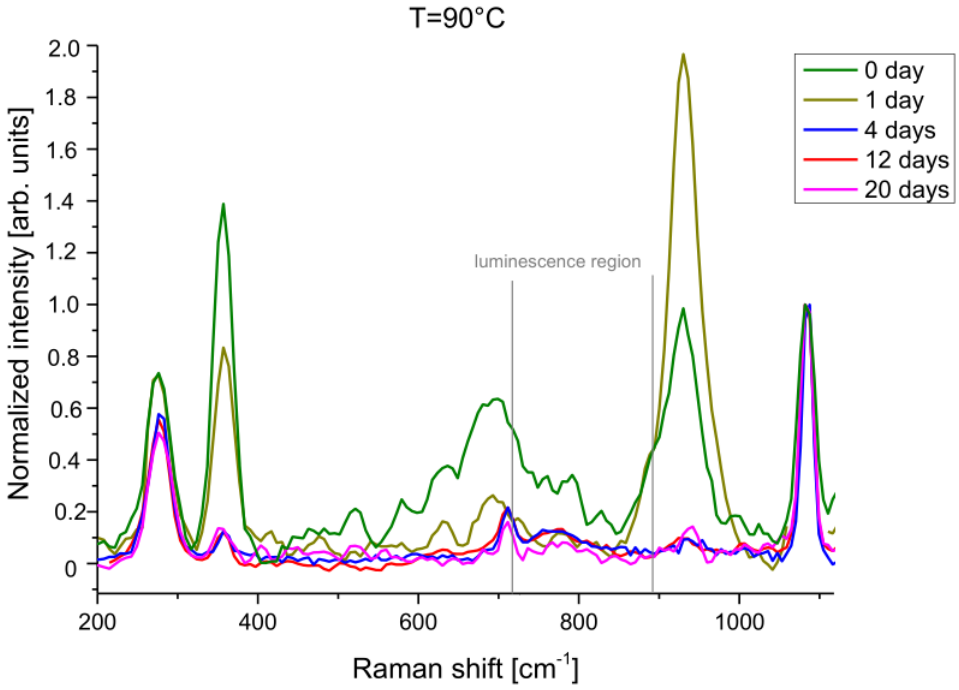

Figure 7: Dependence of the luminescence bands with the time of heated samples at T = 90°C.

of the formation of the 780 cm^{-1} luminescence band, we investigated its temporal evolution by monitoring the Raman spectrum excited at 1064 nm for several days. The analysis was carried out on the samples treated at different temperatures by leaving them in the air at room

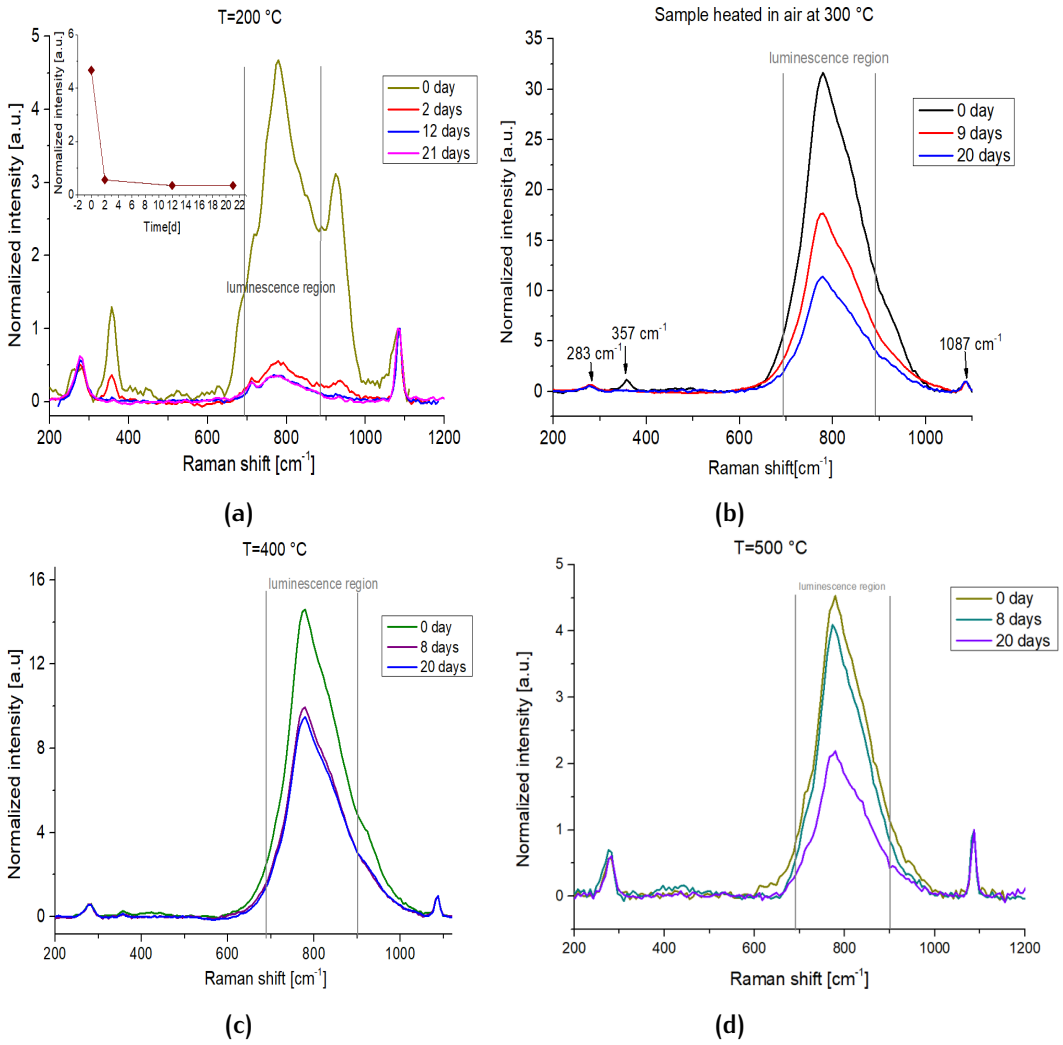

Figure 8: Dependence of the luminescence bands with the time of samples heated in air at : (a) T = 200°C ;(b) 300°C; (c) 400°C and (d) 500°C.

temperature and under standard RH conditions (60%).
Figure 7 shows the spectra for the samples heated to 90°C and arbitrarily normalised to the 1087 cm^{-1} calcite peak. In the luminescence region, no emission bands are detected, whilst the peak of calcium hydroxide (357 cm^{-1}) decreases during the time, suggesting that the carbonation of lime paste takes place.
Indeed, in the time zero spectrum we observe both the contribution of the peak around 936 cm^{-1} attributed to the O–H out-of-plane band [35, 36, 39] and the one of calcium hydroxide at 357 cm^{-1}, the former being higher than the latter; then, after four days both features strongly decreased, indicating that the free water and the calcium hydroxide reacted to form calcite.

The Raman spectra of the sample heated to 200–500°C are reported in Figure 8. In general, the luminescence band at 780 cm^{-1} is observed for all the temperatures at the time zero spectrum and it undergoes a large decrease as a function of time (see inset). The contribution

of free water is clearly singled out only in the time zero spectrum of the sample treated at 200°C spectra, whilst in the other cases no free water contribution is detected, suggesting that, as expected, at a higher temperature the whole nested water is eliminated by the thermal treatment. The whole set of samples displays the formation of calcite in the first days of observation.

Finally, we performed the same analysis on the samples treated under nitrogen flux (Figure 9). Besides the smaller contribution of the 780 cm^{-1} luminescence band already noted in the time zero spectrum, we also observed that the band undergoes a larger relative decrease than in air, its relative intensity being reduced by a factor of 6 in nine days for the nitrogen-treated sample, as compared to a reduction of a factor of 2 in the same observation time for the air-treated sample.

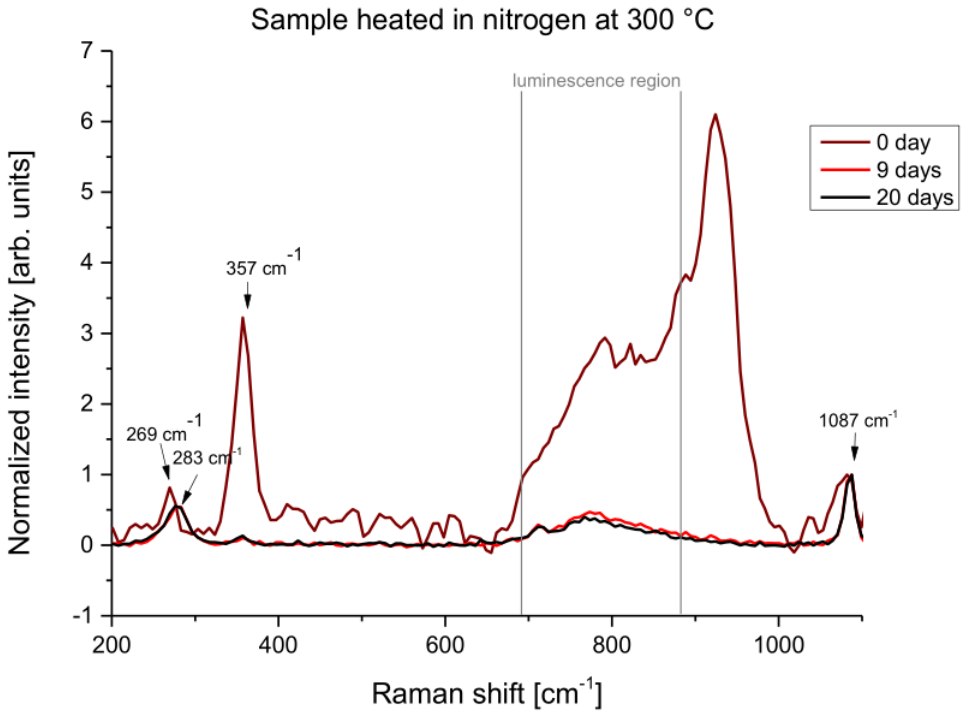

Figure 9: Dependence of the luminescence bands with the time of nitrogen-heated samples at T = 300°C.

1.2.2 Kinetic model of Calcium Hydroxide carbonation

According to these findings, we can hypothesise a kinetic model of the carbonation process that can be monitored from the relative intensities of the Raman band at 1087 cm^{-1} (calcite) and the luminescence band at 780 cm^{-1} that we tentatively assigned to some calcium hydroxide crystal defect interacting with molecular oxygen [40, 41].
The formation of calcite is somehow related to the decrease of the 780 cm^{-1} luminescence band, suggesting that the defect responsible for

that luminescence is involved in the carbonation process. One can hypothesise that the defect centre is largely reactive to environment CO_2, thus acting as a seed for the carbonation process. To monitor the kinetic of the reaction, we consider the relative contribution of defects centres (counted by the intensity of the 780 cm^{-1} luminescence band) and the already formed calcite crystals (counted by the 1087 cm^{-1} Raman band). We express the starting ratio as $R_0 = \frac{I_{780}}{I_{1087}}$. When the time increases, the carbonation process occurs, and the luminescence band decreases. To evaluate the fraction of emitting centres undergoing carbonation at time t with respect to the starting population, we calculate the normalised ratio R_n defined as follows:

$$R_n(t) = \frac{R_t}{R_0} = \frac{\frac{I_{780}}{I_{1087}}(t)}{\frac{I_{780}}{I_{1087}}(0)} \tag{2}$$

where the term R_0 represents the relative starting concentration of emitting defective centers with respect to the amount of calcite crystals after the thermal treatment, and R_t indicates the relative concentration of the defects at the instant t during the progressive carbonation process. By assuming a first order kinetic, in agreement with the model proposed by Camerini et al. in [42], a rate equation can be found, as follows:

$$\alpha = \gamma[1 - R_n(t)] = (1 - e^{(-t/\tau)}) \tag{3}$$

where α is the carbonation degree, τ represents the characteristic time of the process, and γ is the maximum carbonation relative value (asymptotic value in the graph).

Figure 10 reports the calculated model from experimental data recorded over 90 days for the whole set of samples, that is the ones treated at different temperatures and under different environments.

The first order kinetic model successfully fits the acquired data but for the 500°C treated sample, where a second-order kinetics is observed, suggesting that a second carbonation process is occurring beside the previously described one. It is important to underline that the first-order kinetic model accounts for the fraction of centres that can be transformed into calcite, the final amount being dependent on the thermal treatment undergone by the sample. The curves show that the process is slower for the samples treated at 90°C (τ = 10 days), and is the fastest at 200°C, where the luminescence band had its maximum of intensity at zero time (τ = 0.7 days); then, it decreases its speed down to τ = 25 days for the 400°C samples. Finally, at 500°C the kinetics changes, as explained before. We can also note that the nitrogen-treated samples (at 300°C) had a trend comparable with the 200°C samples (in air) with a slightly smaller final relative value of the carbonated centres.

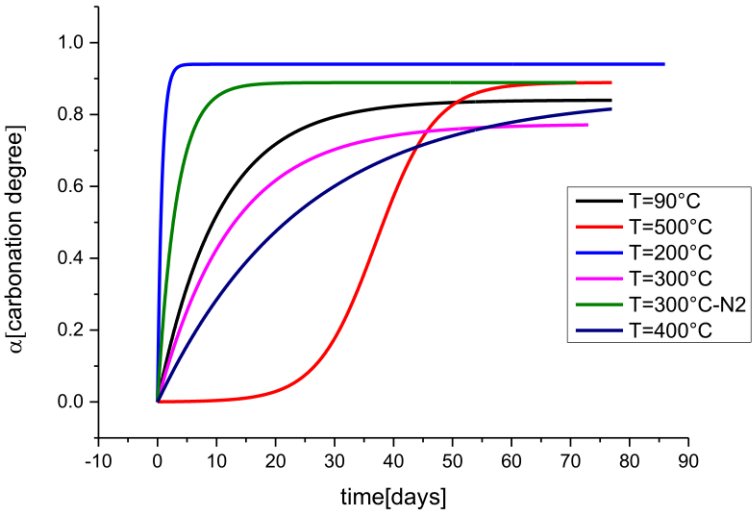

Figure 10: Kinetic model of our experimental data using Equation (3)

1.2.3 From the kinetic model to a frescoes dating model

In order to propose an aging model for lime wall paints exploiting the above-mentioned first order kinetics to evaluate literature and experimental data, some crucial aspects and possible sources of error need to be preliminarily investigated. Among the others, the choice of a common R_0, the evaluation of the sampling depth, and the history of each sample are the most important. Each of these factors can heavily influence the estimated age of an artwork through the final alpha-value. In the following, we propose how each aspect can be dealt with.

The first step is to apply Equation (3) to naturally aged frescoes, so that we collected spectra of frescoes and wall paints from literature, spanning a time interval of various centuries. As already done for synthetic calcium hydroxide powders, we calculated the R_t-value of an artwork as the intensity ratio between luminescent band at $780cm^{-1}$ (1160–1170 nm) and the calcite band at $1087cm^{-1}$. To estimate the R_t-value of each artwork, we considered its declared age. The correct evaluation of the carbonation degree α (see Equation (3)) stems from the choice of a common R_0-value for all the artworks. In principle, the R_0-value would be proportional to the storage/settling time of the lime used and then it could depend on the manufacturing procedure of each historic civilization. The points used for developing the model belong to different historical periods with different syntheses procedures, so they could have different R_0. In order to demonstrate the importance of assuming a R_0 common value, simulations of the carbonation degree as a function of R_0 are reported in Figure 11. The increase in R_0 leads to a decrease in the characteristic time of the curve (tau). Then, at high R_0 values, the carbonation degree reaches its maximum faster, showing that fits with R_0 value greater than 7 are useful

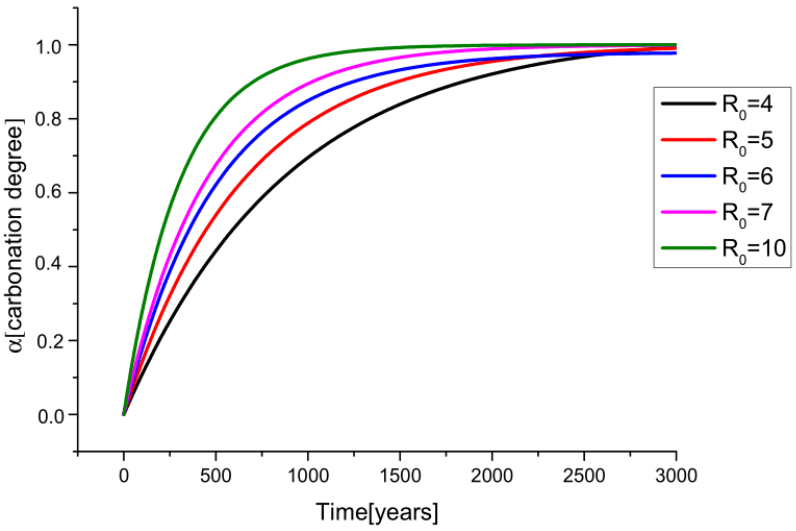

Figure 11: First order kinetic model calculated at different R_0.

to analyze a shorter time range (500 years), whilst lower values of R_0 allow the analysis of a larger time range.
We can remedy this problem by determining an average theoretical R_0 from literature data by plotting R_t-values as a function of the time (Figure 12). According to Equation (3), and assuming the term $\gamma = 1$ (i.e., all the possible superficial centres are completely carbonated at the end of the process), we get the following Equation (4):

$$R_t = R_0 e^{t/\tau} \tag{4}$$

where τ is the characteristic time of the process. The operated fit returns an average R_0 value of (3.4 ± 0.3). This value is in very good agreement with the experimental $R_{0(ind)}$ of modern industrial calcium hydroxide $(3.3 \pm 0.3$, vide infra), realized with synthesis processes very similar to ones of ancient civilization. Indeed, contemporary production of calcium hydroxide in the construction industry follows the consolidated settling/storage process explained, for example, by Vitruvius in [43, 44], being the common procedures to obtain calcium hydroxide by the natural process based on the storage/settling of the material for a period ranging within nine months and two years. The complete formation mechanism of this defective phase, in a natural process, is not completely understood. Actually, a storage/settling in an aqueous medium produces the formation of amorphous $Ca(OH)_2$ [45], and in an air medium, carbonation. Then, the production of this defective band is still an object of study.
Thus, the value $R_{0(ind)} = 3.3$ could be considered a reasonable choice because it is in agreement with the average R_0-value obtained from the previous analysis. The industrial calcium hydroxide $R_{0(ind)}$ was obtained as the average ratio of the spectrum bands collected in dif-

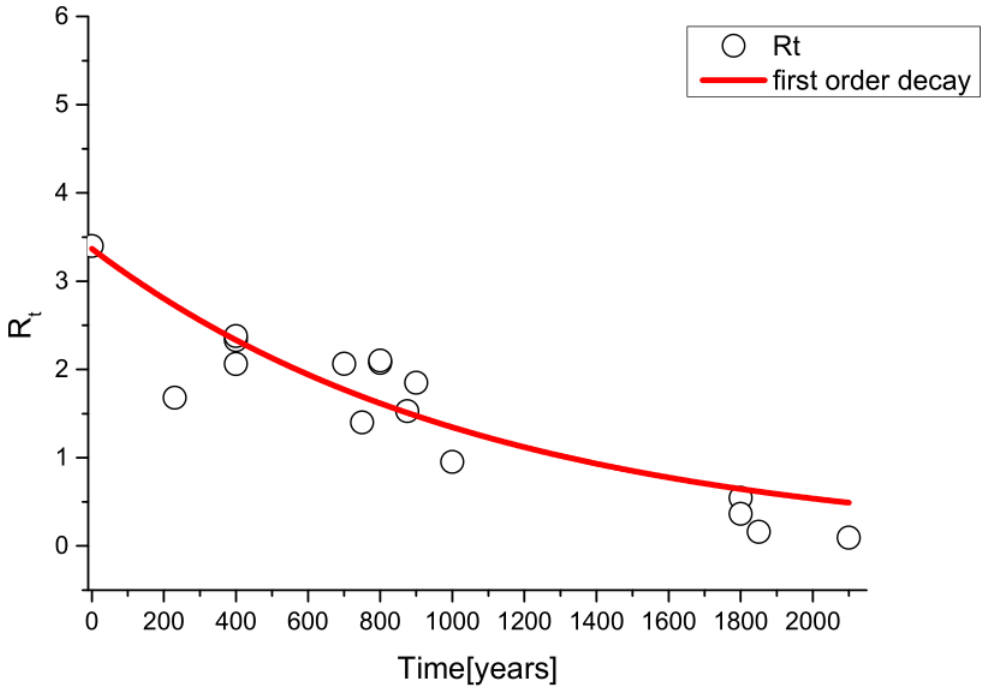

Figure 12: First order decay fit to obtain an average R_0 value from literature points

ferent points of the powder (see Figure 13a) and can be used in the Equation (5) (naturally aged model) to extract the characteristic time of the the carbonation process from the literature data:

$$\alpha = 1 - R_n = 1 - \frac{R_{lit}}{R_{0(ind)}} = \gamma(1 - e^{-t/\tau}) \tag{5}$$

The fit obtained from these values is shown in Figure 13b and provides a characteristic time $\tau = (1490 \pm 400)$years (the asymptotic γ value was set to 1, assuming that, according to the age of each reported artwork, the carbonation process was completed). Although the calculated tau seems to be very large for fresco paintings, it should be remind that it represents the characteristic time associated with the carbonation of the only defective phase of carbon hydroxide present in the sample and not to the overall amount. In addition, according to the literature [3, 46, 47], the natural carbonation reaction in a fresco could be very slow, because of the decreasing of surface porosity, shielding effect associated with external carbonated layers and the presence of carbonated core-shell systems of calcium hydroxide grains.

The reported fit assures that the model is able to date frescoes and wall paintings belonging to different historical ages.

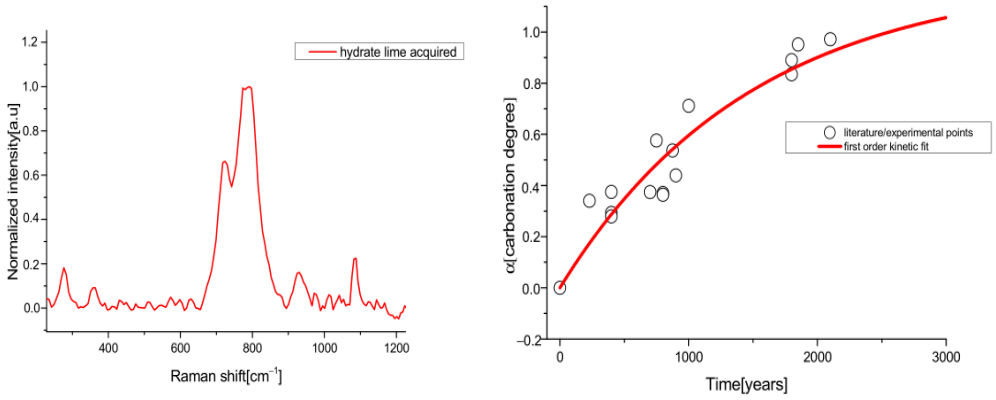

Figure 13: (a) 1064 nm-Raman spectrum of calcium hydroxide acquired; traces of calcite are present; (b) first order kinetics applied on data taken from literature and experimental data.

1.2.4 Carbonation process as function of depth

To improve the validity of this model, we need to also consider how the carbonation process, due to the diffusion of CO_2 inside the fresco wall proceeds in depth. As reported in the literature, the carbonation process occurs in the whole wall due to diffusion of CO_2 inside the wall frame, and this phenomenon should be taken into account to develop a more sophisticated kinetic model. In fact, carbonation starts with the diffusion of dissolved CO_2 molecules in pore water of wall paste [48], and then the formation of calcium carbonate from calcium hydroxide is observed. The result of this reaction is to alter the chemical composition of the concrete, which reduces pH and can lead to conditions which may cause the corrosion of reinforcing steel within the concrete [49]; in particular, the carbonation process of the calcium hydroxide in concrete can reduce the pH of concrete to values less than 9 [50].

The carbonation of lime inside a wall is related to the diffusion process of the carbon dioxide. The carbonation process starts at the surface (which is in direct contact with air) and penetrates slowly into the wall interior, resulting in a function of depth. The carbonation slows down in depth; then, the reduction of pH (due to the increasing of carbonate phase) is itself a function of depth, conditioning the strength and durability of the painting.

The diffusion of CO_2 in walls depends on many factors, such as CO_2 concentration, porosity, and moisture inside the plaster and mortar, that affect gas transport properties within the wall structure. At the end of carbonation reaction, water is produced, and it further affects the diffusion of CO_2 and humidity [51] inside the wall layers. Thus, due to the intrinsic interdependence of each parameter in the diffusion process, any analytical model for the prediction of carbonation

is intrinsically complex and should be based on a nonlinear scheme [48]. Several experimental studies on concrete carbonation under outdoor and indoor conditions were carried out and they agreed with the hypotheses that depth of carbonation is directly proportional to the square root of the ageing time of the wall [52–54]. Different mathematical formulations were developed to model CO2 diffusion in concrete and the effect on the carbonation process, the most accredited one being the following Equation (6) [55, 56]:

$$X_c = \sqrt{\frac{2D_{CO_2}[CO_2]t}{[Ca(OH)_2]}} \tag{6}$$

where X_c is the carbonation depth [m] at time t [s], D_{CO_2} is the effective diffusion coefficient of carbon dioxide [m^2/s], [CO_2] is the molar concentration of carbon dioxide in the atmosphere in contact with the wall layers [mol/m^3], and [$Ca(OH)_2$] is the molar concentration of calcium hydroxide in the wall [mol/m^3].
The expression of the effective CO2 diffusion coefficient is $D_{CO_2} = \Phi(1 - S_1)\theta D_{air,CO_2}$; it depends on the diffusion coefficient of carbon dioxide in the air (D_{air,CO_2}), the wall porosity Φ, the water saturation degree S_1, and a parameter used to model the material tortuosity (θ). CO2 concentration is one of the most important parameters of carbonation in a deep layer: under low CO2 concentration (2–20%), the increase of carbonation depth was found to be higher than in the case of high concentration exposure. The reason is mainly due to the microstructure change caused by concrete carbonation, which makes the surface layer denser, thus lowering the rate of CO2 diffusion into wall layers [57].

Thus, a study on the depth-dependence of the carbonation process is necessary because sampling at different depths can lead to large differences on the estimated carbonation degree of an artwork. As already reported [28, 29], analyzed points of a fresco could be taken on the surface or on substrate layers, when, for example, examining the spectra from a wall paints; in addition, optical objectives with a high depth of field collects signals from many layers below the surface. These facts can affect the fits proposed in Figures 11 and 13b, possibly providing an explanation for the discrepancy of some points with the model curve.

To perform this study, we needed to recreate a sample which presented not only similar characteristics of natural lime but also an aging speed compatible with a laboratory scale time. As previously explained, the artificial aging was performed by thermal treatment in the 90–400°C range, to reproduce the 780 cm^{-1} band, to achieve the same starting degree of defective calcium hydroxide and to study their kinetics within an affordable laboratory time scale. We were able

to reproduce the carbonation process in surface obtaining R_0 values as a function of the temperature (within a variable range of 0.3 and 32). Now, we need to map the thermal treatments to natural aging

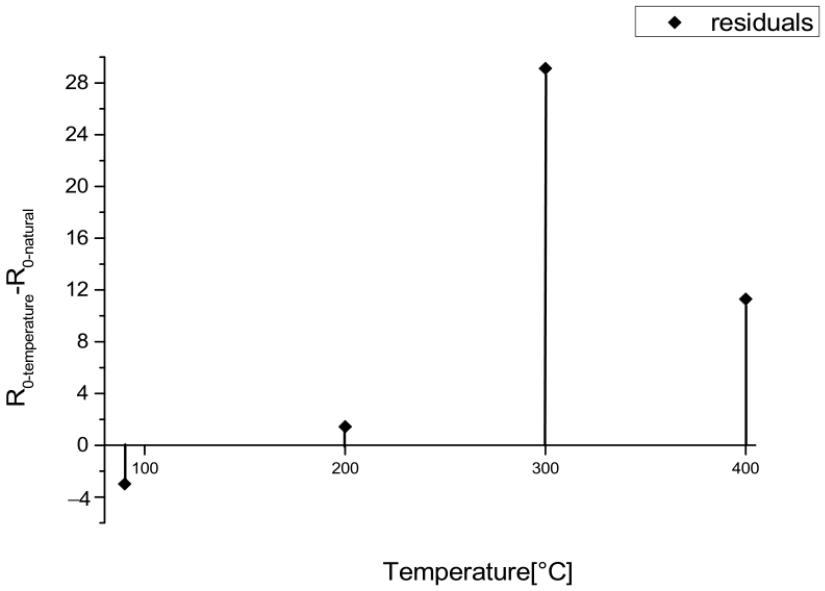

Figure 14: Difference between R_0-values obtained from artificial aged models heated at different temperatures (R_0-temperature) and the R_0-value of natural aged model (R_0-natural).

applying the model to the evaluation of the carbonation process in depth. To this purpose, among the samples realized at different temperatures, we selected the one heated at 200°C, whose measured R_0 value of (4.7 ± 0.6) is the most similar one to the $R_{0(ind)}$ (fig. 14). In addition, to carry out the evaluation of the carbonation process along the depth, we need to calibrate our previous kinetics models to the heat treatments. Therefore, we estimated a conversion factor from the ratio between the natural and artificial characteristic times as indicated in Equations (7) and (8):

$$\tau_{eq} = \frac{\tau_{natural}}{\tau_{artificial}} \tag{7}$$

The same procedure can also be applied to map all the artificially aged samples (at 90–300–400°C), as follows:

$$\begin{aligned} \tau_{calibrated\ 400°C} &= \tau_{400°C} \cdot \tau_{eq} \\ \tau_{calibrated\ 300°C} &= \tau_{300°C} \cdot \tau_{eq} \\ \tau_{calibrated\ 100°C} &= \tau_{100°C} \cdot \tau_{eq} \end{aligned} \tag{8}$$

The γ parameter related to the relative amount of carbonation obtained in the previous section did not reach the asymptotic value of 1. Assuming that the luminescent band is related only to a hydrated phase instead of a carbonated one, it is reasonable that, after a long time, the entire amount of starting portlandite will naturally convert

into calcite and that band may disappear. Therefore, we set $\gamma = 1$ in the calibration equation. Finally, we can write the calibration Equation (9):

$$\alpha = 1 - e^{-t/\tau_{calibrated}} \tag{9}$$

leading to the curves reported in Figure 15.

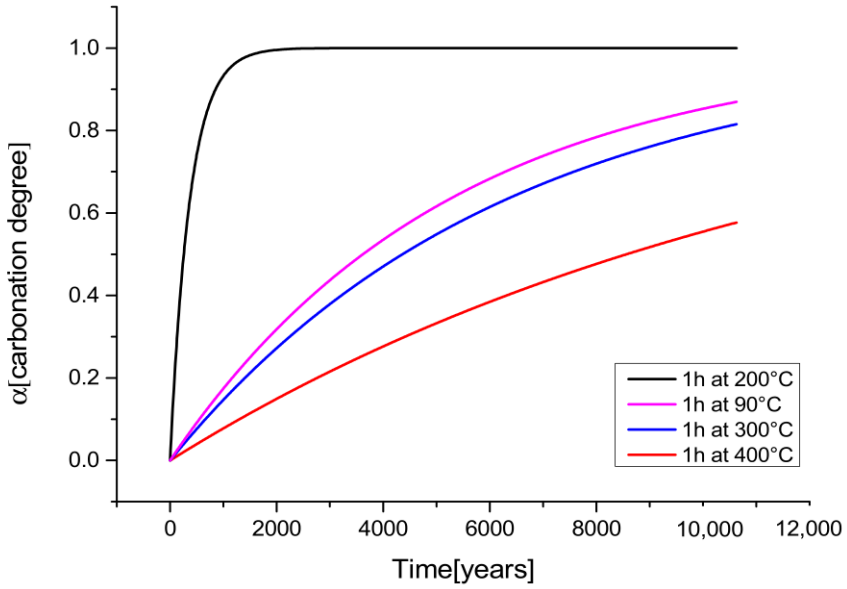

Figure 15: Calibrated fits using τ_{eq} to obtain aging kinetic models pretreated for 1 h at different temperatures.

To analyze the carbonation process as a function of the sample depth, the measurements performed in progressive depths were taken over 18 days, with step of 2–3 days, down to a depth of 4 mm from the surface. This procedure aims to correlate the progressive diffusion of CO_2 inside the sample, producing different kinetics of carbonation, to the effect of ageing connected to the same carbonation as proposed before.

As evidenced in Figure 16, the first order kinetic model accurately describes the carbonation process also in depth, but for the 4 mm case (Figure 16a) where a linear trend is recorded. We can explain this effect considering that the carbonation slows down as it proceeds in depth because of many concurrent factors such as the increasing of RH%, a low content of CO_2 available, etc. Thus, after 20 days, we are able to appreciate only the linear range of the model (first part). The other reported curves (between 0 mm and 3 mm) do show the same trend and are successfully described by the model (the characteristic time of each curve is reported in Table 2). Our results can be further exploited to evaluate the diffusion of carbon dioxide (D_{CO2}) and verify Equation (6) (Figure 16b).

If we assume that the ratio of $Ca(OH)_2$ and CO_2concentration is expressed by Raman derived Rn values, since the CO_2 diffusion pro-

First Kinetic Fit	τ[Days]	Maximum Carbonation Relative Value
0 mm	0.74(9)	0.89(1)
0.5 mm	1.6(2)	0.84(1)
1 mm	2.3(2)	0.77(1)
2 mm	3.1(6)	0.74(2)
3 mm	6(1)	0.69(5)
4 mm	-	-

Table 2: Fit parameters of the carbonation curve in depth.

duces only the carbonation process, we can retrieve the relationship between CO_2 diffusion and depth from the experimental data. As reported in the figure, the data are well fitted by a square law relationship, confirming the hypothesis of Equation (6).

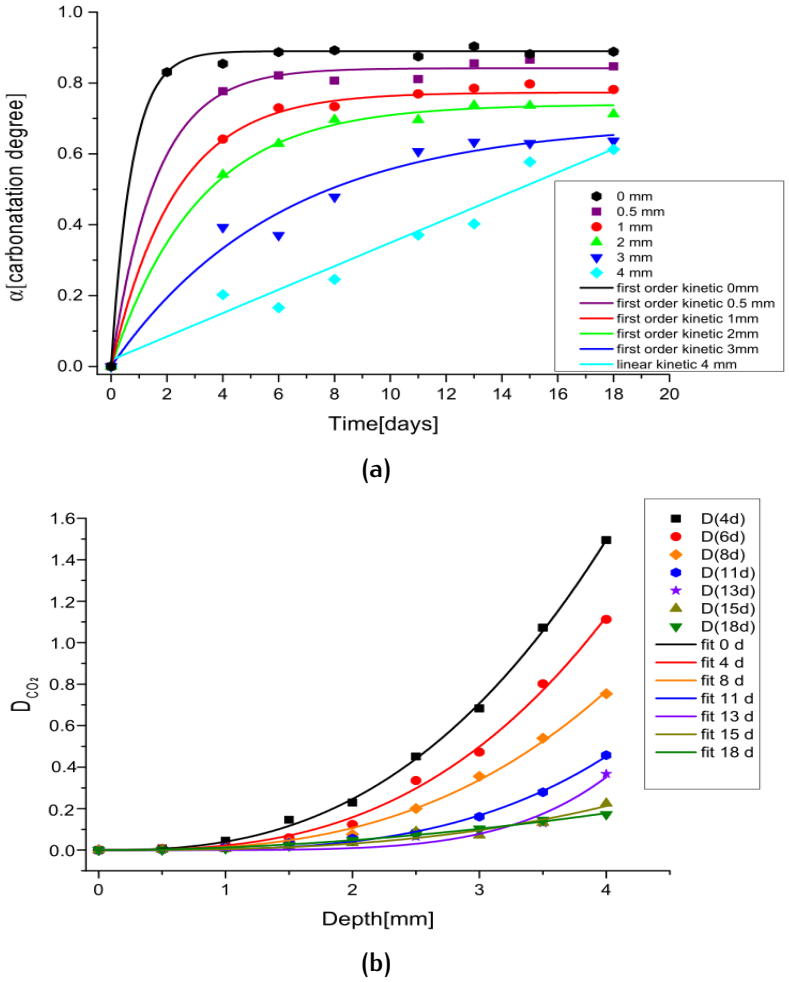

Figure 16: (a)Kinetic model in depth for a sample heated at 200°C, (b) diffusion coefficient for unit of [CO_2] in a sample heated at 200°C as a function of carbonation depth at different days of air exposure.

The diffusion parameter increases remarkably with depth during the first week of analysis, then it changes slowly. Moreover, CO_2 diffusion is proportional to sample porosity, to the water degree (related to RH) and the sample tortuosity [55, 56]. From this point of view, a

possible explanation of the increasing trend with depth could reside in the porosity variation. In fact, with the carbonation process, the porosity of the medium decreases causing a gradient as a function of the depth [58]. In addition, the enhancement of RH causes an increase in the volume fraction of the pores occupied by water, thus leading to a reduction of the diffusion parameter [59–61]. With the intention to validate the model, the exposed results need to be validated with an accurate study where the composition at single depth is determined.

1.2.5 Factors Conditioning the Model and Accuracy

Many factors are involved in the carbonation rate, and, as reported in the previous figure, it is clear that carbonation measurements are strongly related to the sampling depth in a fresco. Actually, the observed kinetics associated with the sample depth can affect our dating model, especially considering the sampling procedure.
We can define a "depth-parameter" related to the experimental sampling procedures, to account for surface erosion, corrosion, crack formation or substrate measurements with different objectives or in different layers of fresco.
To consider this source of uncertainty in our model, we considered a depth parameter of about 0.5 mm and thus the values reported in Table 2 for the 0.5 mm depth. This assumption is justified by considering that the characteristic time of 0.5 mm is twice the one of 0 mm and that condition is sufficient to cause a considerable uncertainty. The results are shown in Figure 17a where previous data are once again considered with the addition of two new sets of experimental data to further discuss the model.
Those samples, shown in Figure 17b and 17c, are characterized by peculiar conservation conditions, so that they can represent a stress test for our model. It is clear, indeed, that the two new sets do not follow the dating model, or, reversing the sentence, the reported data display that the known age of the samples and the estimated one largely differ because of the conservation conditions. One of the new samples belongs to a fresco of the San Giuseppe Church (realized around the end of the 18^{th} century). The estimated carbonation degree is 250 years older than its real age (230 years old). The second sample belongs to a Sumerian wall painting dated around the second to first millennium B.C. It shows a carbonation degree comparable with an age of 700 years old in our model. As already stated, these data fall out of the model curve because of the conservation conditions.

In the first case, the location of the fresco can explain the discrepancy. It was painted in the vault of the Sacristy, typically illumined with candles so that the carbon dioxide and smoke produced from the candles, as testified by the superficial blackening of the paint and

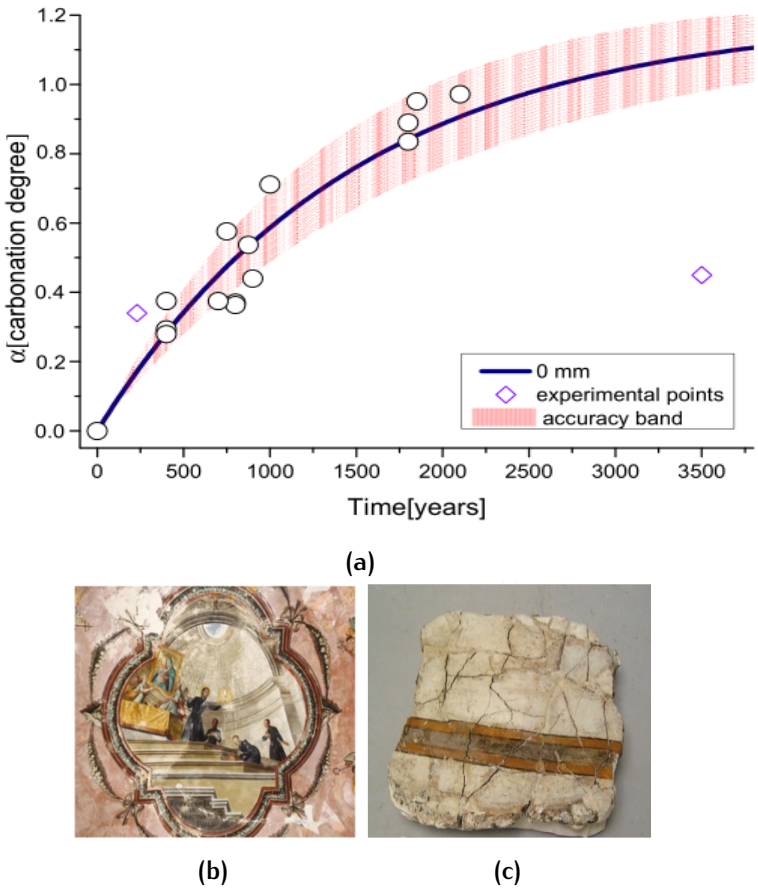

Figure 17: (a)Final kinetic model(0 mm-surface) with accuracy band(red), literature points (circles), experimental points (rhombuses); (b) San Giuseppe fresco (ca. 230 years old); (c) Amorite civilization wall painting fragment from Tell Atchana excavation (ca. 3500 years old)

by Raman analysis [31], could have sped up the carbonation process of the fresco. In the second case, the fragment remained buried until a few decades ago, thus largely slowing down its carbonation process. These two examples illustrate that the dating procedure is a delicate one because many external factors could affect the carbonation process here accounting for dating purposes. Among the others, one should always consider water infiltration, indoor and outdoor exposure, restoration interventions or burial conditions, which could affect, as demonstrated here, the evaluation of the sample aging. To conclude, applying the dating procedure from this preliminary model, the age of a sample can be evaluated starting from the Equation (10) (obtained from Equation (3)):

$$t = \tau \ln(1 - \alpha) \tag{10}$$

which presents, at the moment, an accuracy of 40% (see figure 18) in relation to all the factors mentioned before. Important improvements

can be obtained by (1) reducing the τ_{error} related to the literature points used in the text; and (2) increasing the experimental sampling procedure (focus) to determine the R_t parameter and then the carbonation grade alpha. Despite the accuracy being not so good, it is not so far from other methods like radiocarbon. If we consider the no-destructivity of this technique, we retain in any case a good result.

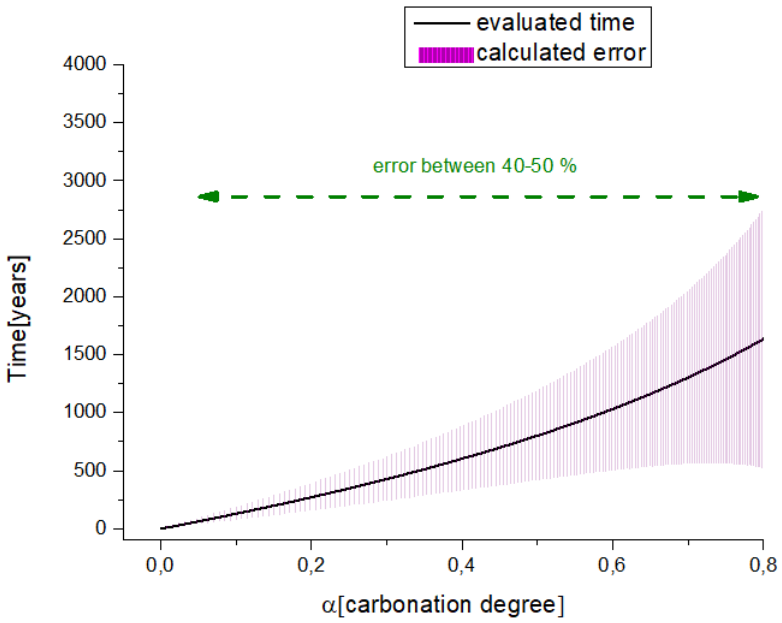

Figure 18: Time error in the dating procedure evaluated with a tau-error of 400 years (fitting procedure) and alpha-error equal to the semi-dispersion of in deep-procedure (figure 17a).

1.3 SYNOPSIS OF THE OBTAINED RESULTS

In this first chapter, by using the information obtained with NIR-Raman spectroscopy appplied to calcium hydroxide, the carbonation process of ancient wall paintings taken from literature and from experimental samples was exploited to achieve a preliminary dating model for frescoes. The model is based on the variation in relative intensity ratio of two bands: the $780cm^{-1}$ band (excitation at 1064 nm) ascribed to luminescence defects in calcium hydroxide and the $1087cm^{-1}$ band ascribed to vibrations of the carbonated phase.
To definitively give this attribution of the $780cm^{-1}$ band (1160 nm) visible in the NIR Ramana spectrum of mural paintings, in ancient mortars and in plasters, firstly we carried out a detailed optical analysis (photoluminescence excitation measurements in the 200–500 nm spectral range and Raman measurements with laser sources at 405 nm,

532 nm, 632.8, and 1064 nm) of synthetic lime paste. The intensity of this band is related to the temperature used for the heating process, (in a range between $100 - 500^{\circ}C$), showing a maximum at $300^{\circ}C$ and also we noticed a dependence of the heating environment. In fact changing from a reducing to an oxidizing one, we evidenced that the interaction with molecular oxygen, and possibly carbon dioxide, is required to produce the defective centre responsable of this particular emission. The centre acts as a preferential site for the carbonation process of the powders observed during the aging of the samples over 90 days, as indicated by the monomolecular model successfully applied to heated samples, and subsequently to the literature wall paintings samples.

In order to explain one of the possible discrepancy factors of the kinetic model developed, a study of the carbonation process as a function of the depth in a synthesized calcium hydroxide sample was executed. The aim of this study was to improve and set a validity region of our starting model. We determined an accuracy band as the semi-region between the surface and $500\mu m$ of depth curves, comparable with the variable sampling depth with 1064 nm-Raman source on a painted surface.

2 DEGRADATION STUDIES ON DIFFERENT STANDARD PIGMENTS

Pigments degradation is a dynamic phenomenon that affects numerous materials in the field of Cultural Heritage. In fact, all the pigments, organic and inorganic, synthetic and mineral, degraded over time. Degradation can arise from environmental conditions, light exposure, bacterial attacks, or the use of erroneous solvents during the restoration process. It is well known, the most famous pigments used in painting are usually semiconductors. Depending on the surrounding environment, these materials are potentially not stable and degradation processes can take place through reactions with the atmosphere, especially with molecules, such as carbon dioxide, sulfur, oxygen, water, etc. [62, 63]. The result implies the formation of patinas of new compounds due to carbonation or oxidation processes. Sometimes, the environmental conditions cause a phase transformation in the mineral that can present a different color. The reaction depends on many important parameters, such as temperature, light, relative humidity, pristine defect density in the materials, points of nucleation, time, etc. Several studies analyzed in detail the degradation phenomena, ranging from structural properties to vibrational fingerprints or colorimetric parameters [64–70]. The color change translates into the variation of optical characteristics, like absorption, transmittance and reflectance which correlate the electronic properties or band structures with the macro effect on visible rendering. Degradation products can be detected by the means of several well-known conventional analytical and optical techniques such as Raman spectroscopy, Reflectance, luminescence, XRD and SEM.

For the two degradation case studies presented in this work, we decided to concentrate our attention also on nucleation processes due to an initial presence of defects in the structure. Those point defects could be related to different phenomena, such as, for example, light exposure. Once the degradation process is observed, one can trace back the numerous steps that led to the deteriorated materials, down to the presence of nucleation areas where the process started. Sometimes, these nucleation areas can be readily observed on the surface of the applied pigment. We want to promote a non destructive diagnostic tool to detect those puntual defects (so associated to the earliest stages of degradation) and try to prevent further degradation, thanks to the combined use of some optical technique (listed above), such as

Raman spectroscopy, reflectance, and exploring the potential of pump and probe for this purpose [71–76].

In fact, the transient absorption (TA) spectroscopy can be used as a preventive tool in discovering defects responsible for the color changes in the pigments. It is a proficient tool to understand the pigment degradation, because it is able to investigate the changes of the optical properties of a material [77–79]. In this technique, the probe transmittance through the sample is measured both in presence and absence of the pump, as a function of relative time delay between the two pulses. Due to both linear and non-linear interactions, changes in the absorption spectrum of the materials are observed, providing information about the optical interaction, the electronic band structure, excitation and relaxation mechanisms, defects.
There are three main features that can be distinguished in a TA experiment: Ground State Depletion (GSD) or Ground State Bleaching (GSB), Excited State Absorption (ESA) and Stimulated Emission (SE) [80]. In GSD the pump pulse excites the carriers from the ground state to the excited state, thus causing the decrease of the ground state population and the increase of the excited state population. This change of the relative population of the two states lead to a decrease, or bleaching, of the optical absorption, with negative differential absorption spectrum. ESA occurs when the pump photons excite the carriers from the ground state to some excited intermediate state. Subsequent probe photons may excite the carries from this intermediate level to a still higher energy level, thus producing additional new features in the absorption spectrum, with positive differential absorption signatures. Lastly, SE occurs when probe photons stimulate the radiative decay of carriers, previously excited by the probe, leading to the increase of the probe intensity transmitted through the sample, with negative differential absorption. A deepened analysis of ESA, GSD and SE signals is very useful in studying the position of electronic bands or the presence intermediate levels originating the optical transitions, especially when degradation is appearing.

In the next section, the darkening of the red vermilion, it will be proposed a detailed example of how this optical technique in combination with other techniques such as reflectivity can be fruitfully used for the preventive diagnostic for standard pigments.

2.1 CASE STUDIO: THE DARKENING OF RED VERMILION

The darkening of red vermilion is the subject of numerous studies engaging the entire community of Cultural Heritage scientists [81–

85]. This phenomenon was recently investigated to understand the causes which determine the degradation and the role of other environmental agents in this process [86–89]. Recent works shed light on the possible phase transformation from alpha-cinnabar (red) to beta-cinnabar (black) during the darkening [90, 91]. The process is accentuated in presence of halide impurities ions (chlorine) and the formation of metallic Hg was observed. At high concentration the appearance of chlorine-based compounds was not excluded as found in other works [92–96].
In a previous work [97], we obtained evidence of phase change (alpha to beta) and metallic mercury formation following a photo-degradation process. Starting from this assumption the aim of this study is oriented to deepen its degradation process using accelerated degradation process through UV exposure and catalyzing the full process with a chlorine solution, and analyzing the change induced with the TA spectroscopy. The TA results will be also supported and corroborated by a DFT (Density Functional Theory) simulation.

2.1.1 Red vermilion: structure, band gap and degradation theories

Structure

Several works report the crystal structure of the HgS system [98–100]. As reported by Ballirano et al. [86], the crystal structure of cinnabar can be identified in three different phases: red α-HgS having trigonal structure ($P3_121$ space group) with lattice constants a=4.1489 Å and c=9.4947 Å; black cubic β-HgS (F43m space group) with lattice constant a=5.8461 Å; γ-HgS (hypercinnabar) with hexagonal structure and lattice constants a=7.0103Å and c=14.1307Å.
Due to the impurities in the composition, the α-HgS phase converts to cubic metacinnabar β-HgS, in the temperature range between 373K (HgS 99.97 %wt) and 635 K (HgS 99.999 %wt) [98, 99]. This transformation presents a value of enthalpy ranging from 2 to 8 kJ/mol. In addition, it was found a very low kinetic of the reverse transformation from β-HgS to α-HgS phase at room temperature [86]. At 798 K the metacinnabar transforms to hypercinnabar.

Degradation processess

Many references suggest different mechanisms ascribable to the darkening of cinnabar. One hypothesis is associated with the phase transformation from red hexagonal α-cinnabar into black cubic β-cinnabar (called also metacinnabar), formulated by Feller [87] and further studied in many other references. This implies that reflectance properties of red cinnabar are altered by light exposure because of the production of dark phase metacinnabar [84, 91].

Another hypothesis reports the formation of transition chloride compounds (mercury chlorides or sulfochlorides) which present a darker coloration with the consequent effect of total blackening of vermilion. These chlorine-based compound like calomel Hg_2Cl_2, terlinguaite Hg2ClO, eglestonite $Hg_6Cl_3O(OH)$, corderoite $Hg_3S_2Cl_2$ and kenhsuite Hg3S2Cl2, are often instable and they dissociate re-forming, in particular cases of relative humidity (RH) and pH, amorphous mercury sulfide.
There is then the photochemical redox to obtain metallic Hg^o and S^o, after catalysis by halogens at high RH under sunlight/UV exposure. So the dark coloration is due to the presence of grey metallic Hg clusters into the red pigment [83, 101].

And lastly a thermodynamic effect: the dissociation of α-HgS in metallic Hg^o and β-HgS, due to a transition temperature in the range 373–673 K, as discussed before. The transition temperature can decrease drastically in presence of Cl ions, in the system Hg–S–Cl–H_2O with prevalence of Hg ions. As reported by Radepont et al. [82], at 300 K the effect of pH leads to a simultaneous presence of Hg^o and $\alpha - HgS$ with mutual concentration depending on pH. In this condition the presence of β-HgS is not excluded. However, a predominant concentration of Cl ions, depending on the pH, implies the formation of Cl-based compounds like calomel or corderoite.

Band structure of alpha-HgS, beta-HgS and some Cl-based compounds

Alpha-HgS presents electronic characteristics as a semiconductor with predominant direct transition. Doni et al. [102], studied the band structure of alpha-cinnabar phase reporting in the Brillouin zone a first conduction band at 2.2 eV from the top of the valence band. The energy thickness of the first conduction band is estimated at around 1.5 eV. From the top of the first conduction band, the authors showed a second conduction band located at 1.2 eV.
Figure 19(a) shows a schematic representation of the band structure concerning the phase alpha. In relation to the previous phase, the beta phase exhibits a very short bang gap around 0.25-0.54 eV which characterizes its behaviour similar to metallic Hg. The electronic properties of beta-HgS were studied by Cardona et al. [103] in the Brillouin zone. Instead of the alpha-phase, beta-HgS presents a unique conduction band. We reported in figure 19b a schematic representation of the band structure.
For completing the possible scenario of the phase transformation, especially in presence of chlorine impurities, we report also the schematic band structure of calomel (Hg_2Cl_2), corderoite (α-$Hg_3S_2Cl_2$) and mercuric chloride ($HgCl_2$) considered in literature the most likely phases that could be formed during the degradation process (figure 19c). Following a recent work of Hogan et al. [83], we report the

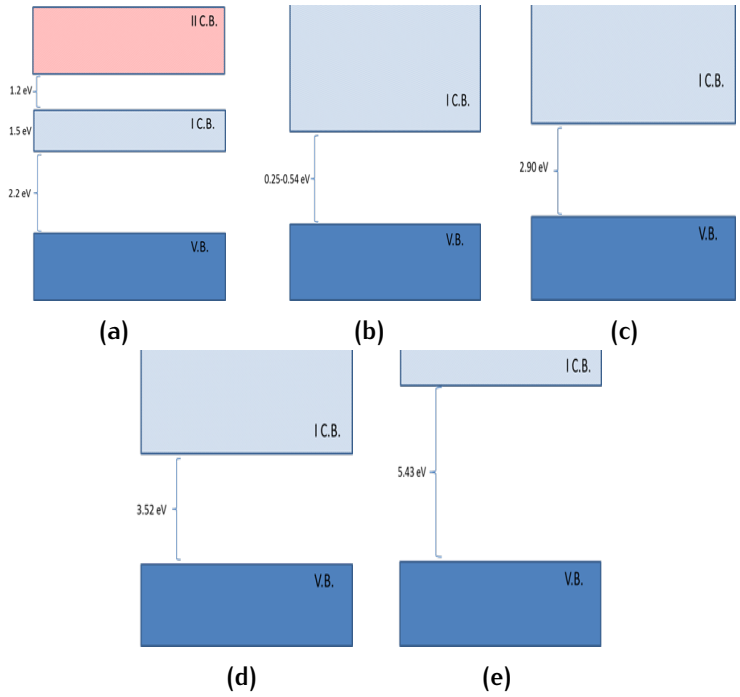

Figure 19: Sketch of band structure of HgS phases and some compounds correlated to cinnabar darkening: alpha-HgS (a); beta-HgS (b); alpha-Hg3S2Cl2 (c); HgCl2 (d), Hg2Cl2 (e).

schematic structure band and the energy gap of these chlorine-based compounds. In particular, for corderoite, calomel and mercuric chloride the energy gap was estimated as 2.90 eV, 3.52 eV and 5.43 eV respectively.

2.1.2 Materials and Methods

Analytical methodology

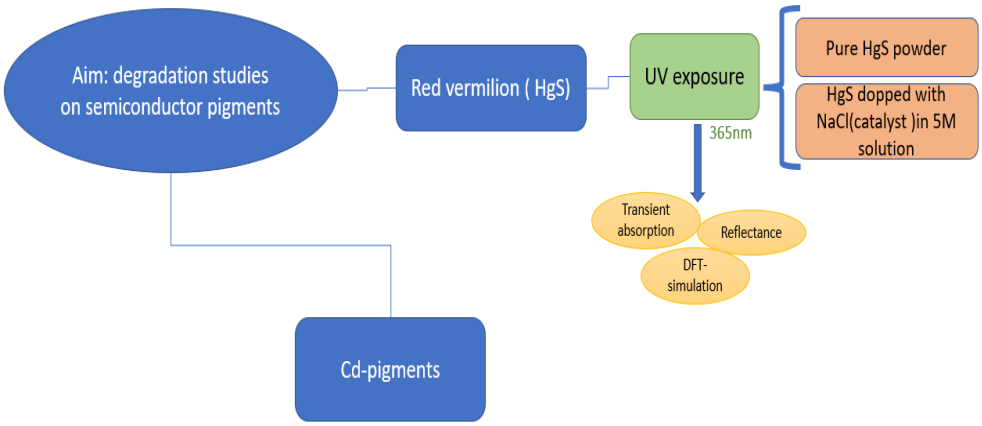

Figure 20: Schematic representation of the methodology followed for the studies of Red vermilion degradation.

Accelerated optical degradation processes, i.e. using UV light, were carried out to study the degradation process of red vermilion. In order to establish the role of chlorine, and to accelerate the degradation process, both pure and chlorine-doped samples were subjected to optical exposure. Induced colour changes were investigated with reflectivity, and possible electronic differences by means of ultraviolet spectroscopy and DFT-simulation.

Samples for the Accelerated degradation process

Pure red cinnabar in powder form, provided by "Opificio Pietre Dure" (Florence – Italy), having 65 μm grain and volume density of $8.1 g/cm^3$ (Natural Cinnabar Monte Amiata 100% - CAS-Nr: 1344-48-5 – Red/ Medium - Kremer Pigmente K10610- Pigment Red 106, C.I. 77766), were dispersed in distilled water and mixed with 5 molar concentration of NaCl. The mixture was hold under agitation for 1 h at room temperature. Solutions were then applied to a specific support to obtain a pigment deposit available for our analysis. All solutions were dropped to glass slides and dried, with the final results of a solid deposit of about $100 \mu m$ thickness and covering area of about $2 cm^2$. We report the assigned nomenclature of samples connected directly to the molar concentration: 0.00M NaCl called "pure" and 5M NaCl called "5M". All synthetic samples were treated under the UV light of a LED at 365 nm (emission with Lorentzian profile having full width half maximum of 10 nm), under constant power density of $10 mW/cm^2$, for time ranges between 0 and 200h. So the set of samples is composed by pure HgS not exposed (HgS-pure), the pure HgS UV exposed for 148 h , HgS 5M not exposed and HgS 5M UV exposed for 20 h. To complete the study, we analyzed also for comparison a metallic Hg sample contained between two glass slides.

Experimental Set-up

TRANSIENT ABSORPTION SET-UP

Transient absorption measurements were performed with a pump-probe differential spectrometer (Ultrafast Systems HELIOS-EOS), with both pump and probe wavelengths generated by a Ti:Sapphire regenerative amplifier (Coherent Libra-F-1K-HE-230), which delivers 100 fs long pulses at 800 nm with 1 KHz repetition rate. The main emission from the regenerative amplifier was splitted into two branches: one sent to an optical parametric amplifier (Light Conversion TOPAS C), in order to generate the pump wavelengths (400 nm and 360 nm), and the other sent to the sapphire plate of the HELIOS spectrometer, where multicolor probe beam was generated by means of white light supercontinuum generation. The probe pulses were time-delayed with respect to the pump pulses, by passing through a

variable digitally controlled optical delay line. The pump and probe beams were then non-collinearly focused and overlapped on the sample surface, with the pump being chopped at 500 Hz, so that half of the transmission spectra were recorded with the pump on, and half with pump off. The Transmission spectra of the probe beam were recorded as a function of the relative delay time, by means of CCD spectrometers. Only for the case of metallic Hg the TA signal was recorded in reflectance mode using a pump of 360 nm.

REFLECTANCE MEASUREMENTS

Reflectance measurements were performed by means of UV–Vis-NIR Agilent Technologies Cary 5000 spectrophotometer equipped with integrating sphere module. The reflection configuration at 10° measures the diffuse reflection of the sample with respect to a reference sample which is considered to have a 100% reflectivity. A calibrated source Illuminant D65 was used to determine the reflectance spectra and for calculating the colorimetric parameters. Pure and 5 M solutions were dropped and dried upon an inert polyvinyl chloride (PVC) support until a compacted homogenous powder deposit was obtained (disk with r = 16 mm, thickness = 1 mm).

2.1.3 Results

In figure 21a, reflectance spectra of the analyzed samples are reported in the range 400-800 nm.
These spectra can be correlated directly with the linear absorption by operating a Kubelka-Munk transformation of reported curves. It is worth noting that the first derivatives of reflectance spectra (fig. 21b) show two weak broad bands at around 650 and 730 nm in exposed samples, suggesting additional absorption properties due to the degradation process.
No other additional bands are evidenced especially in the region before 600 nm which represents the fundamental transition. These information are useful in the interpretation of transient absorption spectra. Figure 22 reports the Transient absorption spectrograms of unexposed and exposed pure HgS sample. The pump-probe data were obtained varying the pump power in a range between 0.002-0.600 mW and collecting the signal in the "short live" range (10 ps – delay step 0.02 ps) and "long live" range (10 ns – delay step 0.1 ns). We verified that the selected wavelength (400nm) and excitation power did not permanently modify the optical features of the investigated samples in terms of color variation. On the contrary, we also exploited the 360 nm excitation in the case of pure HgS to show the effects of pump irradiation. At this wavelength we obtained an evident and permanent darkening of the surface.

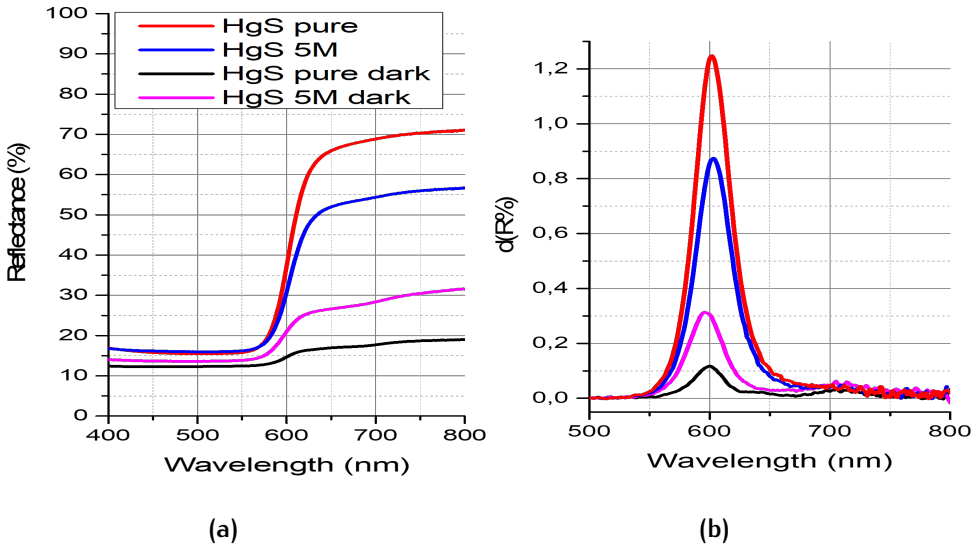

Figure 21: Reflectance (a) and first derivative Reflectance (b) spectra.

The false color scale of the spectrograms shows a differential absorption signal measured in optical density (OD) ranging from positive (red color) to negative (blue color) values. TA spectra and decay profiles can be extracted from the maps by integrating the signal upon specific time and wavelength range, respectively. Those spectra and profiles are reported on top and on the right of each spectrogram. Reported data are perfectly reproducible for each point of analysis and are completely representative of these samples.

In figure 22a, unexposed pure sample (HgS pure) shows two short negative signal at 670 nm (broad) and at 480 nm, the first ends after 6 ps and the second converts after 1 ps to a positive signal of about 10 ps. Positive signals were revealed over a pump power threshold of 200 μW. A different trend can be evidenced (fig. 22b) for the exposed pure sample (HgS UV) after 148h of UV irradiation, where a short negative signal centered at 630 nm, converts within 3 ps into a composite positive signal with two bands at 530 nm and 650 nm.

These positive signals have a "long-lived" time (see figure 22c). In addition, this sample shows other two long signals in the ns scale, not observed in the pure sample: a negative contribution between 650 nm (broad band) and 800 nm (narrow band) and a positive one picked at 480 nm. Both signals have a decay time of around 5 ns. The positive signal at 480 nm (2.58 eV) is compatible with an Excited State Absorption (ESA) which promotes an electron to an excited state located in the first conduction band (I C.B.), after pump absorption, to the second conduction band (II C.B.) of the material when the probe is absorbed (graphical rapresentation are shown in figure 25).

The negative features observed in both the samples are Ground State Depletion (GSD) signals towards shallow trap levels due to intrinsic defect formation in the first prohibited region. These levels are at

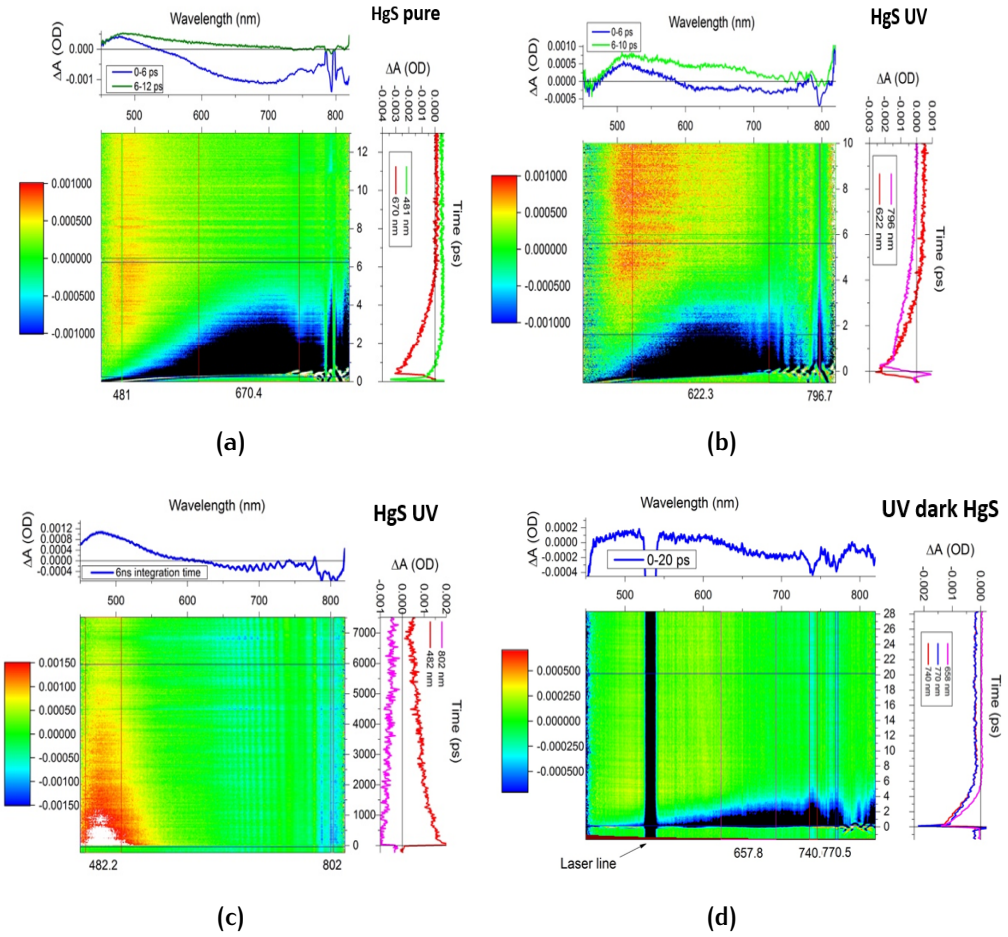

Figure 22: Transient absorption maps, wavelength and time profiles of HgS pure samples: unexposed sample (a); UV exposed (b); exposed observed in long-time range (c); UV induced dark in unexposed sample through 40 mW of 360 nm line (d).

around 1.82 eV (670-680 nm) in HgS pure and Hg UV samples. In the latter sample, we found also a "long-lived" GSD signal at 800 nm (1.54 eV) associated to the formation of other defects after exposure to the UV light. These defects cause the presence of deep traps from the bottom of I C.B., which corresponds to a consistent darkening effect in the visible region. The formation of new defects associated with irradiation is further confirmed by the use of the pump at 360 nm and power of 40 mW in the pure HgS sample (figure 22d), where additional UV-induced negative signals at 740 and 770 nm are evident. Moreover, the application of UV light to the samples changes drastically the characteristic decay time of the revealed signals that moved in the ns range. In particular, a long ESA is revealed at 480 nm and a long bleaching at around 800 nm. The latter assumes a very similar trend as compared to metallic Hg which presents a "long-lived" negative signal in the range of ns between 450 and 800 nm (see figure 23). The reported results suggest the formation of a cinnabar phase upon

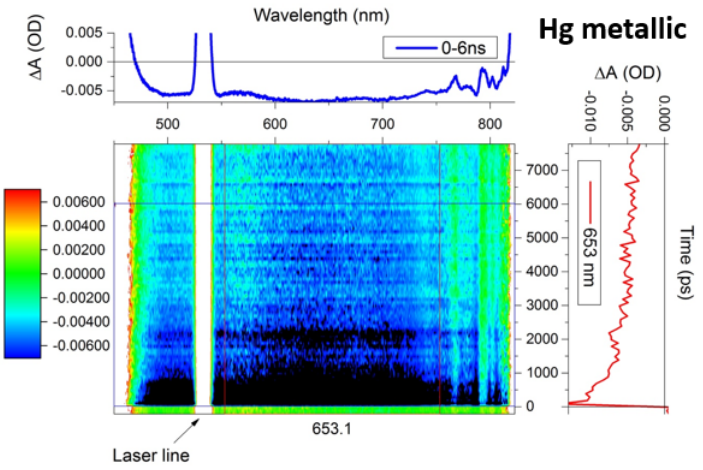

Figure 23: Transient absorption map, wavelength and time profiles of metallic Hg.

UV irradiation with spectral features similar to metallic Hg. Concerning the attribution of this phase and in particular the detection of the beta-cinnabar phase, it is worth noting that in the investigated spectral region it would be impossible to distinguish between beta-cinnabar phase and metallic Hg. Indeed, according to the band structure sketched in figure 19, the band gap of the black beta phase is around 0.25-0.54 eV which corresponds to the 2200nm-5000nm IR region. This range is out of our experimental setup and, by using the presented pump-probe configuration, it is impossible for us to distinguish between metallic Hg and beta phase. However, as illustrated before, the presence of defectivities producing a band gap reduction, and consequently a darkening effect, lead us to suppose a progressive formation of a strongly defective alpha phase. We expect that when the number of defects is structurally unsustainable for this configuration, the alpha phase transforms to beta one, as proved in [90].

Regarding the samples doped with Cl-ions, we found a sort of variability of the signal depending on the sampled point. This reproducibility calls for a non-uniform effect of Cl doping on the samples, as the grained morphology of the samples (see ref. [97]) could also suggest. Despite these variations, the results can be reconducted to few trends that mainly appear in the sampled points. We summarize in figure 24 the main features of TA collected in these points. Unexposed doped sample exhibits a long positive signal at 490nm, a short negative signal at 670 nm which becomes positive after 2 ps, while a double positive signal at 530 and 660 nm with time decay around 30 ps was delineated. In addition, short negative signals at around 770 and 810 nm can be evidenced for this sample. All the mentioned results are reported in figure 24a-c.

For exposed doped sample, the interaction with UV light for 20 h reveals a positive double signal similar to the one discussed for the

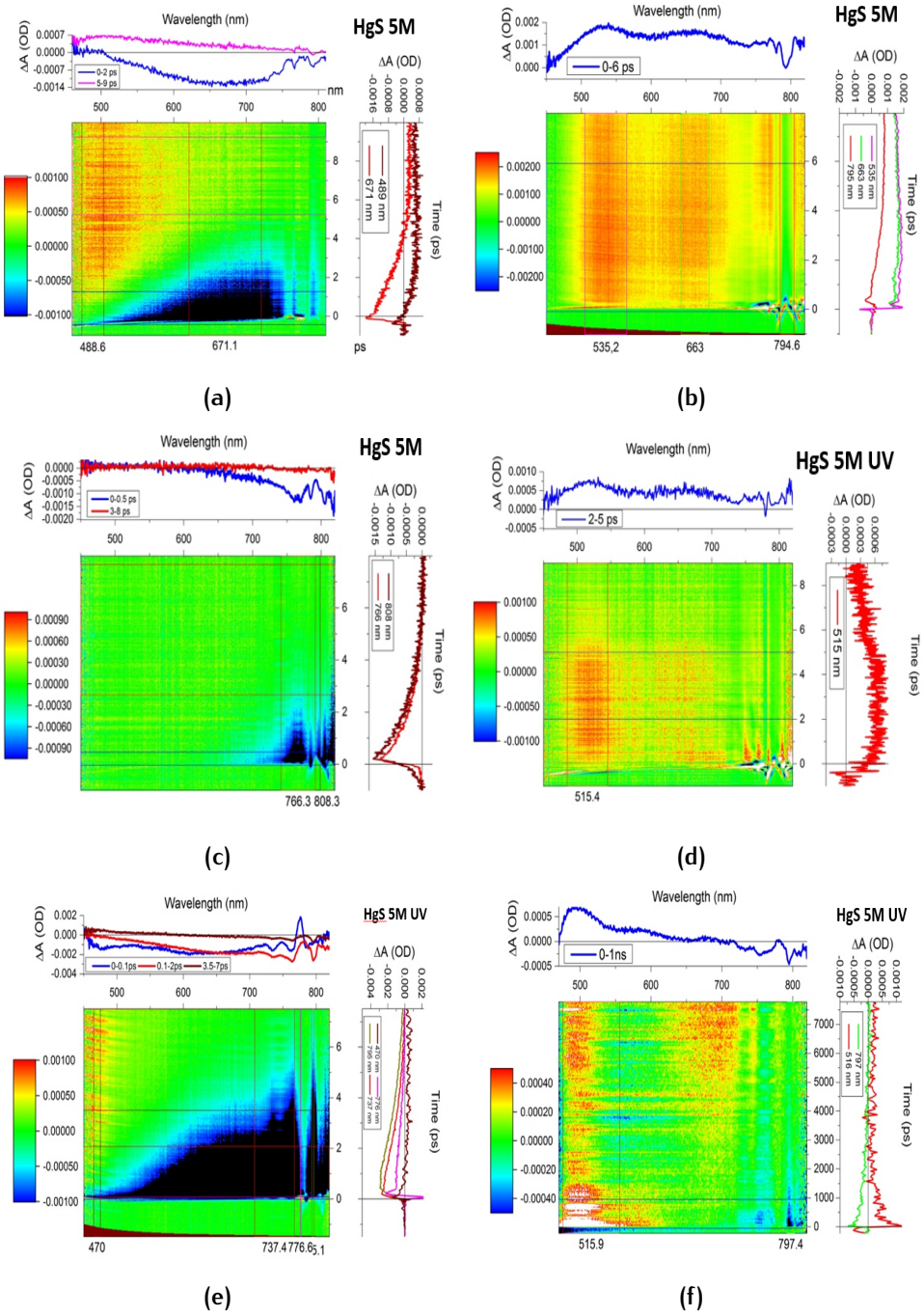

Figure 24: Transient absorption maps, wavelength and time profiles of 5M doped samples: unexposed point 1(a); unexposed point 2(b); unexposed point 3(c); exposed point 1(d); exposed point 2 (e); exposed observed in long-time range (f).

not irradiated sample, peaked at the same wavelengths, but with reduced decay time of 15 ps (figure 24d). At low pump power (50 μW) the sample shows short negative signals at 740 nm and 795 nm which end after 6 ps. Under the same low pump power condition, a very short positive signal is observed at 776 nm (figure 24e).

The relevant variation with respect to the unexposed samples, ob-

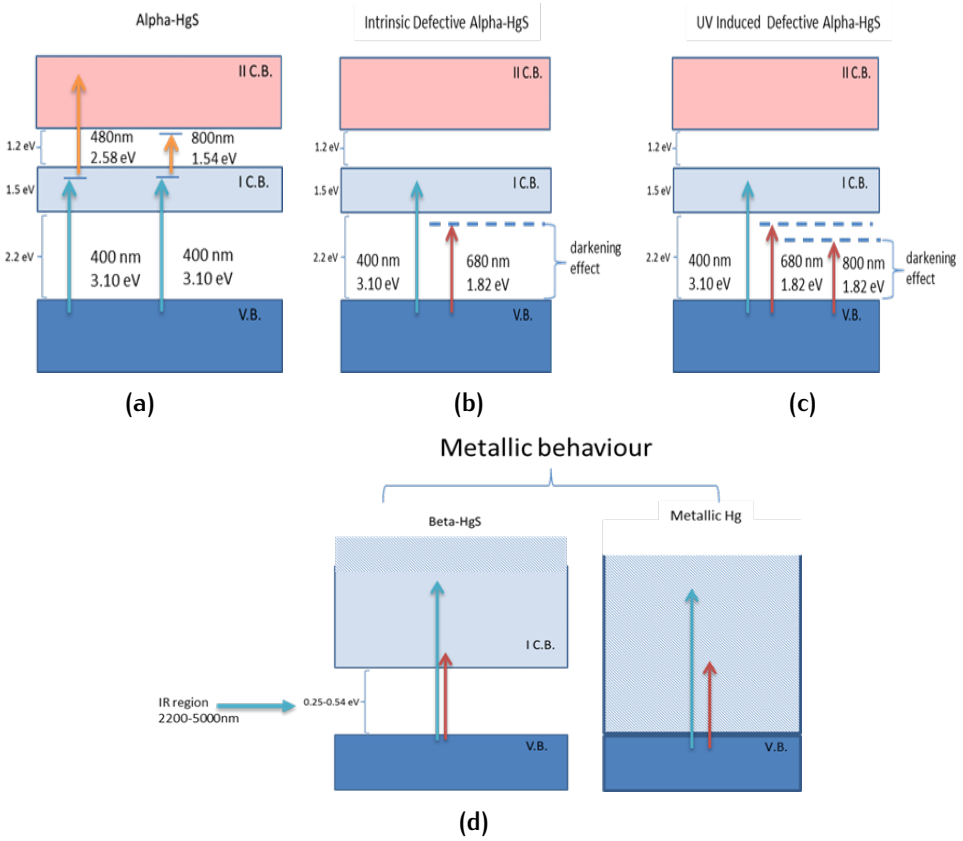

Figure 25: Reconstruction of darkening process in the band structure sketches of HgS phases by means of ESA and GSD transitions from TA maps: alpha phase (a); addition of shallow traps in intrinsic defective alpha-HgS (b); UV induced defects in alpha-HgS (c); metallic behaviour of beta-HgS and metallic Hg (d).

served also in pure series, is the presence of long signals, positive and negative, in the range of ns. In particular, we observed a positive signal at 480 nm with a decay time of around 1 ns and a negative signal at 797 nm with a decay time of 3 ns. We reported these results in figure 24f.

In summary, the presence of chlorine ions seem to not change the structure of the alpha-phase, since only small variations in the GSD spectra and characteristic decay times are revealed. In fact, as can be seen in figures 24c and 24e, well-defined negative bands between 700 and 800 nm which can be ascribed to the presence of further trap centers due to the Cl- ions in the structure. Even the UV treatment does not display an evident difference between doped and undoped samples, except for a shortening of characteristic decay times of involved transitions.

Most important, all the transitions involved in pump–probe measurement do not appear as compatible with the formation of other chlorine-based phases like calomel or mercury chloride which present a higher band gap than pure cinnabar. Only the corderoite phase

could have a possible matching since its band gap at 2.90 eV is compatible with the revealed ESA signals, but in that case the formation of deep traps at 1.82 eV and 1.54 eV could hardly explain the observed darkening phenomena and the recorded changes in the kinetics of the absorption features.

Band gap calculations

Following the just proposed comments, we calculated the band gap for the experimental samples starting from the Reflectance spectrum and by elaborating the Tauc plots for Kubelka Munk function [104, 105] expressed in equation 11:

$$F(R) = \frac{(1-R)^2}{2R} \tag{11}$$

Figure 26 displays the results obtained in samples before and after the UV treatment, evidencing the transition to a phase with a reduced gap. In particular, we reported in the figure the direct and indirect transitions for all the samples that are summarized in Table 3. Upon

Sample	Direct transition [eV]	Indirect transition[eV]
Pure HgS NO UV	2.05	1.97
Pure HgS UV	1.92	1.57
5M HgS NO UV	2.08	1.93
5M HgS UV	2.01	1.77

Table 3: Direct and indirect transitions values for all the samples calculated from figure 26 before and after UV exposure.

UV irradiation, pure HgS transitions move from 2.05 eV to 1.92 eV for direct transitions and from 1.97 eV to 1.57 eV for indirect transitions. The HgS 5M sample changes the transitions from 2.08 eV to 2.01 eV (direct) and from 1.93 eV to 1.77 eV (indirect). These values are compatible with GSD signals obtained by pump-probe and a similar trend evidenced in the first derivative reflectance spectrum (figure 21), where two satellite broad bands are indicated at 650 nm and 740 nm. We underline that the presence of indirect transitions justifies the time extension of pump-probe signal from picoseconds to the nanosecond regime.

Actually, as suggested by several authors [106–108], a phonon assisted recombination for these indirect transitions influences the time of the entire process, especially the absorption of free carriers. Indeed, as studied by Cooper et al.[78], the change of differential absorption coefficient $d\alpha$ is a function of both photon energy and time (Eq. 12):

$$d\alpha(E,t) = \frac{4\pi}{\lambda}(d\kappa_{\Delta E_g} + d\kappa_{\Gamma} + \kappa_{Drude}) \tag{12}$$

As evidenced in equation 12, the change of the extinction coefficient depends on the shifting of the band gap ($d\kappa_{\Delta E_g}$), broadening of the

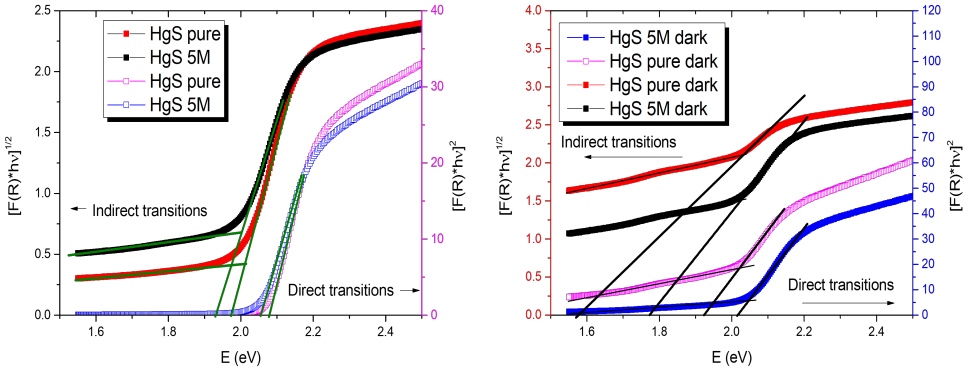

(a) (b)

Figure 26: Tauc Plots for Kubelka Munk function from Reflectance spectra of analyzed samples: direct and indirect transitions for pure and doped samples not exposed to UV light (a); direct and indirect transitions for UV exposed pure and doped samples (b).

band gap $d\kappa_\Gamma$, and Drude-like free-carrier absorption κ_{Drude} components. This equation is related to the experimental differential optical density (dOD) through the Beer-Lambert law. In particular, following the recent study by Cooper, the time dependence of dOD can be determined by the sum of two terms:

$$dOD(\lambda, t) = dOD(t) + Q(t)dOD_{thermal} \tag{13}$$

which represent, respectively, the contribution of above-mentioned extinction coefficient parameters and a time-dependent weighted function $(Q(t))$of thermal contributions. Cooper hypothesized that the temporal evolution in the picosecond regime is dominated by a relaxation of hot photo-excited carriers which occurs primarily through carrier/carrier scattering. Conversely, carrier/lattice scattering and consequent dissipation to lattice heating occur in a second time up to the nanoseconds regime. This trend is consistent with our experimental results and could explain the change of time range associated to the band gap reduction causing the darkening macro effect. In addition, the carrier/lattice scattering is favorable in the transition to quasi metal (beta phase) or metal nature (metallic Hg), where phonon assisted recombination and lattice heating occur efficiently.

The role of chlorine ions in HgS deserves a brief discussion in order to summarize the effects produced in the process. In terms of TA, chlorine ions do not cause a particular effect in ESA or GSD signals in samples without UV exposure. For what concerns the doped sample after UV irradiation we evidenced a lower threshold for short GSD and a higher threshold for long GSD and ESA signals. The spectral

positions of intermediate states which origin the optical transition seem not to change with the presence of chlorine ions.
To conclude our analysis, Tauc plots confirm the presence of alpha-cinnabar with a defective phase, but the formation of other chlorine-based compounds having a band gap over 2.0 eV seems to be ruled out, since all the mentioned possible Cl related structures, corderoite, calomel and mercury chloride, are endowed with higher values of band gap.

Fluence dependence

The power range used for this study was chosen following a fluence study of the TA signal, as HgS is a semiconductor, so its optical properties (especially the charge carrier dynamics) depend strongly on the carrier density (and hence the illumination power). Subsequently, we opted for the minimum required power to observe a TA signal to avoid inducing sample alteration. In figure 27 TA signals and characteristic times as a function of injection fluence derived from pump power is proposed.

At low fluence, the GSD is the most predominant phenomenon. In this process, a fraction of carriers' number is promoted in the excited state, while the carriers' amount in the ground state decreases leading to a negative signal of TA. In the first fluence range, signal intensities and characteristic times follow a linear trend as a function of pump power, while as the laser fluence increases we observed a saturation of these observables and, in some cases, an inversion in the trend. This phenomenon is well known in literature [109]: at higher laser fluences, the third-order non-linear effects such as absorption saturation, exciton-exciton annihilation, Auger processes, and excited-state absorption are prominent. During such non-linear excitation phenomena, the excited states may get fully filled (near full bleach of the ground state) leading to TA signal saturation and even a trend inversion. Indeed, the GSD lifetimes in the present case show a decreasing trend with an increase of laser fluence, which further suggests the involvement of third-order non-linear effects.
In figure 27a, a trend of the saturation model for the intensity dependence of the transient absorption of a material was fitted using the fallowing equation, as reported in the literature [110–113]:

$$\Delta\alpha(F) = \frac{\Delta\alpha_0(F_0)}{(1 + F/F_s)} + \beta F \tag{14}$$

where $\Delta\alpha(F)$ is the fluence-dependent TA, $\Delta\alpha_0(F_0)$ is the TA when the fluence is close to zero, F is the pump fluence, Fs is the saturation flu-

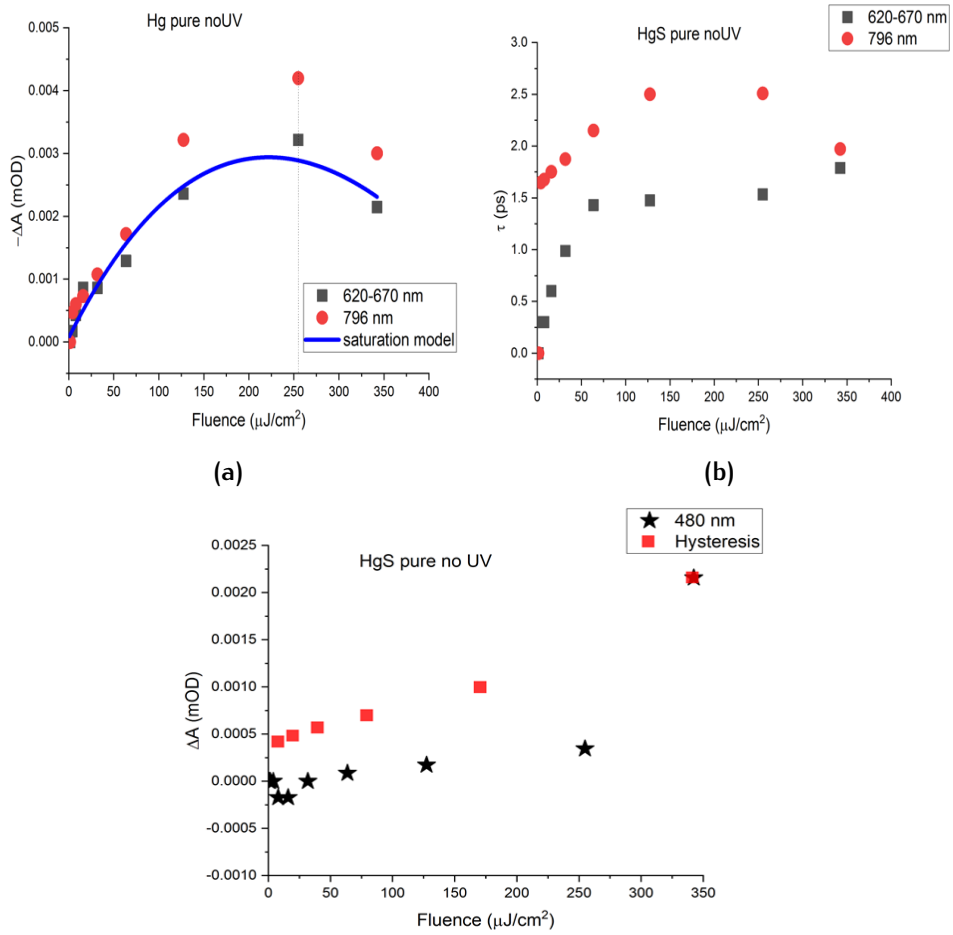

Figure 27: Fluence dependence of TA (GSD) at different spectral regions. Saturation model is preliminary reported in a) (blue line).

ence of the material, while β, predominant at high fluence, expresses other non-linear processes due to two-photon absorption.

Concerning the ESA signal, we analysed in detail the 480nm transition in unexposed pure sample (see figure 27c). In this case a non-linear scaling with pump power is recorded, with a threshold around $200\mu W$ (fluence of $70\mu J/cm^2$), further confirming the involvement of non-linear processes. In addition, a hysteresis, a possible permanent changes once the threshold is reached, of this signal is evident, in fact the same ESA signal recorded after $200\mu W$ shows higher values at lower fluence irradiation.

2.1.4 Density Functional Theory calculations

Quantum-mechanical calculation were performed by means of the Quantum- Espresso package [114] based on density-functional theory (DFT), periodic-boundary conditions, plane-wave basis sets, and

pseudo-potentials to represent the ion-electron interactions. The local density approximation (LDA) with the Slater exchange and Perdew-Zunger [115] correlation were used together with PAW pseudo-potentials [116, 117]. The electronic Kohn Sham wave functions were expanded using a plane wave basis set, up to a kinetic energy cut-off of 29Ry. Monkhorst-Pack grids were used to sample the Brillouin zone, 444-point was used. The structures were fully relaxed to their equilibrium configuration through the calculation of the forces on atoms and the stress tensor. In the relaxed equilibrium configuration, the forces are less than 0.004 eV/Å and the deviation of the stress tensor from a diagonal hydrostatic form is less than 0.5 kbar.

In order to shed light on the nature of the experimentally observed traps, and with the intention to confirm the phase transition, we performed a DFT calculation starting from literature and following our previous work where the S vacancies led to an excess of Hg [97].

The initial structure of Alpha-HgS, obtained from single crystal data, was fully optimized to the equilibrium positions and the supercell containing 48 atoms was relaxed to a target pressure smaller than 0.5kbar. The corresponding optimized lattice parameters a and c were found to be respectively a= 4.225 Å and c=9.7678 Å which agree to better than 3% with the experimental values of a=4.15 Å and c=9.5 Å [86]. Starting from the Alpha-HgS optimized structure, we esti-

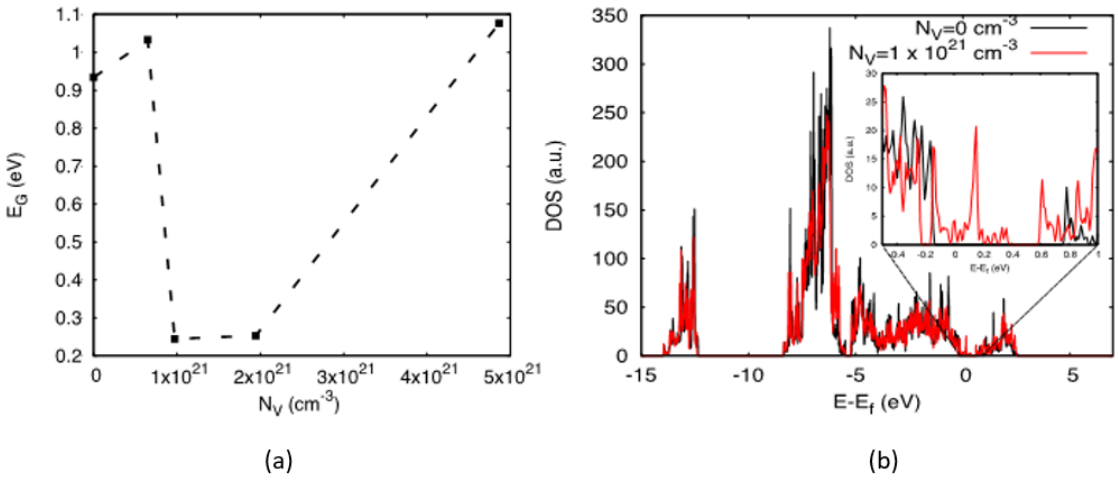

Figure 28: (a)DFT calculation of energy gap of alpha-HgS as a function of S vacancies in the structure; (b) Electronic density of states for pristine HgS and number of vacancies NV = $1x10^{21}cm^{-3}$.

mated the corresponding band structures by means of the Quantum-espresso package. The calculations show an indirect energy gap of 0.93 eV which is considerably smaller than the corresponding experimentally gap of 2.25 eV [118].
The energy gap underestimation is a well-known DFT problem which appears when local density functionals are used in the calculations.

In order to characterize the effects of point defects on the alpha-HgS optical properties, we performed a series of band-structure calculations on alpha-HgS having an increasing density of S vacancy in the range $6.5x10^{20} - 4.9x10^{21} cm^{-3}$. Figure 28a shows the alpha-HgS energy gap as a function of the vacancy concentration. We observe an overall non-monotonic energy-gap (EG) in relation to the number of vacancies (NV). For NV up to $6.5x10^{20} cm^{-3}$ the EG does not significantly change with respect to pristine alpha-HgS. On the other hand, by increasing NV in the range $1 - 2x10^{21} cm^{-3}$, we observe a significant EG reduction down to 0.25 eV, suggesting a possible transition to the beta-phase. We attribute such an energy gap reduction to the occurrence of spurious vacancy energy levels within the energy band gap. This hypothesis is confirmed in Fig. 28b, where the electronic density of states is plotted for pristine HgS and for NV=$1x10^{21} cm^{-3}$. The inset clearly indicates the presence of energy vacancy levels positioned within the energy gap which is therefore reduced down to a value of 0.25 eV. Finally, for NV=$4x10^{21} cm^{-3}$, we observe an unexpected EG increase up to 1.1 eV. However, by analyzing the corresponding HgS structure we observe an overall lack of hexagonal crystallinity being the system mostly amorphous.

2.1.5 Synopsis of the obtained results

In the previous sections, transient absorption on pure HgS and chlorine doped HgS samples was used to characterize the optical properties of Red Vermilion in relation to the darkening effect studied in literature. The results were compared with those obtained in samples exposed to UV light which presented evident blackening of their original color.

Pump probe measurements reveal positive and negative signals ascribed to a broad short GSD at 680 nm and ESA at 480-500 nm. The former is attributed to the presence of traps (0.2 eV from the bottom of the first conduction band) in a "defective" phase, the latter to transitions from the first to the second conduction band. In particular, with the intention to explain the darkening phenomenon, the GSD signals were also studied in UV exposed samples which reveal, beyond the short GSD, the presence of long a GSD at 780-800 nm compatible with a phonon-assisted transition. This behavior is compatible with indirect transitions which explain the reduction of the band gap and reflect the darkening process. Actually, for UV exposed samples the analysis of Tauc plots from Kubelka Munk function of reflectance spectra reveals a band gap change from around 2.0 eV to 1.57 eV for pure HgS and from around 2.0 eV to 1.77 eV for 5M HgS.

The results are in agreement with DFT simulations that show a progressive reduction of the energy gap as a function of S vacancies in

the cell of alpha-HgS structure. The formation of intra-gap defect levels is also confirmed. In addition, all the transitions involved in pump–probe measurement do not appear as compatible with the formation of other chlorine-based phases, confirm our previous results, obtained with the use of Raman spectroscopy, where a kinetic model of phase transition from cinnabar to beta-cinnabar and metallic Hg was proposed.

2.2 CASE STUDIO: Cd-PIGMENTS

During the nineteenth century, new inorganic pigments were synthesized and used extensively by coeval artists [119, 120] for their characteristics, such as high color intensity, low cost, and covering power; they substituted the well-known ancient pigments in numerous Impressionist and early Modernist paintings. Cadmium yellow degradation afflicts numerous paintings realized between the XIX^{th} and XX^{th} centuries of many famous artists, such as Pablo Picasso, Vincent Van Gogh, Georges Seurat, Henri Matisse, Ferdinand Leger, Edvard Munch, and James Ensor [121–125]. The degradation process and its kinetics is not completely understood. It consists of chalking, lightening, flaking, spalling, and, in its most deteriorated cases, the formation of a crust over the original yellow [122].

In this section, to understand the degradation process of CdS pigments, the effect of calcination, the role of inner defects, and to clarify which degradation products could be originated, we simulated several artificial ageing processes on two kinds of CdS commercial samples: the yellow and orange ones. Both of them are also studied in combination with the binder and the canvas, to make mock-ups of oil on canvas painting, to discriminate which elements create the "fading/chalking" phenomena, which further degrades with whitish compounds or dark crusts, and who is the major responsible for color changes in paints. Also for these pigments, the degradation process can be studied and linked to the presence of a distribution of some electronic levels due to color centers, associated with point defects, from which the nucleation process can start, complementing conventional diagnostic techniques with pump and probe.

2.2.1 Cd-pigments structure and synthesis

Yellow cadmium pigment is constituted by a cadmium sulfide (CdS) semiconductor, presenting both crystalline and amorphous forms. The hexagonal phase (α-CdS) is found in nature as the mineral greenockite, with space group $P6_3mc$, the cubic structure belongs to the space group $F\bar{4}3m$ (β-CdS), known as hawleyite mineral [126], while the amorphous form is a chemically synthesized product.

The synthesis procedure can be divided into wet and dry processes. The latter could have, as starting materials, cadmium oxide, cadmium metal, or cadmium carbonate, each of which can be mixed with sulfur and heated to 300°C–500°C in the absence of air. The wet process consists in a solution with soluble sulfide (such as hydrogen sulfide, sodium sulfide, or barium sulfide) and soluble cadmium salts, such as chloride, cadmium nitrate, cadmium sulfate, or cadmium iodide, with a final precipitation of CdS [121]. During the 20^{th} century, to

produce different hues from the light yellow typical of CdS, its synthesis started to be changed by inserting zinc to lighten the color and selenium to increase the red hue.

2.2.2 Degradation pathway and final products

Many studies were performed on Impressionist paints to understand the degradation process and identify which degradation products arise. Some authors [121] suggesting that the degradation process appears to have affected only the material that is in direct contact with moisture and (UV) light, so the degradation process is due to oxidation in the CdS pigment, with the final formation of cadmium sulfate as a degradation product.

In [123, 124] the authors suggested the presence of cadmium carbonate as a secondary degradation product following the primary photo-degradation of CdS, perhaps by the capture of atmospheric CO_2, or a tertiary process involving a further breakdown in cadmium oxalate into cadmium carbonate.

Other degradation products individuated in degraded paints are cadmium oxalate, cadmium sulphate hydrate, and cadmium oxide. All of them can be derived from starting materials or filler products in paints but, as asserted by Mass et al. [122], their presence on the surface and not in the depth of the paint layer, is the proof of their degradation character. The cadmium oxalates are concentrated near the surface of the paint layer, demonstrating that this is a photo-oxidation product rather than a paint filler in the cadmium yellow paints. Cadmium sulfates have high solubility, so their presence in traces throughout the paint layer can be explained as mobile photo-oxidation products or, again, as starting reagents.

In addition to paintings, hexagonal CdS is one of the most important semiconductors for high-tech applications, for solar energy harvesting, among others, because of its bandgap around 2.4 eV [127] and calcination studies of synthetic CdS and consequent photo-oxidation by visible light exposure were carried out for this research field [128], in which CdO was detected as final photo-degradation product and it was also found that the calcination treatment decreases the trap states.

The degradation pathway can be summarized with the fallowing reactions. The action of light with energy equal to or higher than CdS band gap leads to the formation of electron-hole pairs:

$$CdS + h\nu \rightarrow e^- + h^+ \tag{15}$$

The holes oxidize the cadmium compound with:

$$CdS + 2h^+ \rightarrow Cd^{2+} + S. \tag{16}$$

At this point, the contact with air oxygen leads to the oxidation of sulfur to sulfate:

$$CdS + 2O_2 \rightarrow Cd^{2+} + SO_4^{2-} \tag{17}$$

More generally, the paint's exposure to moisture and air can lead to a fading in yellow with the formation of cadmium sulfate hydrate, as confirmed by XRD measurements in [121]. Therefore, the chemical reaction is:

$$CdS + 2O_2 + H_2O \rightarrow CdSO_4 \cdot H_2O \tag{18}$$

L. Monico et al. proposed another mechanism of sulfate formation considering the action of surface holes [129]:

$$CdS + 4h^+_{surf} + 2H_2O + O_2 \rightarrow CdSO_4 + 4H^+ \tag{19}$$

2.2.3 Materials and Methods

Analytical methodology

CdS is a pigment typically used in oil paintings. In order to understand and explain the typical elements and degradation factors found in the literature, an accelerated degradation study was carried out on each component element of a painting. The first step was to characterize only the pigment powders after thermal and optical degradation processes. Subsequently, the role of the binder and canvas when pigment is mixed with them was studied. The determination of degradation products, colour changes and optical variations were studied by means of various optical and analytical techniques such as Raman spectroscopy, SEM, XRD, reflectivity, luminescence and transient absorption.

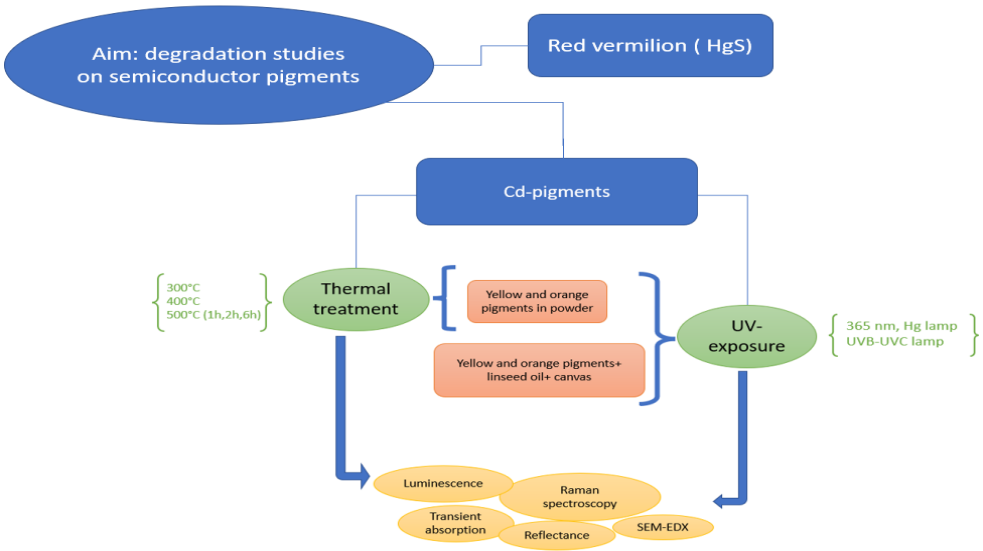

Figure 29: Schematic representation of the methodology followed for the degradation study of Cd-pigments.

Samples in powders

Cd-pigments used for accelerated degradation studies were bought from Kremer pigments. We used pigments number 21040 (white yellow) and 21080 (orange) and called them C-A and S-A respectively. The artificially aged samples were named with the initial C or S to indicate the yellow or orange paints, followed by a number indicating the temperature of heat treatment (300-400-500) and duration of heating (1h, 2h, 6h). With the "UV" term we expressed the UV exposure realized by Hg lamp, with wavelength at 365 nm, followed by the relative exposure time (in hours) up to 56 hours with a density power of $7mW/cm^2$.
The thermal treatment is obtained using a temperature range between 300 and 500°C for different heating times (1h, 2h, 4h, 6h). Their chromatic and structural variation were measured with micro-Raman spectroscopy, reflectance, TR-PL spectroscopy, X-ray diffraction, and transient absorption. Then these samples (and those without treatment) were stored at room temperature, 50% relative humidity (RH) in contact with air, illuminated by ambient light from Compact Fluorescent Lamps (CFL) for 4h/day for 6 months.
To perform UV exposure the acquired powder was mixed with distilled water and dispersed on a slide. The sample was exposed with Hg-lamp combined with a filter to remove the visible components and leave mainly the 365 nm component. The exposure was made at room temperature and with an RH value of 50%. The reflectance spectra were collected by step of 8 hours a day and the other measurements are made only on the raw samples and at the end of the process for a total period of three weeks of air exposure.

Sole binder and Mock-ups of oil on canvas

The degradation process of binder (linseed oil acquired by Zecchi Company) was made by deposition of oil on a slide and exposed to UV radiation (365 nm) of filtered Hg lamp for different hours with P=$60mW/cm^2$.

We also realized mock-ups of oil on canvas. The canvas samples were of two typologies: painted only with oil and a composition of oil plus pigments in the previous mass ratio of 0.5:1. The degradation process was realized with a deuterium lamp as previously indicated. One canvas was exposed for 5 days and after this period stored in the dark at room temperature, and 50% RH, leaving it in contact with air for 15 days. The second one was kept under continuous UVC-exposure of the deuterium lamp for 15 days, at room temperature and 50% RH. Reflectance spectra were collected at different steps of 24 h and 48 h of UV-exposure, while Raman spectra at the starting and endpoint of each degradation process. These kinds of samples

are named O-canvas-, C-canvas-, S-canvas- followed also in this case by the time of exposure.

Time-Resolved Photoluminescence (TR-PL)

TR-PL measurements were recorded by using different excitation systems. One excitation with 100 fs long pulses delivered by an optical parametric amplifier (Light Conversion TOPAS-800-fs-UV-1) pumped by a regenerative Ti:sapphire am-plifier (Coherent Libra-F-1K-HE230). The repetition frequency was 1 kHz. The second excitation with 100 fs long pulses from Ti:sapphire oscillator Coherent Chameleon Ultra II having a repetition rate of 80 MHz. PL signal was recovered by a streak camera (Hamamatsu C10910) equipped with a grating spectrometer (Princeton Instruments Acton Spectra Pro SP-2300). All of the measurements were collected in the front-face configuration to reduce inner-filter effects. Proper optical filters were applied to remove the reflected contribution of the excitation light.

2.2.4 Results

Heating process

The starting pigments were characterized first by XRD to obtain information about the phase composition and additive compounds. At a later time, a second analysis with reflectance and Raman spectroscopy was conducted to have more detail on structural modifications during the aging process.
XRD analyses revealed the presence of barium sulfate (see figure 30a), in a percentage of about 7(1)% with respect to the remaining $Cd_{1-x}Zn_xS$ in yellow cadmium (x=0.19). The orange one revealed the presence of hexagonal $CdS_{1-x}Se_x$ and CdS (figure 30b). The phase identification confirms the mixture of CdZnS and $BaSO_4$ for yellow C-samples and CdSeS for orange S-samples. Thermal treatments on the two mentioned samples, C-A and S-A, were made at different temperatures ($300°C, 400°C, 500°C$) for 1h and, for the 500° C temperature, we performed the calcination also for 2h, 4h, and 6h until obtaining a notable chromatic change.
The XRD measurements performed for the samples heated at $300 - 400 - 500°C$ for 1 hour are reported in Figure 30a and 30b. As displayed in the patterns, a perceptible difference is shown only in the C-500- 1h curve, in which a broadening of the region between 24 and 34° is present. This broadening could be associated with an increase in structural disorder related only to the CdZnS compound. Actually, studies in the literature on thermal stability on $BaSO_4$ demonstrate that its XRD pattern did not change for this compound [130]. Contrary to what was discussed in the introduction, no evidence can be

reported in this analysis about the formation of other compounds, such as $CdSO_4$ and CdO. Only in the case of heat treatment at 500°C

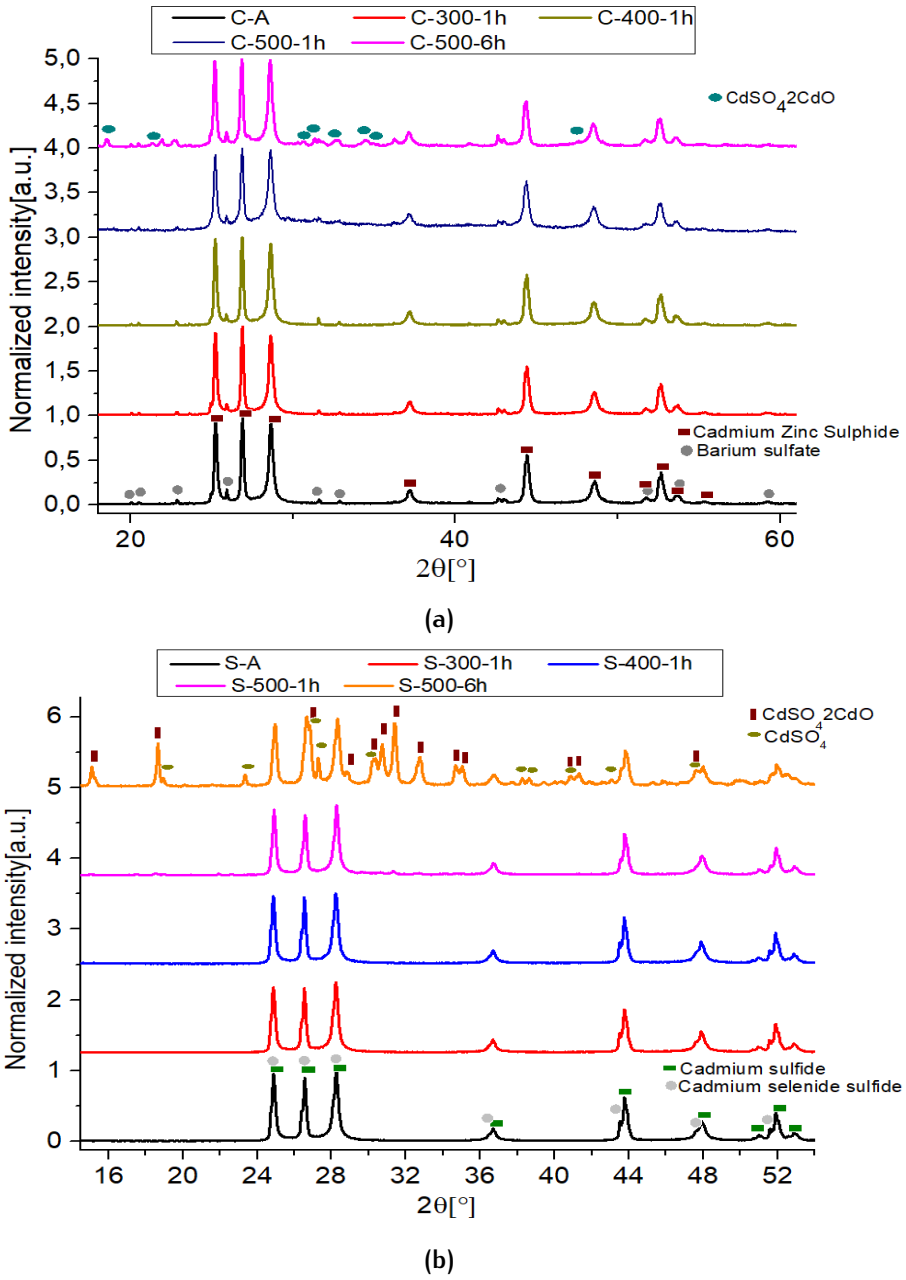

Figure 30: (a) XRD patterns of C-A heated and no-aged samples; (b) XRD patterns of S-A heated and no-aged samples.

for 6h, the formation of these compounds is detected, justifying the observed change in color. Actually, by increasing the heating time to 6 hours at 500°C, the XRD measurements were able to detect the degradation products. As can be seen from Figure 30a and 30b, the C-500-6h patterns show peaks of $CdSO_4 \cdot 2CdO$ and in the S-500-6h sample, also the presence of a pure Cd-sulfate phase. The chromatic variation among the samples was measured from the reflectance spectra. The first derivative spectra for the yellow cadmium are shown in

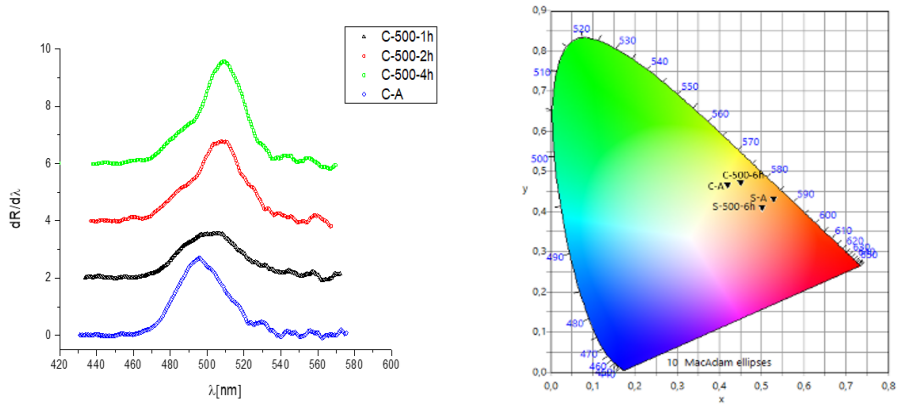

(a) (b)

Figure 31: (a) first derivative reflectance spectra for heated C-A samples; and (b) the color chart of C-A, S-A , C-500-6h, and S-500-6h samples.

Figure 31a and the strongest variations recorded at 500°C after 6h are summed up in the CIE color chart in Figure 31b. The calculated CIE coordinates, relative simulated colors, and the maximum value of the first derivative (X_0) are listed in table 4.

By heating the C-A sample, a notable shift in X_0 towards high wave-

Sample	L	a	b	Xo[nm]	Simulated color
C-A	94,1	-11,1	101	496.9	
C-300C-1h	103	-17,3	101	494,2	
C-400C-1h	93,7	-8,89	101	497,7	
C-500C-1h	85,8	-5.08	75.6	502.3	

(a)

Sample	L	a	b	Xo[nm]	Simulated color
S-A	78,2	35,3	92,6	514.5 , 556	
S-300C-1h	92,2	42,4	107	512,553	
S-400C-1h	76,8	28,4	85,3	514, 552.8	
S-500C-1h	76.4	29.9	89.7	514.3, 552.9	

(b)

Sample	L	a	b	Xo[nm]	Simulated color
C-A	94.1	-11.1	101	496.9	
C-500C-2h	100	-5,91	84	506.4	
C-500C-4h	104	-5,66	99,3	508	
C-500C-6h	91	-0.81	86.9	511	

(c)

Sample	L	a	b	Xo[nm]	Simulated color
S-A	78.2	35.3	92.6	514.5, 556	
S-500C-2h	89,7	37.1	95	514, 553	
S-500C-4h	91,5	43.2	105	513, 555	
S-500C-6h	70.4	32.1	62.6	515, 556	

(d)

Table 4: Chromatic variation on C-A and S-A samples after heating process obtained by reflectance spectra.

lengths is produced. The shift in the S-sample is not remarkable, as can be seen from the X_0 values in Table 4, where the peaks of the first derivative range from 514.5 and 556 (for the no-treated S-sample) to 515 and 556 (for S-500-6h). As is known from the literature, the X_0-value is linked to the direct bandgap value [131–133], so the shift in sample C is compatible with a decrease in the direct bandgap and it can be explained by the formation of the CdO compound after a thermal treatment, as proved by [128, 134]. On the contrary, reflectance measurements suggest another change: heated samples reveal an increment in the luminosity L parameter in CIE Lab coordinates. This

change could be associated with the formation of whitish compounds, probably $CdSO_4$ [135].
As the calcination time increases, we generally register raise in the L parameter (Table 4) for both S-A and C-A samples.
We can explain this behavior considering that the colorimetric coordinates can be influenced by the combination of grain dimensions with the formation of mentioned compounds, CdO and $CdSO_4$. If the temperature increases, the grain size in the sample is larger (see Comelli et al.) and this means a decrease in luminosity but also a major formation of cadmium sulfate and the presence of a darker compound, such as CdO. Therefore, the effect of the co-presence of a whitish and a darker compound, in addition to the variation in grain sizes of the sample, can influence the variability in the L parameter, which does not follow a linear increase as a function of the heat treatment. Actually, luminosity L decreases again after 6h at 500°C, during which, as hypothesized before, a predominant brownish compound is forming (CdO), inducing a reduction in this parameter.

To confirm this assumption, we performed TR-PL measurements and the results are included in Figure 32a: we reported the emission of C-samples before and after the thermal treatment, where, again, a visible red shift is present. Actually, the peak moves from 480 nm in sample C-A to 510 nm in the sample heated at 500°C for 6 h. In Figure 32b, the TR-PL kinetics for the S-samples that do not present substantial variation as a function of the temperature are shown. A Gaussian deconvolution of the spectra for different temperatures was calculated for sample C and the respective band positions in eV are represented in Table 5.
TR-PL analysis was made on the time scale, ranging from a picoseconds regime to the nanosecond scale, revealing the presence of three decay times derived by three emission channels ($\tau_1, \tau_2 and \tau_3$). In the case of the CA sample, as indicated by previous studies in the literature [136], the shorter time τ_1 around 8–13 ps is attributable to the bandgap emission, while $t_2 < 100$ ps andt_3 of 730 ps are associated with superficial and intermediate structural defects, respectively. While τ_1 and τ_3 times remain constants as a function of the temperature, the intermediate time τ_2 changes assuming a maximum value of 200 ps at 400°C. This behavior seems to be compatible with the formation of CdO nuclei. Actually, in the literature, pure CdO presents two decay times, one in a range of 100–500 ps and one in a range of 1–3 ns [137]. This assumption is not exhaustive for the presence of this compound and a detailed study is necessary to corroborate this hypothesis.

TRPL was performed also in the microseconds range, confirming the presence of deep trap states (TS) emissions [136, 138], with a slow broad emission in the spectral region 650–750 nm and a strong sharp

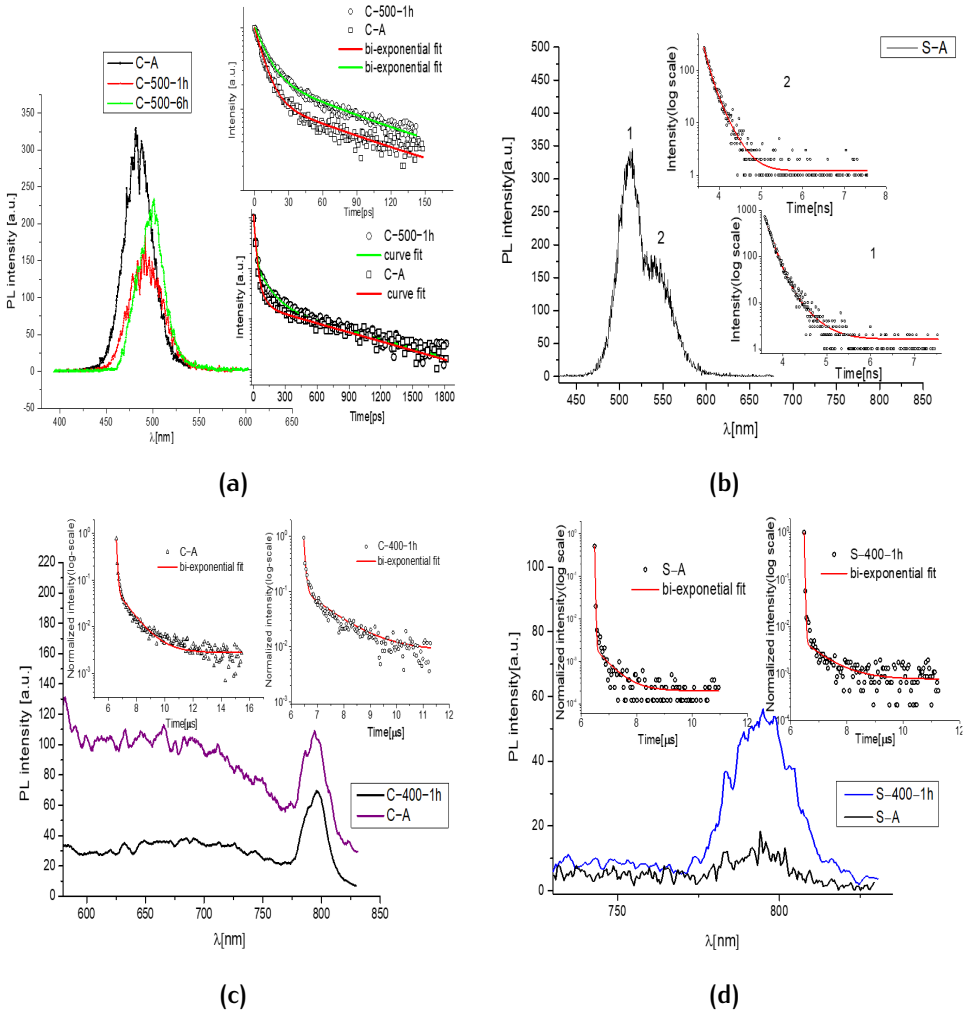

Figure 32: (a) Comparison between the PL emission of C-A sample and the C-samples heated at 500°C for 1 h and for 6 hours and respective decay fits for C-A and C-500-1h samples; (b) TRPL spectra of S-A sample; in inset, the time-resolved spectra of the two bands of emission (one related to CdS and the second to -Se inclusion) with relative bi-exponential decay fit; (c) TRPL microsecond-scale analysis for C-A and C-400-1h samples; in inset, time-resolved fit of 700-800 nm emission band for both the samples; (d) TRPL microsecond-scale analysis for S-A and S-400-1h samples; in inset, time-resolved fit of 700-800 nm emission band.

peak at 790 nm due to crystal defects (see Figure 32c, d). Even using this technique, no evidence of time decays ascribable to $CdSO_4$ can be reported, leaving unresolved the variation in the L parameter discussed before, associated with the formation of a whitish compound. To shed light on this behavior, a complete Raman characterization of the samples, at different wavelengths, was essential to better understand which probable compounds are formed by heating.

For confirming the CdO formation hypothesis, the Raman spectra could not be helpful. In the literature, there are different and contrast-

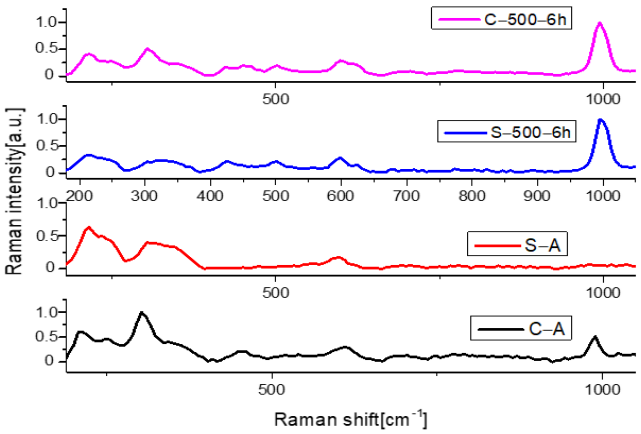

Figure 33: 1064nm excited Raman spectra before and after 500°C for 6h.

Sample	E(eV)	τ_1[ps]	τ_2[ps]	τ_3[ps]
C-A	2.56	8-13	50	730
C-300-1h	2.55	8-13	150	727
C-400-1h	2.56	8-13	200	730
C-500-1h	2.51	8-13	100	728
C-500-6h	2.48	8-13	50	707

Table 5: Value of emission channels for exciting wavelength =450 nm, P=235μW.

ing Raman spectra associated to cadmium oxide [139, 140]; otherwise, according to some authors, cadmium oxide should not be Raman active [141]. Therefore, the individuation of this secondary compound cannot be undoubtedly approved from our Raman spectra.

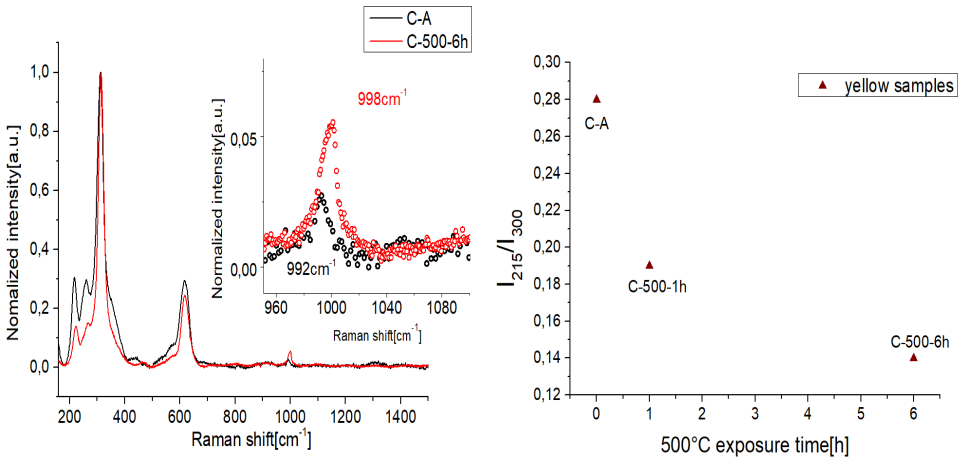

Figure 34: (a) 532nm-Raman spectra of C-A and C-500-6h; in inset, the R.O.I with the value of the peaks obtained by the deconvolution process; (b) Variation in TO/LO bands in high-resolution 532nm excited Raman spectra of yellow samples.

However, the other discussed possible compound was detected. Ac-

tually, the Raman spectrum collected with 1064 nm shows the presence of a big amount of sulfate compound (Figure 33), as demonstrated by the presence of a strong peak around $1000 cm^{-1}$, typical for SO_4 vibration modes. The existence of this band is revealed also in the samples treated at lower temperatures than 500°C. To define, with greater precision, the position of the sulfate vibration and, therefore, to be able to identify the compound, the Raman spectra were acquired with a better resolution ($1 cm^{-1}$), with a 532 nm source.
The Raman spectra with high resolution presented a shift of about $6 cm^{-1}$ between the peaks due to the heat treatment, visible also with the help of a deconvolution procedure by Lorentzian curves around $990–1000 cm^{-1}$(SO_4 vibration), see Figure 34a, confirming the whitish $CdSO_4$ formation.

As previously discussed, no peaks related to CdO and $CdSO_4$ compounds at lower temperature than 500°Care noticeable by XRD, suggesting the possible formation of a thin superficial layer of whitish $CdSO_4$ crust, undetectable with the XRD technique because of the detection limit threshold. Only a broadening in the region between 24°and 34° was revealed, suggesting a progressive structural disorder in the phase CdZnS.
This hypothesis can be confirmed with a detailed analysis of some vibrational modes of the Raman spectra. As reported in the literature [142, 143] the ratio between the 215 cm^{-1} (TO multi-phonon process) and $300 cm^{-1}$(LO) peaks of Cd-pigment Raman spectrum can provide information about the structural disorder, comparing the spectra of the natural and heated samples. In our case, the calculated ratio is drawn in Figure 34b. As reported in [143], the increase in structural disorder and zinc content leads to a decrease of $215 cm^{-1}$ band for the TO mode. In our yellow samples, the heat treatment produces a decrement in TO-peak intensity, as can been seen directly by the spectra reported in Figure 34a, confirming the hypothesis.
Finally, to obtain further confirmation and information about the superficial effect of heating treatment, SEM-EDS measurements were also performed on these two samples. For the sake of brevity, the EDX analysis for each analyzed point of the samples (see figure 35) will not be reported here, but only a summary tables of possible degradation compounds detected. In Table 6, stoichiometric calculations on the element percentages to reach Cd saturation suggest, again, the presence of hydrate sulfate compounds and almost a double amount of Cd-oxide.

UV process

In order to establish the light stability in Cd pigments used in paints, a UV treatment at 365 nm, with different exposure times, was conducted. To characterize the pigment variations, after this degradation

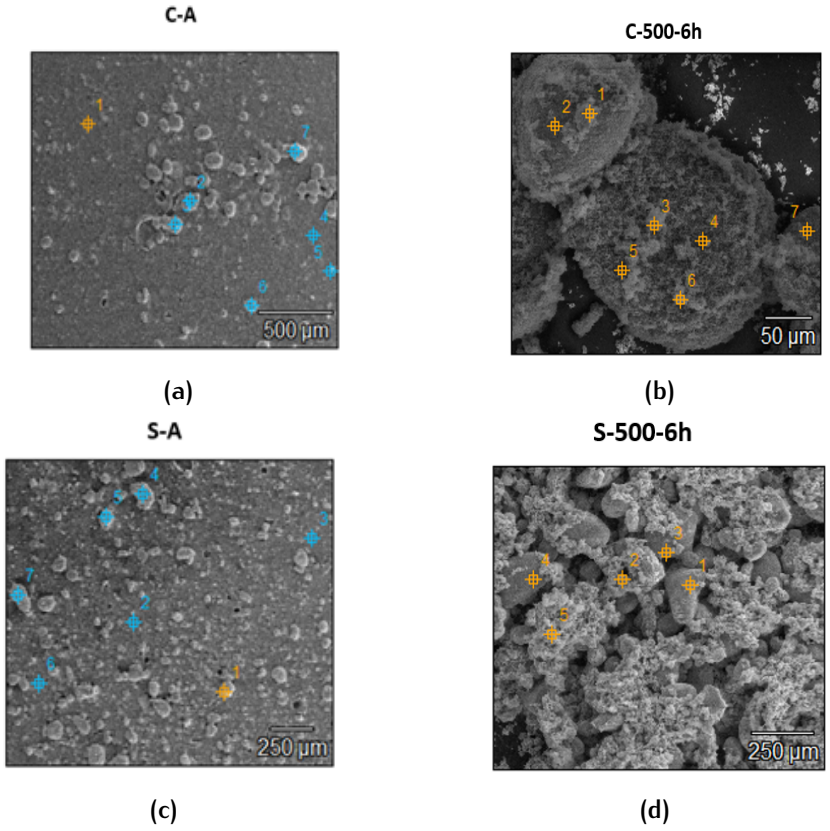

Figure 35: SEM images with points for EDX analyses

	Point 1 [%]	Point 5 [%]
Cd (Se,S)	26.3	27.6
$CdSO_4(8/3H_2O)$	24.4	26.3
CdO	49.3	46.1

(a)

	Point 2 [%]	Point 3 [%]
CdZnS	32.7	38.7
$CdSO_4(8/3H_2O)$	32.2	23.7
CdO	35.1	37.6

(b)

Table 6: Calculation of cadmium saturation for S-500-6h sample (a); and C-500-6h sample (b).

process, we adopted Raman spectroscopy, reflectance, luminescence, and transient absorption. As found in the literature [129], the UV action in the presence of oxygen can produce the formation of sulfate compounds.

In particular, Raman analyses performed on the yellow sample confirmed a broad band in the region of sulfate vibrations between $990cm^{-1}$ and $1008cm^{-1}$ (see Figure 36a). To establish if the new sulfate compound is derived from CdS degradation or if the starting barium sulfate converted to another form, in Figure 36b, the deconvolutions (Lorentzian functions) for the artificially and no-degraded samples are presented in the region of interest (R.O.I). The C-UV-56h signal consists of two peaks, one located at $994cm^{-1}$ with an area of 0.89 and the other one at 1007 cm^{-1} with an area of 0.5. The former is very similar to the one of the C-A band (grey line) located at $992cm^{-1}$

C-UV-56h	Point 1[%]	Point 2[%]
CdZnS	13.3	64
CdSO4(8/3H2O)	86.7	36
CdO	-	-
-S2- in excess	1.3	1.7

Table 7: Calculated Cd-compound percentage by saturation of Cd-amount.

(attributed to $BaSO_4$). The deconvolution procedure presents a slight red shifting and about a doubling of the relative area, suggesting a conversion of barium sulfate to another form. The latter can be associated with CdS degradation in cadmium sulfate. In fact, the peak at 1007 cm^{-1} is usually associated with cadmium sulfate compounds bound with the xH_2O molecule [144].

To confirm the formation of this species, a compositional analysis by means of SEM-EDS was made. For the C-UV-56h sample, the results summarized in Table 7 confirm the presence of Cadmium hydrate sulfate and a possible excess of $-S_2^-$, suggesting the formation of a notable amount of Cd vacancies inside the CdS crystal after light exposure. This is another known cause for the color change in the Cd pigment, as previously reported in the literature [145]. Actually, the Cd vacancies led to the formation of an intra-gap level with NIR emission and time decays of some microseconds, as already discussed before in the case of thermally treated samples.

With the intention of determining the real effect of color change,

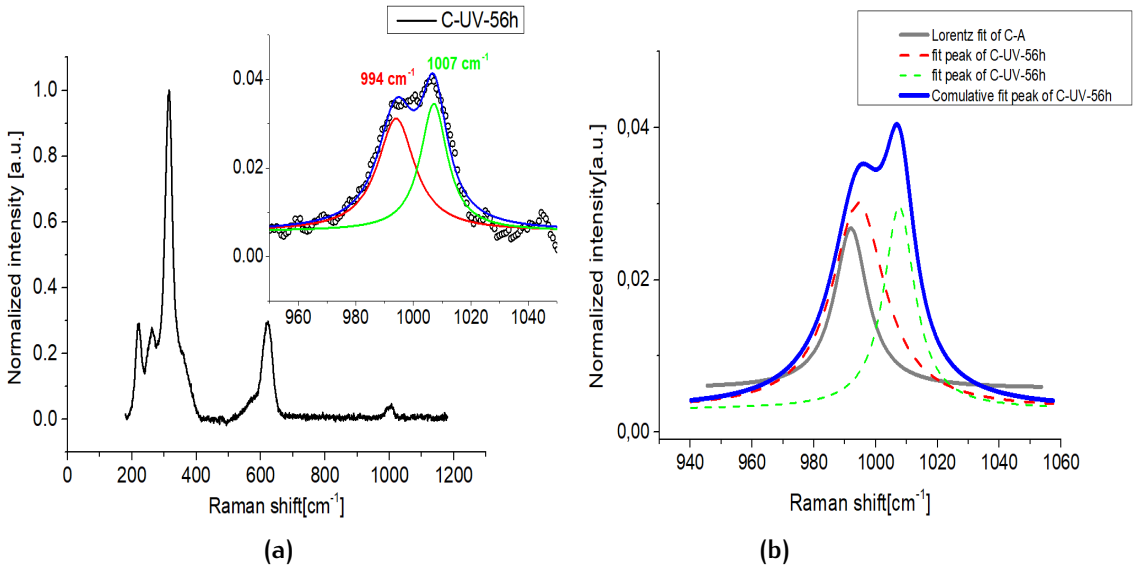

Figure 36: (a) Raman spectrum of C-UV-56h sample with 532 nm excitation wavelength; in inset, the deconvolution of the region of sulfate; (b) deconvolution of the region 900–1060 cm^{-1} of C-A Raman spectrum.

a detailed colorimetric analysis was performed. Reflectance spectra

were collected with 8 h steps of UV exposure and the related CIE Lab coordinates were calculated. The L parameter tends to increase (fig 37a), mainly for the C-A sample with light exposure and the shape of the first derivative, after 56 h, widens, showing a blue shift, typical of the addition of light and white shades in yellow pigments, as studied by Gueli et al. [135]. The total variation in CIE coordinates is represented in CIE space (fig 37b). The S-A sample did not show a remarkable difference in CIE coordinates after 56 h of UV exposure as visible from the color space diagram. To speed up the reading of chromatic variations, a graph with the relative value for each coordinate is shown in Figure 37a, where we tried to express the amount of the total color variation by the ΔE value through a first kinetic model (exponential fit) for the C-A sample:

$$\Delta E = A(1 - e^{(-t/\tau)}) \tag{20}$$

where A is the asymptotic value of the ΔE curve (the final step of conversion of CdS to $CdSO_4$, involving the chromatic change from yellow colors to white ones) and tau is the characteristic time of reaction. After a time of about 40 h, the conversion is completed.

To understand what UV light accomplishes in the process, we monitored the stability of the studied pigments, kept in standard environmental conditions, and we observed that, effectively, the degradation also started slowly in a natural way. After a deposition above a slide, the samples, heated and no-heated (Figure 38), were kept at room temperature with 50 RH%, illuminated by artificial light (Compact Fluorescence Lamps) for 4h/days for 6 months. NIR-Raman spectra were acquired showing the development of a new shoulder in the sulphate region.

In Figure 38, the deconvolution of this region is represented. Even in this case, the formation of sulphate compounds was recorded, revealing that the action of light and mainly of the oxygen leads to degradation in Cd pigments. The optical variations registered on cadmium yellow can be explained in detail with an in-depth study of the electronic properties of this pigment and its behavior after the accelerated degradation process.

For this reason, we characterized, with pump–probe spectroscopy, the optical differences induced in our samples after UV exposure and heat treatment. To clarify the used nomenclature, we will describe, as a short-lived signal, those that last some picoseconds up to tens of picoseconds and long-lived signals, those ranging from hundreds of ps to ns. As reported in Figure 39a, the C-A sample shows a broad positive signal (excited state absorption—ESA), centered at 477 nm, with a duration of 300ps. In addition, a shorter negative broad signal in the region between 650 nm and up to 800 nm is presented.

As a comparison, thermal treatment at 500°C for 6h drastically

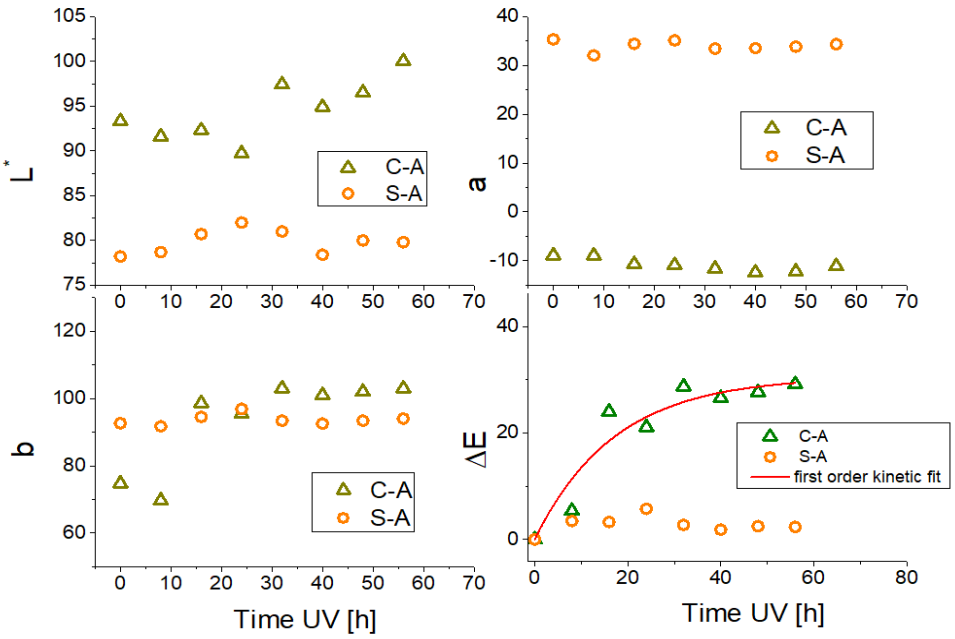

(a)

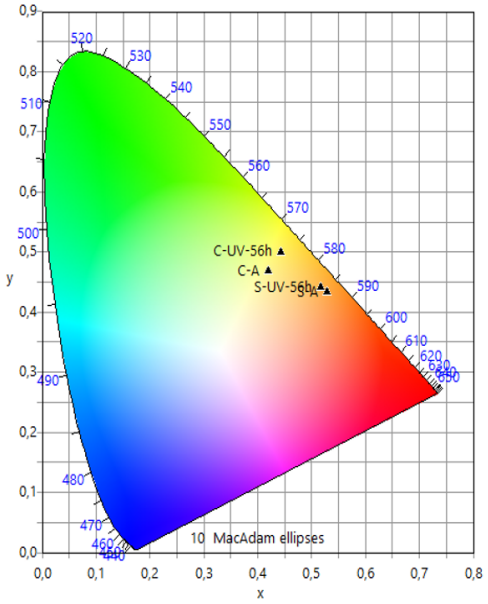

(b)

Figure 37: (a) CIE coordinate trend for C-A and S-A samples exposed to UV radiation. The ΔE for the yellow sample shows exponential growth; (b) color changes

changed the previous ESA signal (figure 39b). In this case, the spectrum is composed mainly of a broad short-lived signal, having different peaks in the region between 475 and 580 nm. Before 475 nm, the same ESA observed for the C-A sample is observed, but with a duration of only 5 ps. The broad short-lived signal after 20ps converted into a negative signal, probably stimulated emission (SE). Around 750 nm, we have another positive signal with the same duration (about 20

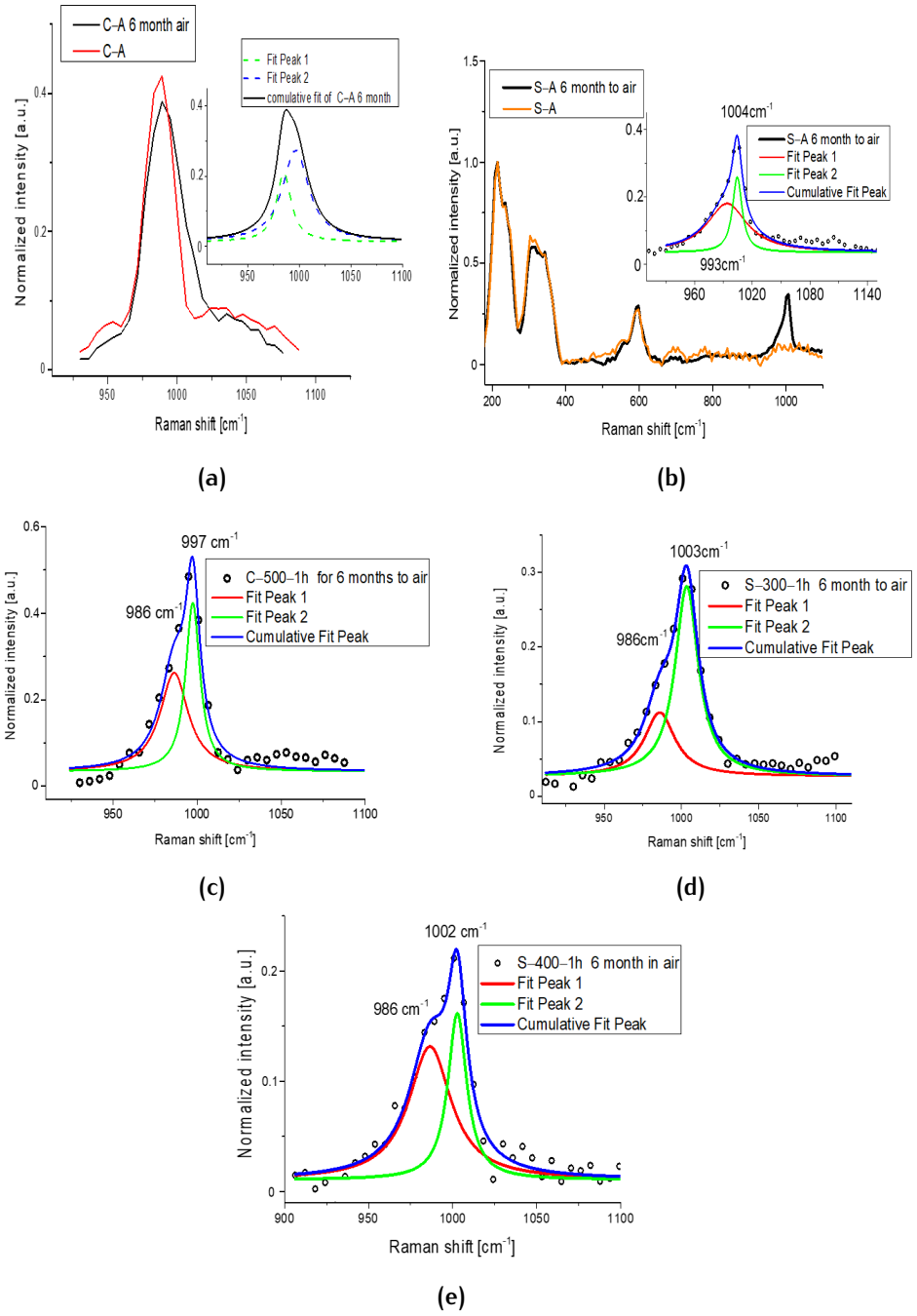

Figure 38: (a) Raman spectrum of C-A sample exposed to 6 months in air in a range between 900 and 1110 cm^{-1}; in inset, the band deconvolutions; (b) Raman spectra of S-A sample and S-A after 6 months in air; in inset, the deconvolutions of the R.O.I (sulphate region) for the sample exposed to air; (c) deconvolutions of the R.O.I for the C-500-1h sample exposed to 6 months to air; (d) deconvolutions of the R.O.I for the S-300-1h sample exposed for 6 months to air; (e) deconvolutions of the R.O.I for the S-400-1h sample exposed for 6 months to air.

ps) but with a longer rise time. The ground state depletion (GSD) signal in the near infrared is located only in the region 775-815 nm

and with a very short time of about 5 ps. The disappearing of the broad trap state band (negative signal between 600 and 750) after the thermal treatment agrees with the TR-PL measurements in the micro-second scale mentioned before (Figure 32c).

The UV exposure led a further broadening of the ESA signals (Fig-

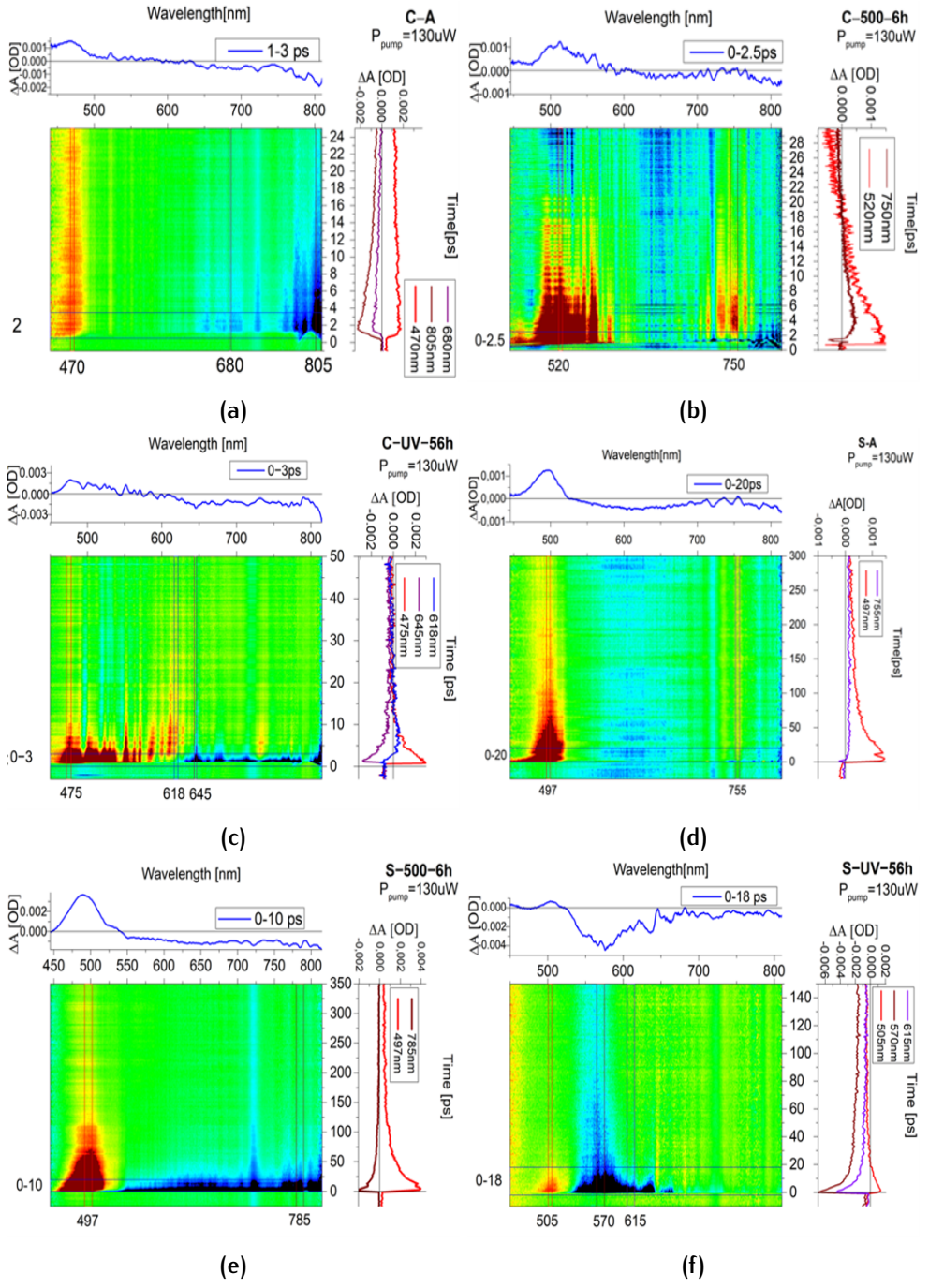

Figure 39: Transient absorption map of (a) C-A sample, (b) C-500-6h sample, (c) C-UV-56h sample, (d) S-A sample, (e) S-500-6h sample, and (f) S-UV-56h sample.

ure 39c) with respect to the C-A sample up to 630 nm, after which a broad short-lived negative signal started from 640 nm. Additional

positive bands start a few picoseconds after the pump absorption, suggesting a non-radiative relaxation to a lower level, from which starts the probe absorption.
Concerning the orange sample, the no-treated powder is composed of a long-lived ESA signal centered at around 495 nm. No negative signals were detected for this sample (Figure 39d).
The heated sample (Figure 39e) showed the same ESA signal and, in addition, a new very broad long-lived negative signal in a region between 550 nm and 815 nm (2.25eV–1.52 eV) attributed to a GSD. This result is compatible with TR-PL measurements where the new trap states around 750–820 nm were obtained after the heating relax after microseconds (Figure 32d).

The UV-exposed sample showed variations in the kinetics of ESA signal, which became shorter (duration of about 40 ps) and the formation of a new broad negative signal centered at 570 nm. The latter can be broken up into two regions with different kinetics, as can be clearly seen from Figure 39f, associable to a long-lived GSD signal at 570 nm and short-lived GSD at 650 nm, both towards trap states. To produce a first interpretation of these results, we can hypothesize that the negative signal in the NIR around 780 nm, found in both normal and UV-exposed samples, could be linked to Cd vacancies, as confirmed by SEM-EDS calculation and by previous authors [145]. Furthermore, the substantial difference in UV exposure for the C-sample resides in the broadening of absorption signals, attributable to a change inside the conduction band structure, new levels due to the formation of defects, and changes in electronic transfer, as suggested by different kinetics observed in some positive signals. The thermal treatment and UV exposure, mainly for orange samples but even, to a lesser degree, in white yellow, led the formation of new trap states inside the bandgap, defects responsible for the darkening effect in aged samples.

Binder degradation

The next step was to analyze the degradation of linseed oil (most used by impressionists) to discriminate which degradation process could be the most efficient for the complex mock-up of oil on canvas. As previously reported in the literature, the light exposure on linseed oil implies changes in its Raman spectrum. In details, in the region between 700-1800 cm^{-1}, it is known the decreasing of the 1264 (CH=CH rocking), 1022, 971 (CH=CH wagging), and 912cm^{-1} bands, and the disappearance of the 940 cm^{-1} (ω(CH) in CH=CH wagging) peak [146]. We performed a detailed analysis of this process by ageing the oil with the exposure of Hg lamp and deuterium lamp.

The results are reported in figure 40a and 40b. In our Hg-aged linseed oil, the Raman spectrum (figure 40a) showed an amorphization of the 866 cm^{-1} band (it becomes broader), a notable decrease of 940,

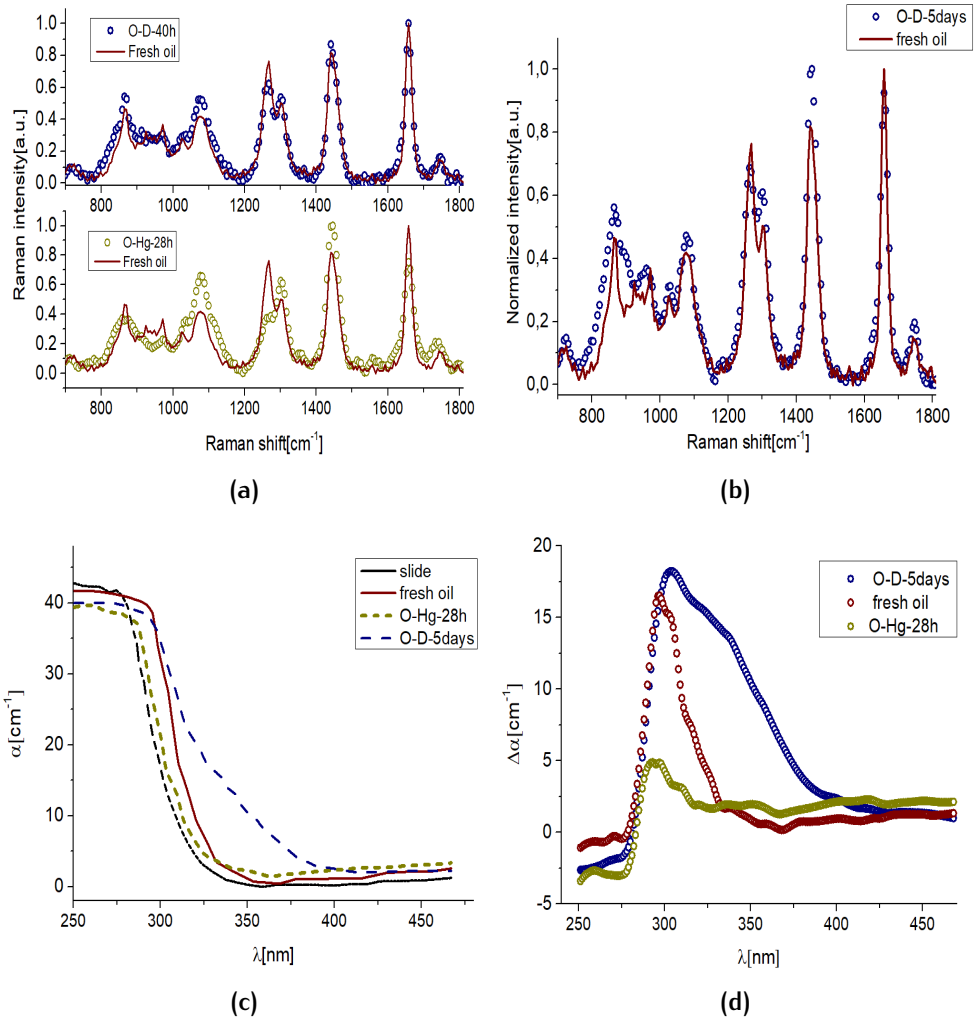

Figure 40: (a) Raman spectra of raw and irradiated oil samples after 28 h of Hg lamp and 40 h of deuterium lamp; (b) Raman spectra of raw and irradiated oil samples after 5 days of exposure to UVC lamp; (c) absorbance spectra of the different degradation process of linseed oil; (d) the differential absorption $\Delta\alpha$ using slide as reference.

1264, 1655 (C=C isolated cis) bands, and the increase of the 1081, 1022, 1302, 1439 (δCH_2) and 1655cm^{-1} bands.

The 1743 cm^{-1} (C=O) band showed a soft increase of its intensity and a slight shift towards lower cm^{-1}. An evident inversion of intensity between the 1264 and 1302cm^{-1} bands is observed. The action of a 365 nm source produced a remarkable alteration of the 1264 cm^{-1} band associated with CH=CH cis rocking, but the color of the sample did not show the yellowing process previously reported.

After 28h of 60mW/cm^2 of Hg lamp exposure, no chromatic changes for the oil were found. The absorbance spectrum is indeed like the fresh oil one, except for the formation of a very broad and low band around 450 nm (fig 40c). The exposure to after UVC irradiation, on the contrary, leaded to a yellowish process even after 24h, the pro-

cess becoming more remarkable after 5 days, as demonstrated by the new intense shoulder around 340 nm in the absorption spectrum (see figure 40c and 40d). Also in this case, the Raman spectrum showed traces of degradation similar to what seen for Hg lamp exposure, but in this case, the 1264cm^{-1} peak was not altered and the change of the 866cm^{-1} peak (ascribed to amorphization) shows an increase of intensity and broadening to high wavenumber side of the band.
The 1435, 1302, 1747 cm^{-1} bands become higher, while the 1265 and 1657 cm^{-1} peaks decreased and a new shoulder around 900 cm^{-1} was observed.

Since UVC exposure produced irradiation effects (yellowing) on the oil whilst 365 nm did not causes any change in color, to understand the total process of the Cd-paint degradation we investigated the UVC irradiation on the complex mock-up (oil with canvas and pigments).

Pigments on canvas degradation

We prepared and analyzed the complex mock-ups made of the only linseed oil spread on canvas and both pigments plus linseed oil spread on the canvas. The large chromatic changes induced in the first mock-up sample are reported in Table 8, whilst a summary for all the mock-ups is proposed in figure 41a where a CIE diagram shows the significative colour variation. After 5-7 days of deuterium lamp irradiation the oil deposited on the canvas showed a visible yellowish, the degradation increasing by increasing the days of exposure. The trend is confirmed by naked-eye inspection of the sample (figure 41b) and by reflectance spectra (figure 41c).

NIR-Raman spectra of these mock-ups were collected after 5 days of UVC lamp exposure in order to identify structural modification caused by the exposure. The degradation of the mock-ups is visible in figure 41d: the canvas and the oil (as described before) showed alteration in the intensity of some bands, but no additive compound was detected.

In addition, after a further 16 days air exposure, Raman spectra on the same mock-ups did not evidence any degradation related to the

Oil on canvas	L	a	b	ΔL	Δa	Δb	ΔE	Colour
0 days	74	-3.55	1.11	-	-	-	-	
2 days	73	-4.17	1.01	-1.00	-0.62	-0.10	1.18	
7 days	76,5	-5.6	7.93	2.50	-2.05	6,82	7.55	
12 days	70	-5.35	11.4	-4.00	-1.80	10.29	11.19	
16 days	76	-6.07	13.8	2.00	-2.52	12.69	13.09	
20 days	72.3	-6.39	16.7	-1.70	-2.84	15.59	15.94	

Table 8: Chromatic coordinates of oil on canvas exposed to different UVC time exposure.

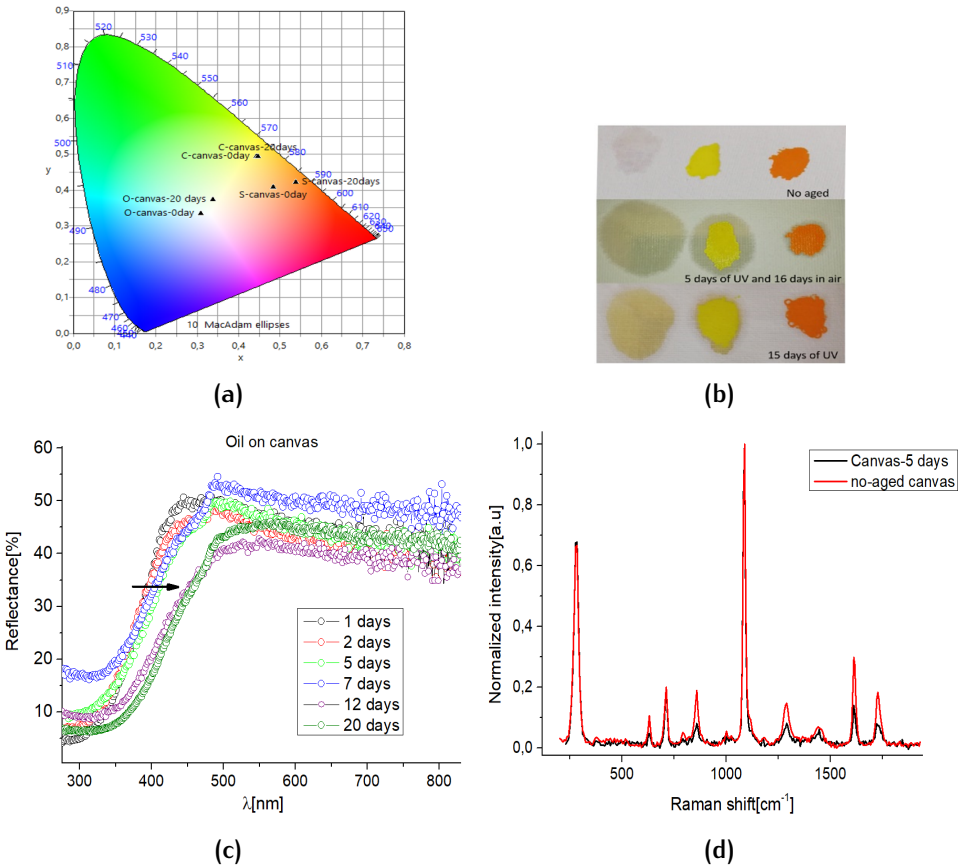

Figure 41: (a) CIE coordinates of the mock-ups before and after the UVC exposure; (b) picture of these mock-ups; (c) reflectance spectra of the oil at different days of UVC-exposure; (d) Raman spectra of raw and irradiated canvas.

formation of sulfates in both pigments (fig 42a and 42b). We then performed a longer UVC irradiation (15 days) and collected the Raman spectra (not reported for sake of clarity). Even in these samples no additive sulfate compounds were detected. The Raman analyses were repeated even after 6 months of exposure to air, still no degradation products were present on the surface. The reported results seem to suggest that the oil acts as a protective film avoiding the direct contact of the pigment with the atmosphere and with the light, generating a slowdown in the degradation of the pigment.

Indeed, up to 5 days of irradiation of the binder no degradation is observed and only for larger exposure the binder itself turned into pale yellow, showing differences in the vibrational spectrum as compared to the raw binder, as discussed before. The UV light also affected the canvas, in fact its Raman spectrum presented variations in peaks intensities as compared to the no-degraded sample. However, in this short period, no compositional change of the inorganic pigments spread on the canvas was detected, although the reflectance spectra registered a small blue-shift trend in the C-samples (figure

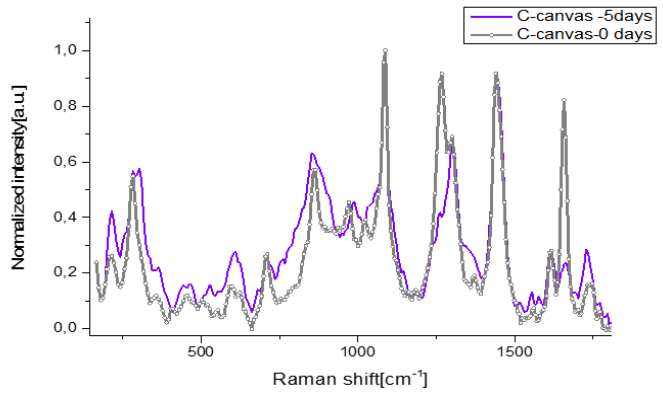

(a)

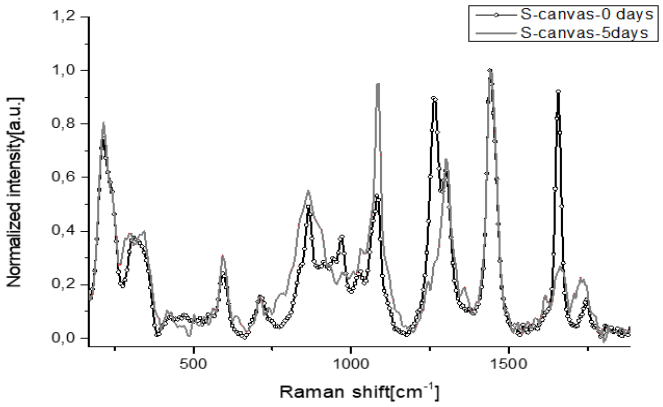

(b)

Figure 42: (a) Raman spectra of yellow pigment spread on the canvas at 0 and 5 days of exposure; (b) Raman spectra of orange pigment spread on the canvas at 0 and 5 days of exposure.

43a) and a small red shift in the S-samples (figure 43b), better evidenced by the corresponding first derivative spectra reported in the insets.

To summarize the overall color variation caused by the UV exposure in each step, we compared all the variation of the CIE coordinates and the total difference ΔE in table 9. The weight of oil-canvas degradation is predominant since the total variation ΔE assumes the value of 15.9. Single pigments present a maximum variation ΔE for sample C which takes on the value of 6.2 after only 56h of UV exposure. In this regard, the results allow us to confirm the provisional protective role of oil for sample C, which reacts with the environment in a reduced way, concluding with a total variation ΔE of only 3.5 after 20 days. We can assume that, after this primary protective action, a progressive degradation of the oil leads to its vulnerability to the environment as suggested by the literature. However, the same feature cannot be confirmed in sample S where the mixture of oil with

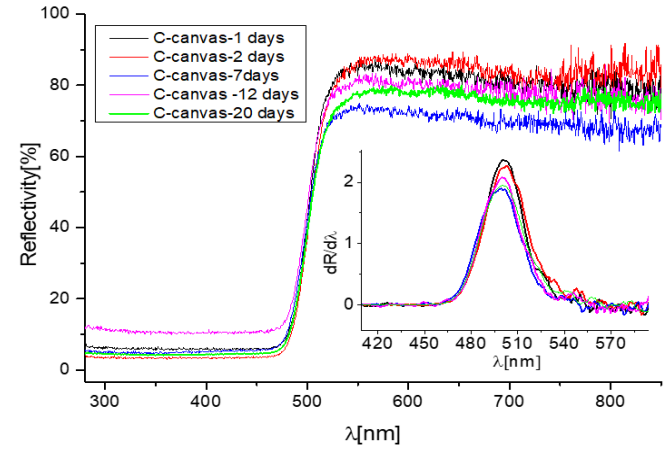

(a)

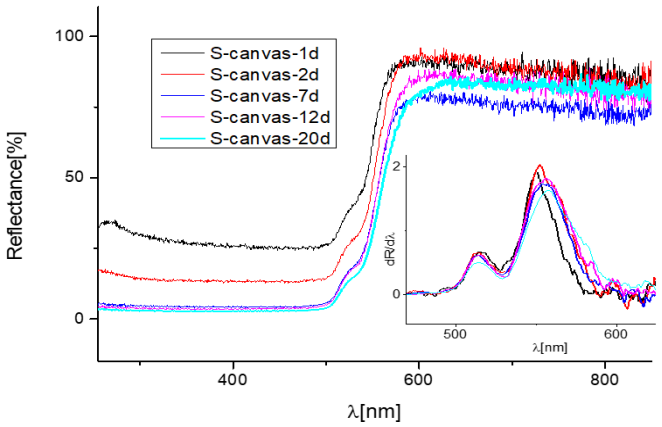

(b)

Figure 43: Reflectance spectra of irradiated C-sample (a) and S-sample on canvas.

pigments brings about the opposite effect: a variation of 27.2 with respect to 2.4 of the sole S pigment mainly due to oil yellowing.

Sample	ΔL	Δa	Δb	ΔE
C-UV-56h	5.9	-2.21	2	6.2
S-UV-56h	1.6	-1	1.4	2.4
Oil-canvas-20d	-1.7	-2.84	15.59	15.9
C-canvas-20d	-3.1	1.71	-0.2	3.5
S-canvas-20d	-5.5	8.8	25.1	27.2

Table 9: Color differences between the aged and no-aged samples.

2.2.5 Synopsis of the obtained results

Light-yellow and orange pigments from Kremer were artificially degraded through different accelerated ageing: heat treatment and UV light exposure. Whereas the orange pigment seems more stable, the yellow one degrades more markedly.

Reflectance spectra and chromatic coordinates in the CIELab space revealed that the heating treatment, executed in a range of 100–500°C until 6h, causes a prominent color variation for the light-yellow pigment in terms of bleaching. XRD and Raman spectroscopy suggest that the cause is attributable to the formation of sulfate compounds and possible cadmium oxide, detected in the XRD pattern of the sample heated at 500°C for 6h, after the reaction with the oxygen present in the environment atmosphere. This interpretation is also confirmed by the punctual SEM/EDS analysis. The formation of deep trap states and oxide products after thermal treatment was also confirmed by TRPL measurement, performed in the ps and micro-second scale. The same conclusion for the formation of whitish compounds can be adopted for UV treatment, which allows one to demonstrate, by means of Raman spectroscopy and SEM-EDX, the formation of a superficial sulfate phase. In addition, the action of UV light for the yellow sample, and both UV and thermal exposure for the orange one, seems to produce a defective phase where intra-gap energy levels are generated.

Actually, with the help of pump–probe measurements, GSD and long ESA signals due to the formation of trap levels are evidenced in the visible and near-infrared region, both for light-yellow and orange pigments. If structural defectivities are activated by light exposure, the reaction with atmosphere seems to also produce darker compounds, such as cadmium oxide, and whitish compounds, such as cadmium sulfate, as previously reported in the literature.
In addition, the investigation was extended on the study of the interaction between UV light and the binder or canvas support, taken singularly, or combined with the pigments. The color variation was even revealed in linseed oil and canvas with no pigments exposed to UV light, while the formation of sulfate phase in the combined systems is not observed. This condition suggests a complex color change due to the single variation of canvas, oil, and pigments.

Finally, it may be assumed that a visible color variation of CdS pigment, caused by natural factors like time, light, and atmosphere, is determined by three factors: 1) oil degradation which translates into a darkening and yellowing process that is more remarkable in the S-sample; 2) after temporary protection, degraded oil does not act in the same way on the pigment that, exposed to the environment atmosphere, reacts with the oxygen forming sulfate (bleaching) or/and oxide compounds. The third factor, the degradation of the canvas itself, contributes to the yellowing as a minor factor.

3 STRATIGRAPHY OF ANCIENT FRESCOES: A NEW APPROACH WITH PHOTOACOUSTIC AND SORS IMAGING

Photoacoustic (PA) imaging is a novel, powerful diagnostic technique utilized in different research fields. In particular, during the last years it has found several applications in Cultural Heritage (CH) diagnostics. PA imaging can be realized in transmittance or epi-illumination (reflectance) mode obtaining variable levels of contrast and spatial resolution. The first detection geometry can be used only on thin objects including paintings, and multi-layered documents, revealing hidden layers, and measuring the thickness of very thin optically turbid paint layers.
The second acquisition geometry has recently shown its potential in providing diagnostic information in artistic mock-ups of different thickness.

The aim of this chapter is to test for the first time the potential of the PA imaging technique to reconstruct stratigraphic profiles of thin and thick frescoes surfaces, one of the most challenging artwork objects, moving from real fragments to mock-ups, exploring also the limits and the advantages of this diagnostic method in this challenging application.

Furthermore, we attempt to combine PA imaging with Spatially Offset Raman spectroscopy (SORS) technique, obtaining complementary information. SORS is another technique recently applied for stratigraphy in multi-layered samples, and is based on laser defocusing to receive information from the underlying layers.
Despite the fact that the principles of SORS are entirely different from the PA techniques, they can potentially employ the same excitation source, offering the possibility to be integrated together into a single hybrid instrument for obtaining stratigraphic characterization of a sample. In this direction, we have experimentally demonstrated that the apparent information complementary between PA and SORS diagnostic methods can be carried out in a realistic case of multi-layered fresco samples. The combined use of these two techniques has been proven useful to achieve detailed hidden information on the investigated fresco samples.

3.1 PHOTOACOUSTIC TECHNIQUE

Photoacoustic imaging has several applications in different science branches, ranging from biomedical to Cultural Heritage (CH) fields [147–156], due to its capability to provide in-depth optical absorption contrast with high spatial resolution.
In the field of conservation and artwork diagnostics, it has recently found several applications such as revealing hidden underdrawing on paintings [157–160], discovering degradation and retouching features in historical oil paintings [152], uncovering text in multilayered documents [161], and monitoring laser cleaning interventions on stonework [162, 163].
The photoacoustic (PA) imaging is based on the absorption of a pulsed laser beam by a turbid material, with consequent thermal expansion and production of an initial local pressure rise (p_0) proportional to the local laser optical fluence F, the dimensionless Grüneisen parameter Γ, the percentage of pulse energy converted into heat η_{th} and the optical absorption coefficient for the employed wavelength [164, 165], which is mathematically expressed by the following relation:

$$p_0 = \Gamma \mu_\lambda \eta_{th} F \tag{21}$$

The initial local pressure propagates in the form of ultrasonic waves prior its detection by an ultrasonic transducer (air-coupled or immersion), located in-behind the sample in transmission geometry, or on the same side with the laser beam in epi-luminescence (reflectance) geometry. The generated acoustic wave is typically found in the MHz frequency regime, with the detected amplitude directly proportional to the local absorption coefficient of the medium for the employed excitation wavelength [166], providing, in this manner, excellent optical absorption contrast with high sensitivity.
The recorded acoustic wave can propagate in the materials and encounter low attenuation, about up to three orders of magnitude less than near-infrared optical radiation [149], permitting to receive information from deep layers located a few hundreds of μm or even a few mm below the sample's surface.
Recent work [153] demonstrated the potential of the new epi-illuminescence geometry photoacoustic system for obtaining information of hidden graphite layers found in various wall painting mock-ups. In this work, we extend further the capabilities of this new apparatus as regards the accurate reconstruction of the transverse profiles of real ancient fresco fragments, realized with the overlap of many pictorial layers, estimating the thickness values of the successive layers.

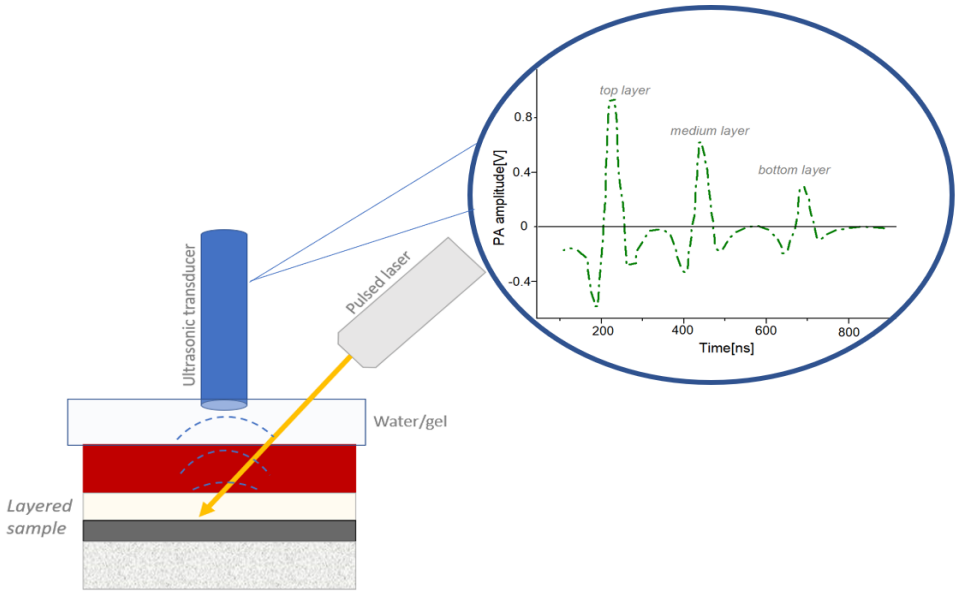

Figure 44: Schematic representation of PA geometry.

3.2 SORS TECHINQUE

The SORS (Spatially Offset Raman Spectroscopy) is a technique for overcoming the turbidity of the sample, which makes even radiation with great depth of penetration such as in the IR impenetrable at certain depths.
There are three different variants of the SORS: defocusing micro-SORS, full micro-SORS, and fiber optic micro-SORS. For the fresco sample (highly turbid media) we reached a good compromise between sensitivity and spatial resolution by applying the first one.
The defocusing micro-SORS is based on defocusing the microscope's objective on the sample to obtain information on the underlying layers. The zero position of defocusing is defined as the position in which the sample is in focus and its Raman spectrum is mainly characterized by its surface signal [167–169]. By defocusing, i.e. increasing the space between the objective and sample of a Δz, new Raman spectra are obtained gradually characterized by the contribution of the sub-surface layers. One can highlight these contributions by subtracting the surface signal at zero position, achieving non-destructive depth-resolved chemical and structural analysis of the CH objects by Raman spectroscopy.
In general, a spectrum dominated by the signal from the only surface is obtained by using a sub-millimeter pinhole, which allows the contribution of the inner layers to be masked. After careful subtraction of the surface signal, it is possible to follow the intensity trend of a particular compound as a function of the defocusing distance, resulting in non-invasive stratigraphic profiles of the multi-layered sample [170, 171].

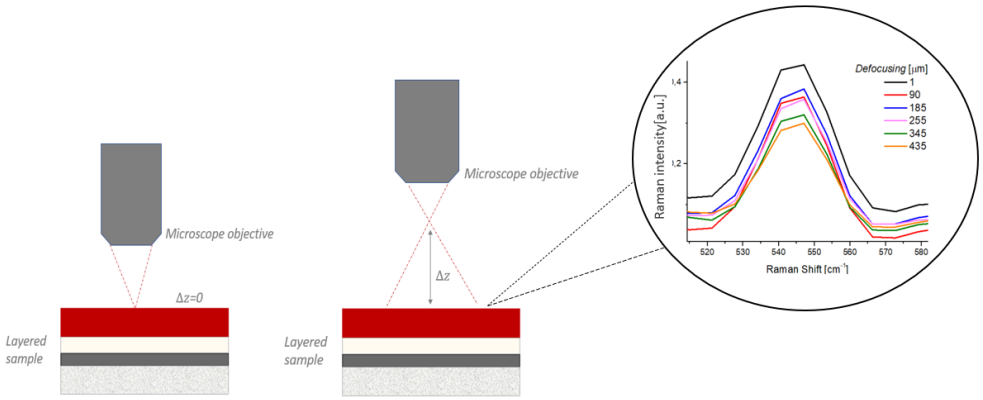

Figure 45: Schematic representation of micro-SORS geometry set-up.

3.3 MATERIALS AND METHODS

Analytical methodology

To determine the stratigraphy of frescoes, real samples and mock-ups with different pigments and with variable thickness were analyzed using Photoacoustic and SORS techniques. The estimation of their thicknesses was carried out by observing their cross sections under electron and optical microscopes. The Photoacustic and the SORS are used with the same exciting wavelength in the NIR.

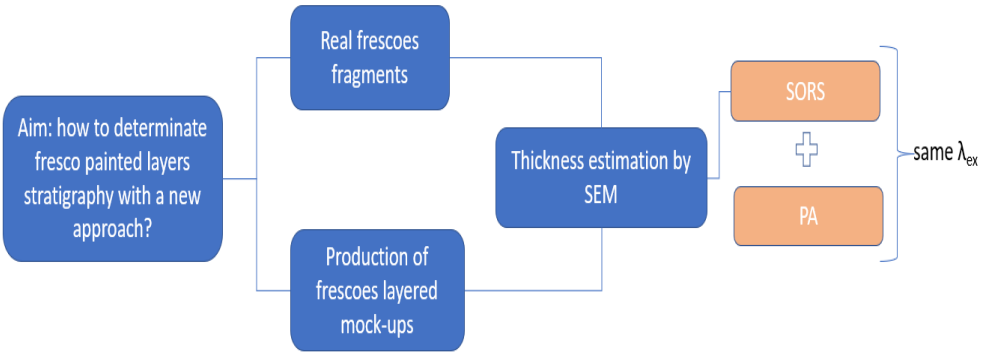

Figure 46: Schematic representation of the methodology followed for the stratigraphy reconstruction of frescoes.

3.3.1 PA experimental set-up

The imaging apparatus employed a Q-switched Nd:YAG laser (SL404, Spectron Laser Systems, Rugby, UK; maximum pulse energy 30 mJ, pulse duration: 10 ns, pulse repetition rate: 10 Hz) emitting infrared radiation at 1064 nm. The beam was initially attenuated and reduced in diameter to 1.2 mm using an adjustable iris diaphragm so that the pulse energy on the sample's plane is less than 0.90 mJ. A positive

lens with a focal distance equal to 50 cm was used to focus loosely (spot size: ca. 1 mm) the optical radiation, improving the sensitivity of the imaging system. Each sample was placed at the bottom of a 3D-printed sample holder filled with distilled water, which served as an immersion medium for the efficient propagation and subsequent detection of PA signals. The sample's front surface was irradiated to generate laser-induced ultrasound from the highly absorbing layers. The generated PA waves were transmitted through the painted layers and water prior to their detection in reflectance configuration by a broadband, spherically focused piezoelectric transducer (HFM28, SONAXIS, Besancon, France; nominal central frequency 73 MHz; focal distance: 4.53 mm; numerical aperture 0.44). The signals were subsequently enhanced by two low-noise radio frequency (RF) amplifiers (TB-414-8A+, Mini-Circuits, Camberley, UK; gain: 31 dB) connected in series to achieve a total gain of 62 dB, which was adequate for the digitization and recording of PA waveforms by an oscilloscope (DSO7034A, Agilent Technologies, Santa Clara, CA,USA; bandwidth: 350 MHz; sample rate: 2 GSa/s). To form an image, the sample was raster scanned with high-precision XY motorized stages (8MTF-75LS05, Standa, Vilinius, Lithuania), to attain a point-by-point data acquisition synchronized with the trigger signal of the laser source. The recorded waveforms were averaged two times for signal-to-noise ratio (SNR) improvement, transferred to a computer, and band passed between 100 kHz and 30 MHz for high-frequency noise elimination. The modulus of the Hilbert-transformed PA waveforms was estimated for the reconstruction of the imaged layers in 3D. Depending on the size of the underlying sketch area, the scanning regions had dimensions ranging between 2x2 to 4.5x4.5 cm^2 respectively, and were sampled, in all cases, using a pixel size of 300x300μm^2. The total time required for the recording of a PA image ranged from 2.5 to 4 h. Control and synchronization of the PA imaging system were accomplished using custom-developed software, whereas image processing was performed through ImageJ and MATLAB programming environment.

3.3.2 SORS measurements

Measurements were performed in ambient air at room temperature with a compact spectrometer BWTEK (Newark-USA) i-Raman Ex integrated system with a spectral resolution of $8cm^{-1}$. For each experimental setup, all the spectra were collected with an acquisition time of about 60 s (five replicas) and power excitation between 5 and 15 mW concentrated in a spot of 0.3 mm^2 on the surface through a Raman Video MicroSampling System (Nikon Eclipse for high-resolution and BAC151B in the other case) equipped with a 20 Olympus objective to select the area on the samples. Each measurement area represents a

sampling surface of about $1cm^2$.
Micro-SORS measurements were carried out with the above Raman system by collecting the spectra in different sample positions.
The SORS measurement is obtained by acquiring the spectrum of the surface and then operating a progressive defocusing to provide the contribution of sub-layers. With the help of a sub-millimeter pinhole (diameter of 500 µm), the contribution of the upper surface (zero point) is isolated with respect to the sublayers. Then, after removing the aperture, spectral acquisition was perfomed at fixed defocusing distances (10, 20 and 30 µm steps) from the zero position. Zero position spectrum and defocused spectra were finally subtracted to extract the Raman contribution at a specific defocusing distance.

3.3.3 Samples

Real fresco samples

The 3 fresco fragments (called respectively F.01, F.02 and F.03) belong to a fresco of San Giuseppe Church in Cagliari (ca. 1870 AD.) which has been unintentionally detached from the vault because of aging. All the samples appear to constitute by different layers of plaster and painted on their top surface using different pigments. A 1cm cross section along the depth direction was cut from one of the fragments to analyze the layer composition by surface Raman spectroscopy and scanning electron microscopy (SEM) imaging. Samples were analyzed at different points distributed on internal and external surfaces and they were not modified after recovery; the fragments were subjected to gentle dust cleaning with soft brushes. For facilitating the reader, Table 10 summarize all the samples with each point of analysis. F.01

Fresco fragments from San Giuseppe Church			
Sample	**Substratum**	**Painted line**	**N° of layers**
F.01	Concrete, calcium hydroxide	L1	3 layers
		L2	2 layers
		L3	2 layers
F.02	Concrete, calcium hydroxide	L4	1 layer
F.03	Concrete, calcium hydroxide	L5	3 layers (same composition of L1)
Fresco Mock-ups			
Sample	**Substratum**	**Painted line**	**N°of layers**
M.02	Lime, sand, calcium hydroxide	Total area	1 layer: lapislazuli
M.07	Lime, sand, calcium hydroxide	Total area	1 layer: cadmium orange (CdSeS)
V.02	Compact earthenware	Area 1	3 layers: graphite, cadmium yellow (CdS) and ochre
		Area 2	2 layers: graphite, cadmium yellow
		Area 3	1 layer: graphite
V.03	Compact earthenware	Area 1	2 layers: ochre and cadmium yellow
		Area 2	2 layers: ochre and cadmium orange

Table 10: Real fresco samples and mock-ups.

is composed of L1, L2, and L3 painted lines having different stratigraphy: L1 is dark in the top, L2 is white and L3 brownish-grey. L1 is

composed on the whole by three layers including the dark one, while L2 and L3 present two layers considering the visible one on the surface. Sample F.02 is composed of only one layer called L4. In sample F.03 the only line analyzed is the brownish labelled as L5, equal in composition and structure to the L3 line of F.01. All these samples and lines are shown in detail in Table 11.

Fresco mock-ups

To test the PA performances in stratigraphic imaging, and provide a comparative study with the results obtained with SORS profiles, additional fresco mock-ups were realized: M.02 and M.07 with lime, sand, and calcium hydroxide substrates (the typical composition of a fresco, the "arriccio" and "intonachino") covered by lapislazuli and cadmium orange (CdSeS) respectively.
In addition, other samples V.02 and V.03 were made with compact earthenware. These are composed of different layers: V.02 presents 3 layers, the bottom one made of graphite, the second by cadmium yellow (CdZnS), and then ochre. Sample V.03 is composed of a bottom layer made of ochre and two covering layers: one containing cadmium yellow and the other cadmium orange.
The different compositions of pigments used in mock-ups samples were selected to have a complete scenario about the absorption properties of PA source in order to verify the contrast feature of this technique in a multi-layered structure.

3.4 RESULTS

3.4.1 Frescoes from San Giuseppe Church

As the first step, SEM-EDX analysis was performed on different cross-sections of the samples (see figure 47 and table 11) to confirm the presence of different layers, and their chemical compositions. In the same table we propose also the cross-section imaging obtained with PA, and the relative PA later view images. A detailed analysis of these results will be leaded below in this paragraph. Cross sections confirmed the presence of several pictorial layers up to a maximum of three and a minimum of one, with variable thickness evaluated with different scales of magnification. The lime wall support (called intonaco) is not smoothed and homogeneous, making even the superficial brushstrokes inhomogeneous. The elemental compositions derived from EDX are listed in Table 12 for L4 line (F.02 sample), in which higher atomic percentages are relative to Ca, Si, C, and O, a typical composition of a mortar and amount of Fe, Ca, S are due to

Sample	a	b	c	d
F.01	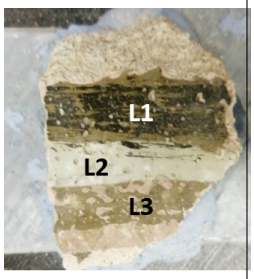	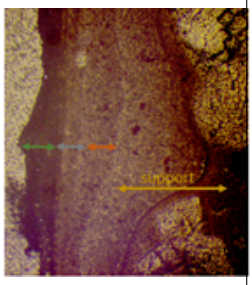	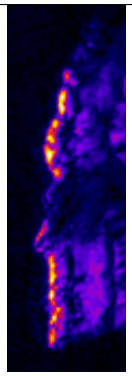	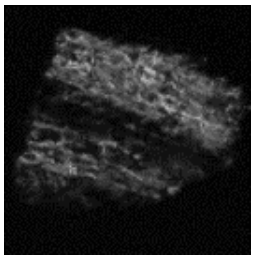
F.02	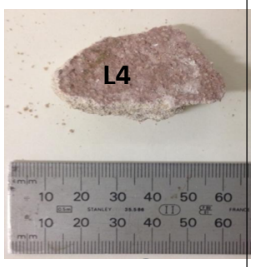	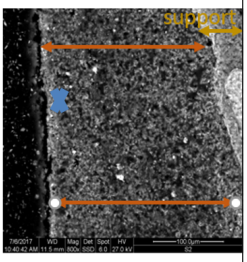	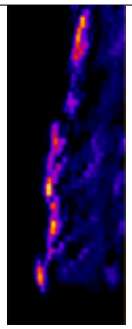	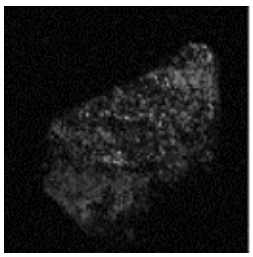
F.03	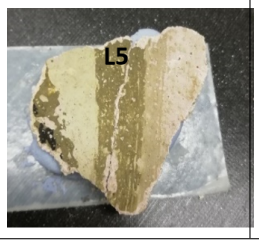	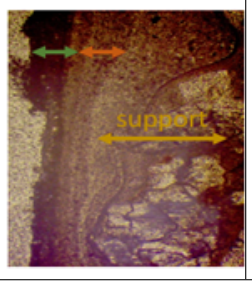	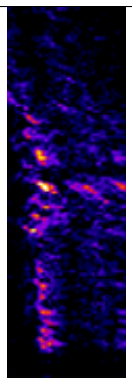	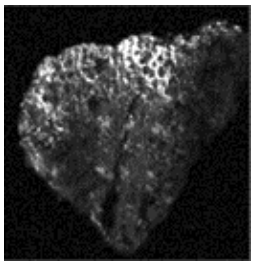

Table 11: Moving from the right, we have: a) the picture of fresco fragments; b) the cross-section images; c) cross-section imaging obtained with PA; d) and relative PA later view images.

the pigments of the painted layer. Their distribution in sample F.02 is shown in Figure 47.

Additional NIR-Raman measurements were also carried out on fresco samples in order to individuate the chemical phases of the elemental analysis conducted by SEM-EDX. Raman spectra of L1 and L4 painted lines are shown in Fig. 48. In detail, the 3 layers of L1 line present the following characteristics: the upper one is black, composed of amorphous carbon black (graphite) recognizable by the two characteristic Raman bands at 1325 cm^{-1} and 1580 cm^{-1} mixed with calcite having a strong peak at 1081 cm^{-1} (CO_3 symmetric stretching [172]); the intermediate layer with a visible brownish/greyish color is composed of a mixture of calcite, graphite, hematite (characteristic

Element	Line Type	Intensity	Weight %	Weight % err	Atom %	Atom % err	Compound %
C	K	103.87	22.37	0.37	35.78	0.59	22.37
O	K	69.78	33.26	0.43	39.93	0.52	33.26
Na	K	4.69	0.58	0.04	0.48	0.03	0.58
Al	K	24.26	1.93	0.05	1.37	0.03	1.93
Si	K	143.47	11.10	0.10	7.59	0.07	11.10
S	K	17.28	1.31	0.04	0.79	0.02	1.31
Cl	K	7.41	0.67	0.03	0.36	0.02	0.67
K	K	15.24	1.54	0.05	0.75	0.02	1.54
Ca	K	225.58	26.40	0.20	12.65	0.09	26.40
Fe	K	2.93	0.84	0.07	0.29	0.03	0.84

Table 12: SEM-EDX analysis on L4 line of F.02 sample, in the point indicated by a blue cross in Table 11.

peaks at 286, 410, 614 cm^{-1} due to Fe-O symmetric stretching [173]), and gypsum with the strong band at 1006 cm^{-1} related to $-SO_4$ symmetric stretching [174]. The last one is a mixture of hematite, calcite, calcium hydroxide (large band at 780 cm^{-1} [175]), and gypsum. Line L4 of F.02 sample is composed of a single pink layer with the same composition of the just mentioned layer of L1. Also in this case, the pink hue is obtained by a mixture of hematite, calcite, calcium hydroxide, and gypsum (in anhydrous and hydrate phases).

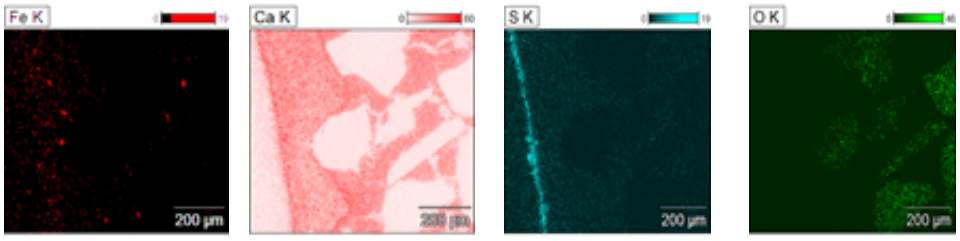

(a) (b) (c) (d)

Figure 47: Elemental distribution maps for the sample characterized by L4.

The thickness results of the relative layers obtained from the SEM and optical images are shown in Table 13. The high error values associated with these thicknesses are due to the inhomogeneity of the fresco surface: the brush strokes are applied on a non-uniform intonaco substrate. Thus, the thickness values listed in the table are derived from an average of different cross-sections at different points of measurement and the errors are calculated as their deviation standards.

After this preliminary characterization of real fresco fragments, we can concentrate our attention to the PA stratigraphic analyses. The experimental results derived from an average of 20 depth profiles of the three different samples obtained by ImageJ. To obtain the depth profiles we fitted the experimental data with Lorentzian and Gaussian functions as displayed in Figure 49. From stratigraphic

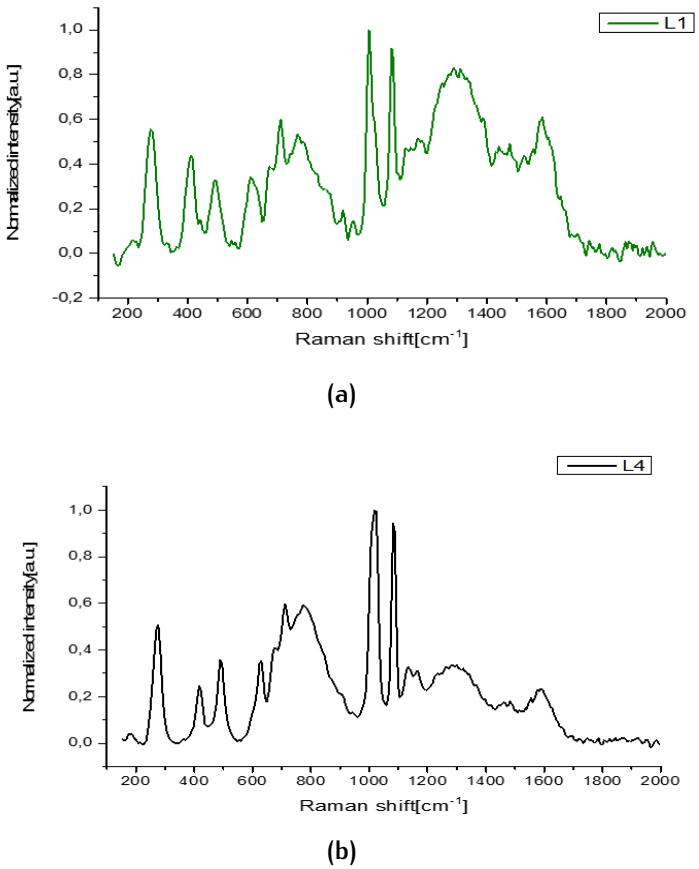

Figure 48: Raman spectra of different painted lines of fresco fragments.

images of Figure 49, in comparison with the Table 11 (images in column c), we excluded from our analysis the signal derived by thickness below 1 mm of depth, because they are probably spurious signals due to the reflection of PA waves in the substratum. This assumption is confirmed by a detailed study of mock-ups realized with different bases (see next paragraph). As revealed by the deconvolution procedure in Fig. 49(a), L1 painted line is composed of three layers with 60, 71, and 137 µm respectively with a maximum error of 25 %.

L3 is also made up of the overlap of two layers, as confirmed by cross-section images, with thicknesses assessed by PA techniques of 70 and 85µm. The L4 thickness, evaluated in the second fresco fragment (F.02 sample) confirm its composition of one layer. Due to the surface roughness of the sample, we estimated separately the maximum and the minimum thicknesses for this stratum, to decrease the associated absolute errors, obtaining $95\mu m \leqslant d \leqslant 170\mu m$. All the estimated PA values are consistent, inside the error bands, with the SEM measurements as shown in Table 13.

From the images of Table 11 (column d, the lateral view), some par-

SEM analysis		
L1[μm]	L3[μm]	L4 [μm]
$1^{st} = (81 \pm 30)$ $2^{nd} = (60 \pm 20)$ $3^{rd} = (80 \pm 30)$	$1^{st} = (81 \pm 30)$ $2^{nd} = (6o \pm 20)$	$1^{st} = (107 \pm 50)$
PA analysis		
L1[μm]	L3[μm]	L4[μm]
$1^{st} = (60 \pm 15)$ $2^{nd} = (71 \pm 20)$ $3^{rd} = (137 \pm 30)$	$1^{st} = (70 \pm 21)$ $2^{nd} = (85 \pm 20)$	$d_{max} = (170 \pm 40)$ $d_{min} = (95 \pm 15)$

Table 13: Thickness measurements of different layers of fresco samples by SEM and PA imaging.

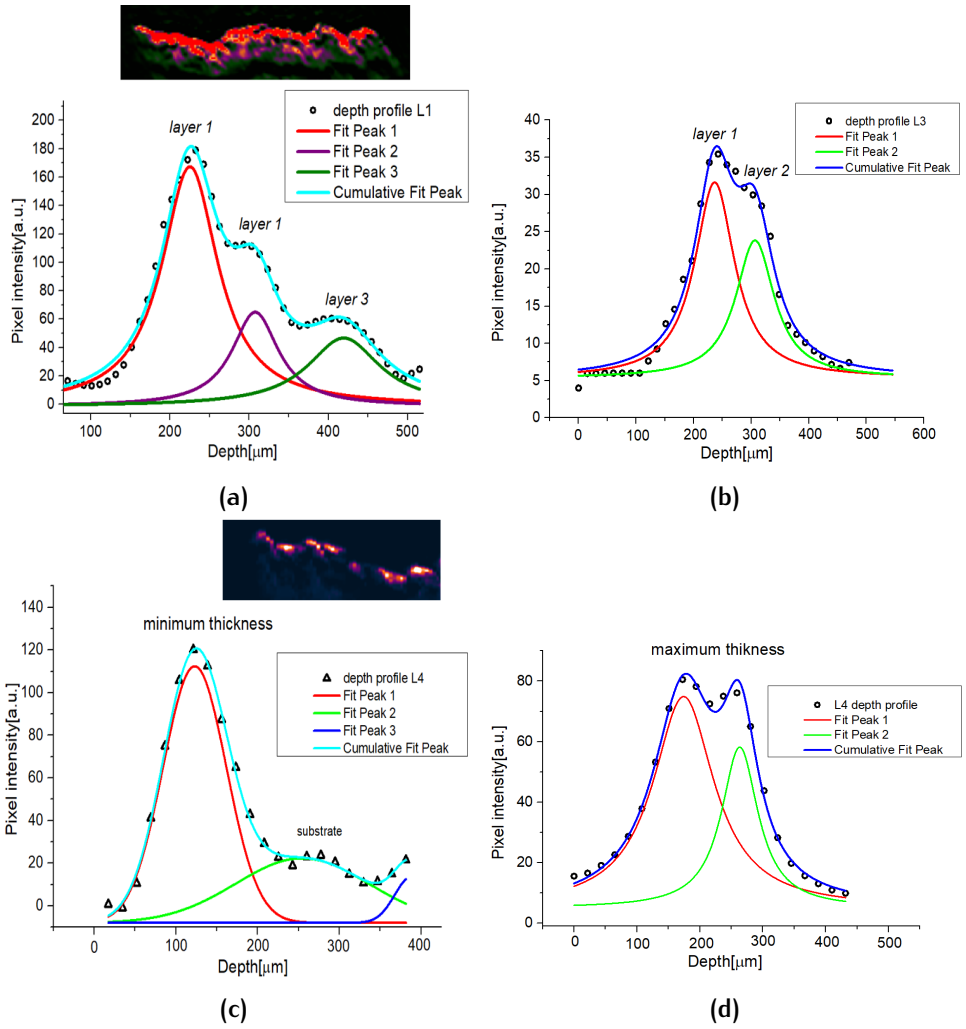

Figure 49: Stratigraphic profile fit obtained by PA imaging for the different painted lines: a) z-profile of L1; b) z-profile of L3; z-profile of L4 zone- maximum c) and minimum d) thickness evaluation.

ticular area, such as the L2 white line, presents a low PA signal that makes it difficult to define an accurate z-profile in that region. For this reason, in our preliminary study, we focused our attention exclusively on the darkest painted surface area providing high PA contrast. To have a complete characterization of sample F.01 and thus, a strati-

graphic analysis in the white area, we used the micro-SORS technique, recently applied for stratigraphy for CH objects.

For micro-SORS measurements, we employed the same excitation wavelength employed for PA imaging (1064 nm), to avoid fluorescence signals from the painted surface.
Also for micro-SORS technique, the investigation of frescoes samples represents a challenging task due to their inhomogeneous structure and the low-depth penetration in such turbid media, independently on the selected laser wavelength and focusing objective.
The results shown in figure 50 are obtained by an average of five different z-profile points, as done for PA signals.

Firstly, we analyzed the F.02 sample made with one layer to make

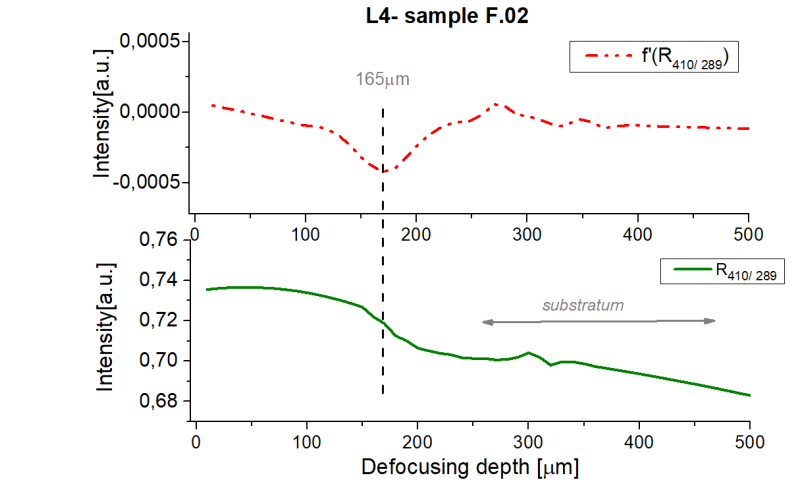

(a)

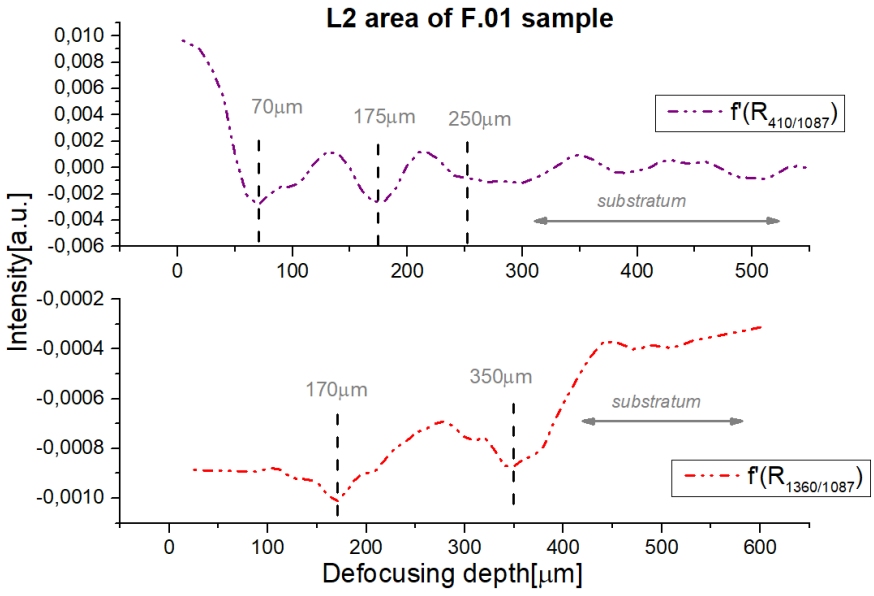

(b)

Figure 50: (a) Micro-SORS image of the sample F.02;(b) F.01 in the L2 zone (white).

a comparison with the PA analysis. The depth profile is obtained following the decrease of the 410 cm^{-1} peak intensity, associated with the red pigment (hematite), with respect to the intensity of the band at 1087 cm^{-1} (calcite deriving from the substratum layer). To better visualize the variation associated with the interface of a new stratum, we estimated the first derivative of the z-profile. The thickness obtained for L4 was found at $(165 \pm 30)\mu m$, in good agreement with the previous analysis.
Moving to the white layer of sample F.01, looking for the SORS profiles, we followed different ratio intensities associated with each component of this layer to better identify their stratigraphy. Fig. 50(b) offers the trends of hematite and graphite peaks at 410 cm^{-1} and 1360 cm^{-1} respectively, with respect to the principal band of calcite at 1087 cm^{-1}. For sake of brevity we reported only the first derivative of the analysis. From the hematite peaks, the obtained profile shows three layers at 70, 175, and 250 μm, with the thickness of about 70 μm, 100 μm, and 75 μm respectively.
For what concern the graphite profile, two layers are visible at 170 and 350 μm, but the simultaneous presence of this compound in two adjacent layers makes less accurate the identification of their profile. This specific problem is not so unusual in painted artworks. For this reason it is necessary reconstruct the stratigraphic information by combining the information from various profiles.

3.4.2 PA and SORS on Fresco Mock-ups: comparing limits and applicability

With the intent of validating the PA imaging methodology and exploring its limits or advantages on fresco samples, different frescoes mock-ups were realized. In Table 11(c) where the PA transversal view imaging are shown, three separate signals with the same trend but a decrease of the intensity are visible. This condition could be associated to spurious wave reflection phenomena in the fresco substratum with respect to the real signal of the painted surface (higher contrast in the image). In fact, in the fresco fragments, the substratum is composed of sand grains with variable sizes, which could produce spurious oscillation of the PA signal derived from the surface.
To verify this assumption, and exclude the two signals below the brighter one in our analyses of depth, we reproduce two different typologies of frescoes mock-ups: the first one made with the original substratum (sand, calcium hydroxide, calcite), similar to the real fresco fragments of Table 11, and the second one made with a homogeneous substratum of compact earthenware. Both the men-

tioned typologies were realized with different painting structures as reported before in Table 10 for samples M02, M07, V02 and V03.

The different PA profile images obtained from these mock-ups are

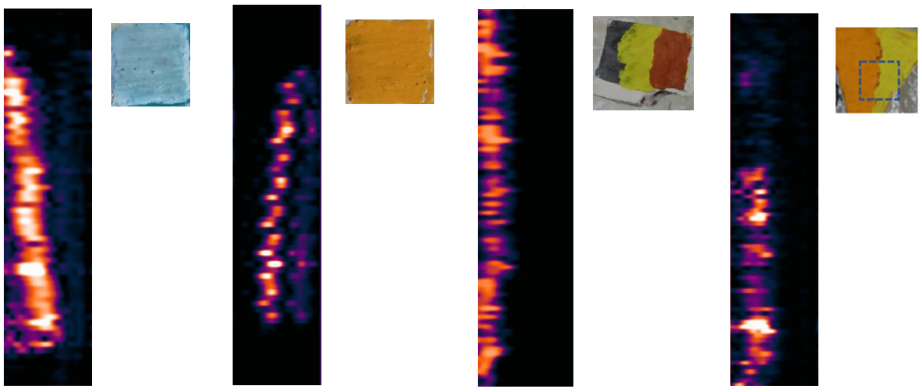

Figure 51: PA imaging of transverse view of a) M02; b) M07; c) V02 ; d) V03 samples with relative pictures.

shown in Fig. 51. In particular in figures 51a and 51b the samples made with an original fresco substrate (the "arriccio") presented another shade line below the sharp one in contrast with those obtained in V.02 and V.03 samples (see figures 51c and 51d). This finding confirms the hypothesis that the second signal is due to some artifacts of the PA waves originated by the presence of size variable substratum grains. The intensity of this spurious signal seems to be proportional to the absorbance and the thickness of the top layer. In order to avoid the contribution of these spurious signals and to present an analysis on multi-layered samples, we focused our attention only on the second group of samples, V.03 and V.02 (made from the succession of up to 3 layers), and we executed also a comparative analysis with SORS profiles.

Actually, by using these samples, we want to test the PA stratigraphic capability for thick-painted layers, obtained with pigments presenting higher or lower absorbance in the NIR region. These pigments are spread with larger thicknesses unlike the real sample analyzed above (<200 μm) to demonstrate the maximum depth that can be achieved using the PA signal. All PA measurements were compared with SORS results obtained in the same analyzed regions to provide complementary information about the stratigraphy.

Sample V.03 was made with two different cover layers, obtained with Cd-yellow and Cd-orange pigments. Below them, a red layer of ochre is present, and in the middle of the sample, some areas of this red layer were left visible.

The obtained PA transversal image is noisy, and the contrast is not very strong (Fig. 51(d) and Fig. 52), since the two colors chosen for the cover layer don't absorb enough in the NIR region, but it is still

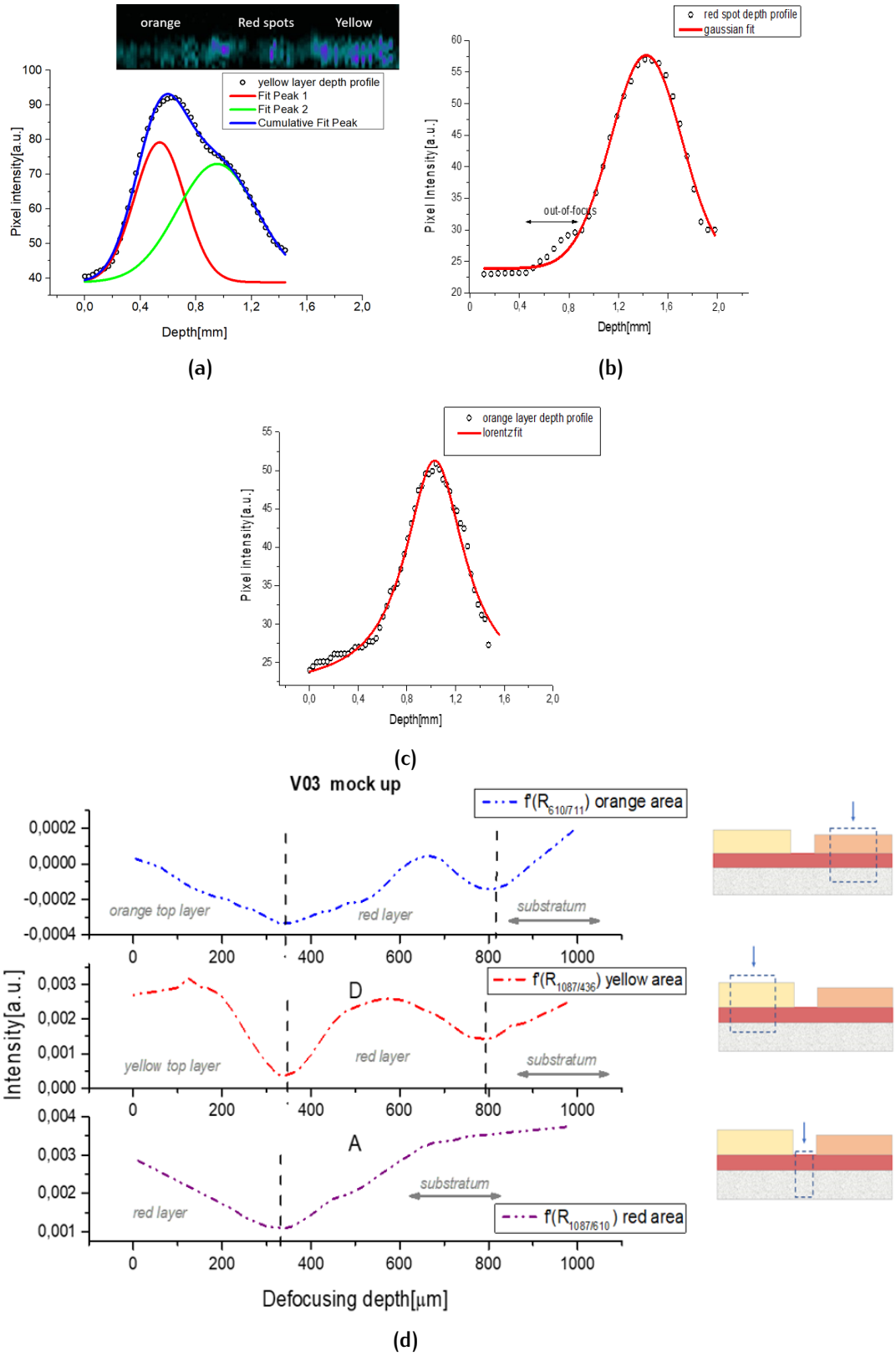

Figure 52: PA stratigrafic profile fit of V03 sample for: a) the yellow zone; b) the red spots from the bottom layer; c) the orange zone; d) micro-SORS profiles of the same regions.

possible to see the difference in intensity between the orange and yellow areas. In fact, the latter shows greater intensity due to its higher NIR absorbance. The two cover layers have respective depths of 500 µm for the yellow and 400 µm for the orange. The red spot belonging to the bottom layer shows a PA profile with a maximum peak shifted of about 500 µm compared to the signal of the top layers, in agreement with its real position.
However, since the very low signal associated with the orange layer hinders the estimation of the PA profile, we obtained only a curve with a medium value of 550 µm (Fig. 52(c)). Higher signals are generated from the yellow stratum, through which we were able to receive information also from the bottom layer, as shown by the deconvolution procedure in Fig. 52(a). In this case, we obtained a thickness of 490 µm for the yellow and an estimation of 600 µm for the substratum composed from the union of the red layer and the intonaco.

A comparison with the SORS profiles it is immediately possible by studying the graph of fig. 52(d), in which, for sake of brevity and clarity, we put only the first derivative of the depth curves. In this

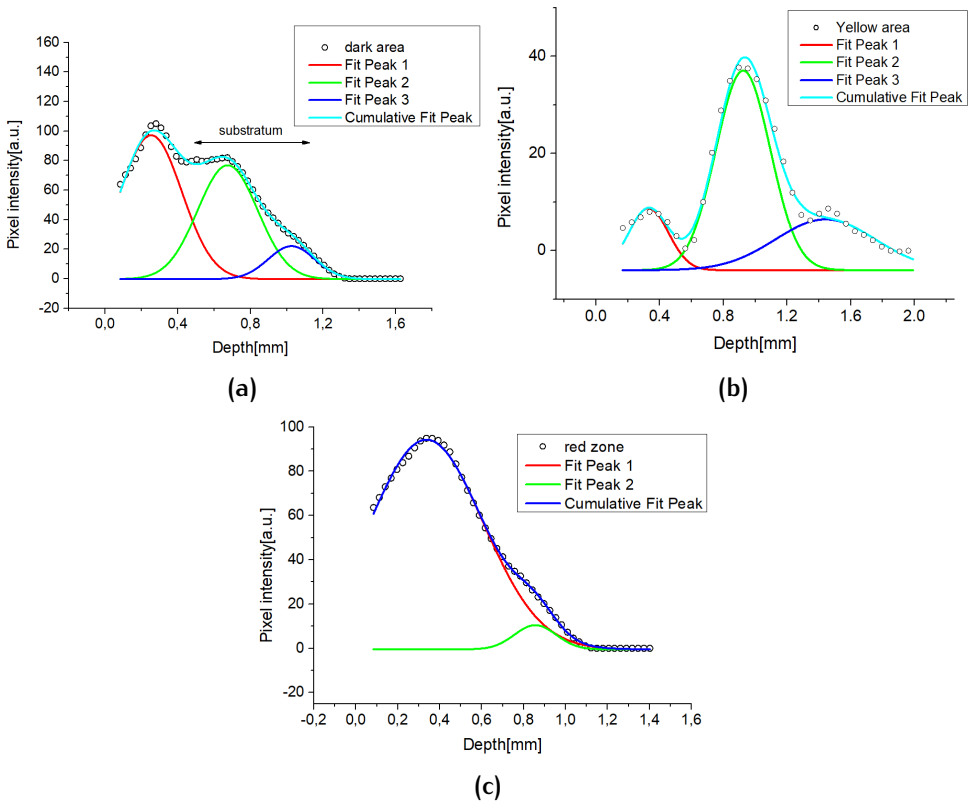

Figure 53: Layers fit of V.02 sample obtained from PA stratigraphic images for: a) the dark area, b) the yellow area, c) the red area.

case, we followed different relative ratios based on the compound present on the surface. For example, in the yellow area, we normalize

the spectra with a characteristic peak of CdS and we followed the distribution of calcite (1087 cm^{-1}), obtaining an average thickness of 400 µm for both the layers, yellow and red. In the red spots, we found only a minimum associated with the red layer with an average thickness of 300 µm. The orange zone revealed two minima, respectively around 370 and 800 µm. For what concerns the yellow top layer, the obtained value underestimates the real thickness, but it should be noted that the gathered information is derived from the average of different sampling points (inhomogeneous surface) and the combination of different compound profiles (different ratios). In addition, the SORS profile is linked to the depth of "defocusing", which does not always match the exact thickness of the sample under examination, as well explained by the literature [167–171].

Regarding sample V.02, PA and SORS profiles (see fig 53 and 54) show on the whole a bottom dark zone composed of only a layer of graphite (around 250-350 µm), in the middle the yellow area composed of two layers, the graphite seen before, and a cover layer of yellow cadmium of around 200-300 µm. Finally the red area is composed by the previous yellow layer covered by a stratum of red ocher (about 500-600 µm). In particular, as seen before for sample

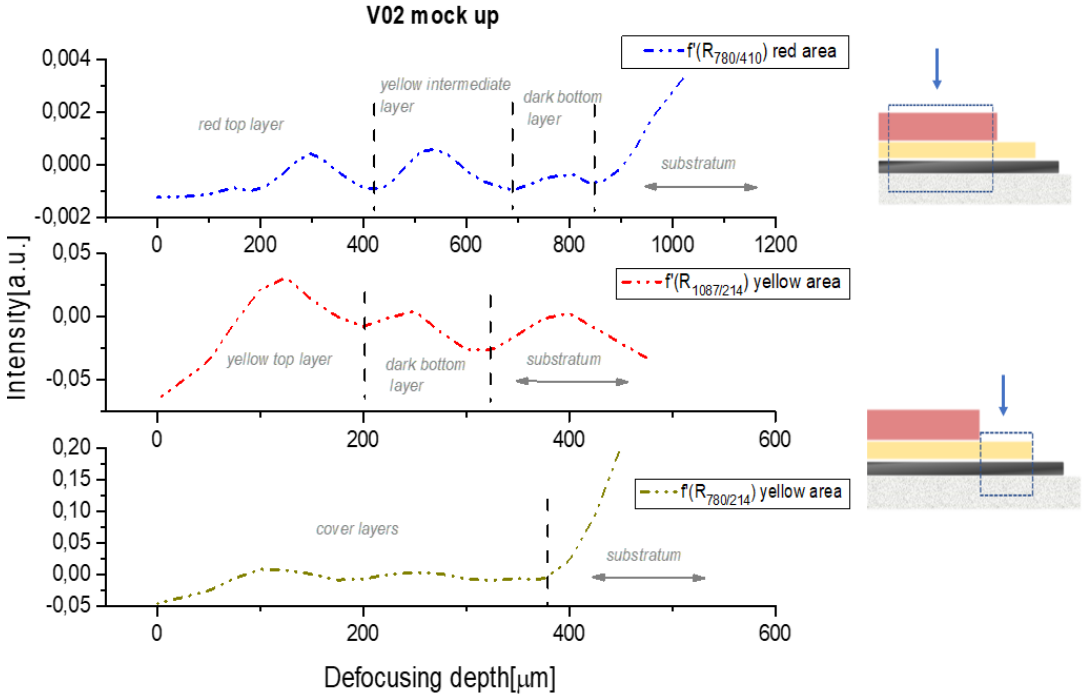

Figure 54: SORS analysis of V.02 sample

V.03, the yellow cadmium is not a good absorber of the NIR excitation source (very low pixel intensity associated with its signal), even if in figure 53(b) an identification of its thickness and the thickness of the dark layer below it is possible. In this case we obtained 300 µm for

the yellow stratum, 350 μm for the dark one, and a broad band of around 740 μm for the white substratum.
In fig 53(a) the dark zone was analyzed obtaining around 330 μm for the painted layer and a broad signal composed of different bands associated with the substratum until a maximum of 800 μm. For the red area (see figure 53(c)), the deconvolution showed two peaks, the intense one of about 600 μm associated with the red layer and a very weak shoulder for the underlying yellow layer of around 230 μm. No further information on other underlying layers can be obtainable from these PA images.
In fig. 54 we propose the SORS stratigraphic results obtained from the same area discussed before. Following the intensity ratio between the calcium hydroxide (780 cm^{-1}) and the hematite (410 cm^{-1}), starting the defocusing from the top red layer, we obtained tree pigmented layers with average thickness values of around 500 μm (red), 200 μm (yellow) and 150 μm (dark), followed by a white substratum which starts below 830 μm of depth. The values obtained with SORS technique are more accurate than the PA ones in this sample, even if there is a slight underestimation of the real thickness of the red layer, which could be explainable with the inhomogeneous surface.

These preliminary results show that, even if for thicknesses of more than 200 μm we can estimate with PA the fresco stratigraphy, their accuracy decreases as a function of the layer thickness (over 400 μm) and the absorbance at the source wavelength. The final result becomes quite approximate especially when the surface signal is weak. However, the combined use of SORS, even in such thicknesses, makes it possible to obtain information with a fair degree of accuracy, overcoming the PA limits encountered in some mock-up compositions.

3.5 SYNOPSIS OF THE OBTAINED RESULTS

In this chapter, we sought for the first time the exploration of the photoacoustic (PA) imaging potential using an excitation wavelength at 1064 nm to reveal the stratigraphy of highly turbid and inhomogeneous materials such as frescoes, combining it also with micro-SORS, using the same wavelength. The results of the PA on real samples were also complemented by studies on mock-ups of different thicknesses and realized with different materials to increase the information recovery of this novel approach and validate the obtained results. Although the frescoes are not homogenous and are characterized by grains of different sizes which can cause reflections of the main signal, an estimation of the stratigraphy of the painted surface is possible, and when the PA cannot properly work due to low absorbance from

the surface pigments, the SORS technique can be easily used.
This work is presented as a preliminary study on some frescoes mock-ups with the future aim to increase the variability of the fresco samples and systematically their thickness to achieve a maximum limit of the PA imaging accuracy. In addition, to overcome the limits encountered in this study, different excitation wavelengths could be employed to investigate layers presenting variable optical absorption and structural properties. Finally, a future goal will be to extend the versatility of the technique to other painting surfaces, such as canvas and pictorial panels, and combine it with other imaging techniques to obtain full knowledge of the sample under examination.

4 | CONCLUSION

In this research work, we sought to expand the knowledge in the diagnostics field of cultural heritage by using new experimental approaches.

In the first chapter, an extensive use of the Raman technique was made to develop a kinetic model based on the carbonation of calcium hydroxide. This work was preceded by a fine characterization of its Raman spectrum, resolving the open question on the nature of the band at 780 cm^{-1}. Following our experimental results, this band can be finally attributed to luminescence phenomena. The proposed kinetic model is only preliminary, and it could be improved by considering other factors that affect the rate of carbonation, such as the presence of organic coatings. This affination process will make it applicable as a correct dating model, regardless of the conditions beneath which the fresco was found and the method of its preservation.

In the second chapter, three famous pigments, the red vermilion known as cinnabar and two standard pigments used by the Impressionists, cadmium yellow and orange, were studied with artificial degradation processes. In the case of cinnabar, a careful characterization of its defects by pump and probe confirmed the phase variation attributable to its blackening. These results were also expected by a DFT-simulation. In the case of cadmium pigments, we found different degradation products such as sulphates, oxides, and the presence of cadmium vacancies through the application of various analytical and optical techniques. For the latter pigment, typically used in oil paintings, the study was also extended to the degradation of canvas and oil to define their contribution in the full degradation process. Future studies are aimed at the application of non-linear optics to study the degradation of the binder and the organic canvas, in order to obtain further information about their alteration.

In the third chapter, a new approach derived from the combination of photoacoustic technique and defocusing Raman micro-SORS was applied to analyze the stratigraphy of fresco paintings. With the aid of real samples and mock-ups, we attempted to explore the limits, potentiality, and complementary nature of these two methodologies in the stratigraphic reconstruction of the analyzed samples. Future efforts will be dedicated to extending the applicability of this new approach to other cultural heritage objects and developing a completely non-invasive methodology.

This thesis presents itself as an initial research work both on the

degradation of individual pigments and also for the application of new methodologies for diagnostics, which opens new insights and theories for the diagnostic investigation, conservation and restoration of cultural heritage.

BIBLIOGRAPHY

[1] R. Linn, E.H. Cline, and A. Yasur-Landau. "Technological study of Middle Bronze Age painted plaster fragments from the Canaanite Palace of Tel Kabri, Israel - materials and painting techniques". In: *Journal of Archaeological Science: Reports* 13 (2017), pp. 466–475. ISSN: 2352-409X. DOI: https://doi.org/10.1016/j.jasrep.2017.03.053. URL: https://www.sciencedirect.com/science/article/pii/S2352409X16305569.

[2] M. Horgnies et al. "An exceptionally perennial surface artwork: fresco on lime or on cement". In: *Surface and Interface Analysis* 46.10-11 (2014), pp. 791–795. DOI: https://doi.org/10.1002/sia.5392. eprint: https://analyticalsciencejournals.onlinelibrary.wiley.com/doi/pdf/10.1002/sia.5392. URL: https://analyticalsciencejournals.onlinelibrary.wiley.com/doi/abs/10.1002/sia.5392.

[3] R. PIOVESAN et al. "FRESCO AND LIME-PAINT: AN EXPERIMENTAL STUDY AND OBJECTIVE CRITERIA FOR DISTINGUISHING BETWEEN THESE PAINTING TECHNIQUES". In: *Archaeometry* 54.4 (2012), pp. 723–736. DOI: https://doi.org/10.1111/j.1475-4754.2011.00647.x. eprint: https://onlinelibrary.wiley.com/doi/pdf/10.1111/j.1475-4754.2011.00647.x. URL: https://onlinelibrary.wiley.com/doi/abs/10.1111/j.1475-4754.2011.00647.x.

[4] R. Camerini et al. "The carbonation kinetics of calcium hydroxide nanoparticles: A Boundary Nucleation and Growth description". In: *Journal of Colloid and Interface Science* 547 (2019), pp. 370–381. ISSN: 0021-9797. DOI: https://doi.org/10.1016/j.jcis.2019.03.089. URL: https://www.sciencedirect.com/science/article/pii/S002197971930387X.

[5] G. Montes-Hernandez et al. "Calcite precipitation from CO2–H2O–Ca(OH)2 slurry under high pressure of CO2". In: *Journal of Crystal Growth* 308.1 (2007), pp. 228–236. ISSN: 0022-0248. DOI: https://doi.org/10.1016/j.jcrysgro.2007.08.005. URL: https://www.sciencedirect.com/science/article/pii/S0022024807007099.

[6] G. Montes-Hernandez et al. "In situ kinetic measurements of gas–solid carbonation of Ca(OH)2 by using an infrared microscope coupled to a reaction cell". In: *Chemical Engineer-*

ing Journal 161.1 (2010), pp. 250–256. ISSN: 1385-8947. DOI: https://doi.org/10.1016/j.cej.2010.04.041. URL: https://www.sciencedirect.com/science/article/pii/S1385894710003839.

[7] Carlos Rodriguez-Navarro, Kerstin Elert, and Radek Ševčík. "Amorphous and crystalline calcium carbonate phases during carbonation of nanolimes: implications in heritage conservation". In: *CrystEngComm* 18 (35 2016), pp. 6594–6607. DOI: 10.1039/C6CE01202G. URL: http://dx.doi.org/10.1039/C6CE01202G.

[8] Shin-Min Shih et al. "Kinetics of the Reaction of Ca(OH)2 with CO2 at Low Temperature". In: *Industrial & Engineering Chemistry Research* 38.4 (1999), pp. 1316–1322. DOI: 10.1021/ie980508z. URL: https://doi.org/10.1021/ie980508z.

[9] Daniele Chiriu et al. "Portable NIR Raman microspectroscopy investigation on Early Bronze IV pottery (2500–1950 BCE) from Khirbat Iskandar, Jordan". In: *Vibrational Spectroscopy* 97 (2018), pp. 8–15. ISSN: 0924-2031. DOI: https://doi.org/10.1016/j.vibspec.2018.04.002. URL: https://www.sciencedirect.com/science/article/pii/S0924203118300353.

[10] Daniele Chiriu et al. "Drying oil detected in mid-third Millennium B.C. Mesopotamian clay artifacts: Raman spectroscopy and DFT simulation study". In: *Microchemical Journal* 124 (2016), pp. 386–395. ISSN: 0026-265X. DOI: https://doi.org/10.1016/j.microc.2015.09.013. URL: https://www.sciencedirect.com/science/article/pii/S0026265X15002143.

[11] "Raman characterization of XIV–XVI centuries Sardinian documents: Inks, papers and parchments". In: *Vibrational Spectroscopy* 92 (2017), pp. 70–81. ISSN: 0924-2031. DOI: https://doi.org/10.1016/j.vibspec.2017.05.007. URL: https://www.sciencedirect.com/science/article/pii/S0924203116303678.

[12] Daniele Chiriu et al. "Raman identification of cuneiform tablet pigments: emphasis and colour technology in ancient Mesopotamian mid-third millennium". In: *Heliyon* 3.3 (2017), e00272. ISSN: 2405-8440. DOI: https://doi.org/10.1016/j.heliyon.2017.e00272. URL: https://www.sciencedirect.com/science/article/pii/S2405844016319181.

[13] Daniele Chiriu et al. "Ageing of ancient paper: A kinetic model of cellulose degradation from Raman spectra". In: *Journal of Raman Spectroscopy* 49.11 (2018), pp. 1802–1811. DOI: https://doi.org/10.1002/jrs.5462. URL: https://

analyticalsciencejournals.onlinelibrary.wiley.com/doi/abs/10.1002/jrs.5462.

[14] D. Chiriu et al. "Time through colors: A kinetic model of red vermilion darkening from Raman spectra". In: *Dyes and Pigments* 184 (2021), p. 108866. ISSN: 0143-7208. DOI: https://doi.org/10.1016/j.dyepig.2020.108866. URL: https://www.sciencedirect.com/science/article/pii/S0143720820315631.

[15] Tae-Yub Kwon, Tatujiro Fujishima, and Yohji Imai. "FT-Raman spectroscopy of calcium hydroxide medicament in root canals." In: *International endodontic journal* 37 7 (2004), pp. 489–93.

[16] Thomas Schmid and Petra Dariz. "Shedding light onto the spectra of lime: Raman and luminescence bands of CaO, Ca(OH)2 and CaCO3". In: *Journal of Raman Spectroscopy* 46.1 (2015), pp. 141–146. DOI: https://doi.org/10.1002/jrs.4622. eprint: https://analyticalsciencejournals.onlinelibrary.wiley.com/doi/pdf/10.1002/jrs.4622. URL: https://analyticalsciencejournals.onlinelibrary.wiley.com/doi/abs/10.1002/jrs.4622.

[17] A Aminzadeh. "Fluorescence bands in the FT-Raman spectra of some calcium minerals". In: *Spectrochimica Acta Part A: Molecular and Biomolecular Spectroscopy* 53.5 (1997), pp. 693–697. ISSN: 1386-1425. DOI: https://doi.org/10.1016/S1386-1425(96)01848-3. URL: https://www.sciencedirect.com/science/article/pii/S1386142596018483.

[18] O. Chaix-Pluchery et al. "Evidence of a luminescence band during the thermal transformation of calcium hydroxide". In: *Journal of Solid State Chemistry* 73.2 (1988), pp. 563–566. ISSN: 0022-4596. DOI: https://doi.org/10.1016/0022-4596(88)90145-4. URL: https://www.sciencedirect.com/science/article/pii/0022459688901454.

[19] J. Llopis. "Luminescence of MgO and CaO Stabilized ZrO2 Crystals". In: *physica status solidi (a)* 119.2 (1990), pp. 661–667. DOI: https://doi.org/10.1002/pssa.2211190230. eprint: https://onlinelibrary.wiley.com/doi/pdf/10.1002/pssa.2211190230. URL: https://onlinelibrary.wiley.com/doi/abs/10.1002/pssa.2211190230.

[20] M. Blasse G. Aguilar. "Luminescence of natural calcite (CaCO3)." In: *J. of Luminescence* 29.2 (1984), pp. 239–241.

[21] Hua Wang et al. "Facile Synthesis of CaCo3 and CaCo3:Eu3+ Phosphors by Solid State Reaction at Room Temperature and the Luminescence Properties". In: *Materials Science Forum* 809

(Jan. 2015), pp. 711–718. DOI: 10.4028/www.scientific.net/MSF.809-810.711.

[22] E Dubina et al. "Influence of water vapour and carbon dioxide on free lime during storage at 80 C, studied by Raman spectroscopy". In: *Spectrochimica acta. Part A, Molecular and biomolecular spectroscopy* 111 (Apr. 2013). DOI: 10.1016/j.saa.2013.04.033.

[23] H. G. M. Edwards, E. R. Gwyer, and J. K. F. Tait. "Fourier Transform Raman analysis of paint fragments from biodeteriorated Renaissance frescoes". In: *Journal of Raman Spectroscopy* 28.9 (1997), pp. 677–684. DOI: https://doi.org/10.1002/(SICI)1097-4555(199709)28:9<677::AID-JRS159>3.0.CO;2-2. eprint: https://analyticalsciencejournals.onlinelibrary.wiley.com/doi/pdf/10.1002/%28SICI%291097-4555%28199709%2928%3A9%3C677%3A%3AAID-JRS159%3E3.0.CO%3B2-2. URL: https://analyticalsciencejournals.onlinelibrary.wiley.com/doi/abs/10.1002/%28SICI%291097-4555%28199709%2928%3A9%3C677%3A%3AAID-JRS159%3E3.0.CO%3B2-2.

[24] H. G. M. Edwards, E. R. Gwyer, and J. K. F. Tait. "Fourier Transform Raman analysis of paint fragments from biodeteriorated Renaissance frescoes". In: *Journal of Raman Spectroscopy* 28.9 (1997), pp. 677–684. DOI: https://doi.org/10.1002/(SICI)1097-4555(199709)28:9<677::AID-JRS159>3.0.CO;2-2. eprint: https://analyticalsciencejournals.onlinelibrary.wiley.com/doi/pdf/10.1002/%28SICI%291097-4555%28199709%2928%3A9%3C677%3A%3AAID-JRS159%3E3.0.CO%3B2-2. URL: https://analyticalsciencejournals.onlinelibrary.wiley.com/doi/abs/10.1002/%28SICI%291097-4555%28199709%2928%3A9%3C677%3A%3AAID-JRS159%3E3.0.CO%3B2-2.

[25] H.G.M. Edwards and D.W. Farwell. "The conservational heritage of wall paintings and buildings: An FT-Raman spectroscopic study of prehistoric, Roman, mediaeval and Renaissance lime substrates and mortars". In: *Journal of Raman Spectroscopy* 39 (2008). DOI: https://doi.org/10.1007/s00339-016-0370-7.

[26] H. G. M. Edwards, C. J. Brooke, and J. K. F. Tait. "Fourier Transform Raman Spectroscopic Study of Pigments from English Mediaeval Wall Paintings". In: *Journal of Raman Spectroscopy* 28.2-3 (), pp. 95–98. DOI: https://doi.org/10.1002/(SICI)1097-4555(199702)28:2/3<95::AID-JRS74>3.0.CO;2-0. URL: https://analyticalsciencejournals.onlinelibrary.wiley.

com/doi/abs/10.1002/%28SICI%291097-4555%28199702%2928%3A2/3%3C95%3A%3AAID-JRS74%3E3.0.CO%3B2-0.

[27] S. E. Jorge Villar et al. "Raman spectroscopic analysis of mediaeval wall paintings in the Palencia region, Spain". In: *Journal of Raman Spectroscopy* 37.10 (2006), pp. 1078–1085. DOI: https://doi.org/10.1002/jrs.1608. URL: https://analyticalsciencejournals.onlinelibrary.wiley.com/doi/abs/10.1002/jrs.1608.

[28] H. G. M. Edwards, D. W. Farwell, and S. Rozenberg. "Raman spectroscopic study of red pigment and fresco fragments from King Herod's Palace at Jericho". In: *Journal of Raman Spectroscopy* 30.5 (1999), pp. 361–366. DOI: https://doi.org/10.1002/(SICI)1097-4555(199905)30:5<361::AID-JRS383>3.0.CO;2-2. URL: https://analyticalsciencejournals.onlinelibrary.wiley.com/doi/abs/10.1002/%28SICI%291097-4555%28199905%2930%3A5%3C361%3A%3AAID-JRS383%3E3.0.CO%3B2-2.

[29] H.G.M. Edwards et al. "Romano-British wall-paintings II: Raman spectroscopic analysis of two villa sites at Nether Heyford, Northants". In: *Analytica Chimica Acta* 484.2 (2003), pp. 211–221. ISSN: 0003-2670. DOI: https://doi.org/10.1016/S0003-2670(03)00333-7. URL: https://www.sciencedirect.com/science/article/pii/S0003267003003337.

[30] H. G. M. Edwards et al. "Mediaeval Pigments in the Monastery of San Baudelio, Spain: A Raman Spectroscopic Analysis". In: *Applied Spectroscopy* 55.1 (2001), pp. 71–76. DOI: 10.1366/0003702011951272. URL: https://doi.org/10.1366/0003702011951272.

[31] D. Chiriu et al. "Beyond the surface: Raman micro-SORS for in depth non-destructive analysis of fresco layers". In: *Microchemical Journal* 153 (2020), p. 104404. ISSN: 0026-265X. DOI: https://doi.org/10.1016/j.microc.2019.104404. URL: https://www.sciencedirect.com/science/article/pii/S0026265X19325172.

[32] Zofia Kaszowska et al. "Raman scattering or fluorescence emission? Raman spectroscopy study on lime-based building and conservation materials". In: *Spectrochimica Acta Part A: Molecular and Biomolecular Spectroscopy* 169 (2016), pp. 7–15. ISSN: 1386-1425. DOI: https://doi.org/10.1016/j.saa.2016.06.012. URL: https://www.sciencedirect.com/science/article/pii/S1386142516303249.

[33] Barbara Lafuente et al. "1. The power of databases: The RRUFF project". In: *Highlights in Mineralogical Crystallography*. Ed. by Thomas Armbruster and Rosa Micaela Danisi. Berlin, München, Boston: De Gruyter (O), 2015, pp. 1–30. ISBN: 9783110417104. DOI: doi:10.1515/9783110417104-003. URL: https://doi.org/10.1515/9783110417104-003.

[34] O. Chaix-Pluchery et al. "Raman study of prereactional transformations in calcium hydroxide crystals during a thermal treatment leading to dehydration". In: *Journal of Solid State Chemistry* 53.2 (1984), pp. 273–276. ISSN: 0022-4596. DOI: https://doi.org/10.1016/0022-4596(84)90102-6. URL: https://www.sciencedirect.com/science/article/pii/0022459684901026.

[35] Toshifumi Sugama, G. Gray, and L. Kukacka. "Alkali carbonation of autoclaved polymer-cement composites in Na 2 CO 3 -laden water at 300C". In: *Journal of Materials Science - J MATER SCI* 27 (Feb. 1992), pp. 180–190. DOI: 10.1007/BF00553854.

[36] T. Sugama, L.E. Brothers, and T.R. Van de Putte. "Air-foamed calcium aluminate phosphate cement for geothermal wells". In: *Cement and Concrete Composites* 27.7 (2005), pp. 758–768. ISSN: 0958-9465. DOI: https://doi.org/10.1016/j.cemconcomp.2004.11.003. URL: https://www.sciencedirect.com/science/article/pii/S095894650500017X.

[37] Sang Hwan Cho et al. "Synthesis of Precipitated Calcium Carbonate Using a Limestone and its Application in Paper Filler and Coating Color". In: *Eco-Materials Processing and Design VIII*. Vol. 544. Materials Science Forum. Trans Tech Publications Ltd, May 2007, pp. 881–884. DOI: 10.4028/www.scientific.net/MSF.544-545.881.

[38] S. P. S. Porto, J. A. Giordmaine, and T. C. Damen. "Depolarization of Raman Scattering in Calcite". In: *Phys. Rev.* 147 (2 July 1966), pp. 608–611. DOI: 10.1103/PhysRev.147.608. URL: https://link.aps.org/doi/10.1103/PhysRev.147.608.

[39] Nicolae Buzgar and Andrei Apopei. "The Raman study of certain carbonates". In: *Anal. Şt. Univ. „Al. I. Cuza" Iaşi* LV (Jan. 2009), pp. 97–112.

[40] J. Kemperl and J. Maček. "Precipitation of calcium carbonate from hydrated lime of variable reactivity, granulation and optical properties". In: *International Journal of Mineral Processing* 93.1 (2009), pp. 84–88. ISSN: 0301-7516. DOI: https://doi.org/10.1016/j.minpro.2009.05.006. URL: https://www.sciencedirect.com/science/article/pii/S0301751609001409.

[41] Sandra Galmarini and Paul Bowen. "Atomistic simulation of the adsorption of calcium and hydroxyl ions onto portlandite surfaces — towards crystal growth mechanisms". In: *Cement and Concrete Research* 81 (2016), pp. 16–23. ISSN: 0008-8846. DOI: https://doi.org/10.1016/j.cemconres.2015.11.008. URL: https://www.sciencedirect.com/science/article/pii/S0008884615002914.

[42] R. Camerini et al. "The carbonation kinetics of calcium hydroxide nanoparticles: A Boundary Nucleation and Growth description". In: *Journal of Colloid and Interface Science* 547 (2019), pp. 370–381. ISSN: 0021-9797. DOI: https://doi.org/10.1016/j.jcis.2019.03.089. URL: https://www.sciencedirect.com/science/article/pii/S002197971930387X.

[43] M. N. Wetmore. In: *The Classical Weekly* 9.15 (1916), pp. 116–118. ISSN: 1940641X. URL: http://www.jstor.org/stable/4387224 (visited on 10/07/2022).

[44] BRIAN DIX. "THE MANUFACTURE of LIME and ITS USES IN the WESTERN ROMAN PROVINCES". In: *Oxford Journal of Archaeology* 1.3 (1982), pp. 331–346. DOI: https://doi.org/10.1111/j.1468-0092.1982.tb00318.x. eprint: https://onlinelibrary.wiley.com/doi/pdf/10.1111/j.1468-0092.1982.tb00318.x. URL: https://onlinelibrary.wiley.com/doi/abs/10.1111/j.1468-0092.1982.tb00318.x.

[45] Carlos Rodriguez-Navarro, Eric Hansen, and William S. Ginell. "Calcium Hydroxide Crystal Evolution upon Aging of Lime Putty". In: *Journal of the American Ceramic Society* 81.11 (1998), pp. 3032–3034. DOI: https://doi.org/10.1111/j.1151-2916.1998.tb02735.x. URL: https://ceramics.onlinelibrary.wiley.com/doi/abs/10.1111/j.1151-2916.1998.tb02735.x.

[46] I. Galan et al. "Assessment of the protective effect of carbonation on portlandite crystals". In: *Cement and Concrete Research* 74 (2015), pp. 68–77. ISSN: 0008-8846. DOI: https://doi.org/10.1016/j.cemconres.2015.04.001. URL: https://www.sciencedirect.com/science/article/pii/S0008884615001076.

[47] Núria Oriols et al. "Amorphous calcium carbonate (ACC) in fresco mural paintings". In: *Microchemical Journal* 154 (2020), p. 104567. ISSN: 0026-265X. DOI: https://doi.org/10.1016/j.microc.2019.104567. URL: https://www.sciencedirect.com/science/article/pii/S0026265X19320223.

[48] Mohan D. Tongaria K. Mandal S. "Review on Carbonation of Concrete and Its Prediction Modelling." In: *J. Environ. Nan-*

otechnol. 7.4 (2018), pp. 76–91. URL: https://doi.org/10.13074/jent.2018.12.184325.

[49] D. O. McPolin, P. A. Basheer, and A. E. Long. "Carbonation and pH in Mortars Manufactured with Supplementary Cementitious Materials". In: *Journal of Materials in Civil Engineering* 21.5 (2009), pp. 217–225. DOI: 10.1061/(ASCE)0899-1561(2009)21:5(217). eprint: https://ascelibrary.org/doi/pdf/10.1061/%28ASCE%290899-1561%282009%2921%3A5%28217%29. URL: https://ascelibrary.org/doi/abs/10.1061/%28ASCE%290899-1561%282009%2921%3A5%28217%29.

[50] Ali Behnood, Kim Van Tittelboom, and Nele De Belie. "Methods for measuring pH in concrete: A review". In: *Construction and Building Materials* 105 (2016), pp. 176–188. ISSN: 0950-0618. DOI: https://doi.org/10.1016/j.conbuildmat.2015.12.032. URL: https://www.sciencedirect.com/science/article/pii/S0950061815307054.

[51] Björn Lagerblad. "Carbon Dioxide Uptake during Concrete Life Cycle - State of the Art". In: 2005.

[52] Costas G. Vayenas Vagelis G. Papadakis and Michael N. Fardis. "Fundamental Modeling and Experimental Investigation of Concrete Carbonation". In: *Materials Journal* 88 (4 1991), pp. 363–373.

[53] N. Bouzoubaâ et al. "Carbonation of fly ash concrete: laboratory and field data". In: *Canadian Journal of Civil Engineering* 37.12 (2010), pp. 1535–1549. DOI: 10.1139/L10-081. eprint: https://doi.org/10.1139/L10-081. URL: https://doi.org/10.1139/L10-081.

[54] M. A. Mansur S. Nagataki and H. Ohga. "Carbonation of Mortar in Relation to Ferrocement Construction". In: *Materials Journal* 85 (1 1988), pp. 17–25.

[55] A. Younsi et al. "Accelerated carbonation of concrete with high content of mineral additions: Effect of interactions between hydration and drying". In: *Cement and Concrete Research* 43 (2013), pp. 25–33. ISSN: 0008-8846. DOI: https://doi.org/10.1016/j.cemconres.2012.10.008. URL: https://www.sciencedirect.com/science/article/pii/S0008884612002219.

[56] Treval Clifford Powers. "A DISCUSSION OF CEMENT HYDRATION IN RELATION TO THE CURING OF CONCRETE". In: 1948.

[57] Hongzhi Cui et al. "Experimental study on effects of CO2 concentrations on concrete carbonation and diffusion mechanisms". In: *Construction and Building Materials* 93 (2015), pp. 522–527. ISSN: 0950-0618. DOI: https://doi.org/10.1016/j.conbuildmat.2015.06.007. URL: https://www.sciencedirect.com/science/article/pii/S0950061815006844.

[58] Qian Zhang. "Mathematical modeling and numerical study of carbonation in porous concrete materials". In: *Applied Mathematics and Computation* 281 (2016), pp. 16–27. ISSN: 0096-3003. DOI: https://doi.org/10.1016/j.amc.2016.01.034. URL: https://www.sciencedirect.com/science/article/pii/S0096300316300340.

[59] V. G. Papadakis, C. G. Vayenas, and M. N. Fardis. "A reaction engineering approach to the problem of concrete carbonation". In: *AIChE Journal* 35.10 (1989), pp. 1639–1650. DOI: https://doi.org/10.1002/aic.690351008. eprint: https://aiche.onlinelibrary.wiley.com/doi/pdf/10.1002/aic.690351008. URL: https://aiche.onlinelibrary.wiley.com/doi/abs/10.1002/aic.690351008.

[60] V. G. Papadakis, C. G. Vayenas, and M. N. Fardis. "Physical and chemical characteristics affecting the durability of concrete." In: *ACI Mater. J* 88 (1991), pp. 186–196.

[61] Vagelis G. Papadakis, Costas G. Vayenas, and Michael N. Fardis. "Experimental investigation and mathematical modeling of the concrete carbonation problem". In: *Chemical Engineering Science* 46.5 (1991), pp. 1333–1338. ISSN: 0009-2509. DOI: https://doi.org/10.1016/0009-2509(91)85060-B. URL: https://www.sciencedirect.com/science/article/pii/000925099185060B.

[62] Willemien Anaf et al. "Understanding the (in)stability of semiconductor pigments by a thermodynamic approach". In: *Dyes and Pigments* 113 (2015), pp. 409–415. ISSN: 0143-7208. DOI: https://doi.org/10.1016/j.dyepig.2014.09.015. URL: https://www.sciencedirect.com/science/article/pii/S0143720814003684.

[63] Willemien Anaf et al. "Electrochemical Photodegradation Study of Semiconductor Pigments: Influence of Environmental Parameters". In: *Analytical Chemistry* 86.19 (2014), pp. 9742–9748. DOI: 10.1021/ac502303z.

[64] Francesca Assunta Pisu et al. "Defect Related Emission in Calcium Hydroxide: The Controversial Band at 780 cm1". In: *Crystals* 10.4 (2020). ISSN: 2073-4352. DOI: 10.3390/cryst10040266.

[65] Francesca Assunta Pisu et al. "Fresco Paintings: Development of an Aging Model from 1064 nm Excited Raman Spectra". In: *Crystals* 11.3 (2021). ISSN: 2073-4352. DOI: 10.3390/cryst11030257.

[66] Anna M. Gueli et al. "Effect of particle size on pigments colour". In: *Color Research & Application* 42.2 (2017), pp. 236–243. DOI: https://doi.org/10.1002/col.22062.

[67] Jessie Harrison et al. "The influence of light and relative humidity on the formation of epsomite in cadmium yellow and French ultramarine modern oil paints". In: *Heritage Science* 9 (2021). ISSN: 2050-7445. DOI: 10.1186/s40494-021-00569-2.

[68] Francesca Rosi et al. "UV–Vis-NIR and micro Raman spectroscopies for the non destructive identification of Cd1xZnxS solid solutions in cadmium yellow pigments". In: *Microchemical Journal* 124 (2016), pp. 856–867. ISSN: 0026-265X. DOI: https://doi.org/10.1016/j.microc.2015.07.025.

[69] Daniela Comelli et al. "Degradation of Cadmium Yellow Paint: New Evidence from Photoluminescence Studies of Trap States in Picasso's Femme (Époque des "Demoiselles d'Avignon")". In: *Analytical Chemistry* 91 (2019/03/05). ISSN: 0003-2700. DOI: 10.1021/acs.analchem.8b04914.

[70] Daniele Chiriu et al. "Raman identification of cuneiform tablet pigments: emphasis and colour technology in ancient Mesopotamian mid-third millennium". In: *Heliyon* 3.3 (2017), e00272. ISSN: 2405-8440. DOI: https://doi.org/10.1016/j.heliyon.2017.e00272.

[71] Daniele Chiriu et al. "Application of Raman Spectroscopy to Ancient Materials: Models and Results from Archaeometric Analyses". In: *Materials* 13.11 (2020). ISSN: 1996-1944. DOI: 10.3390/ma13112456. URL: https://www.mdpi.com/1996-1944/13/11/2456.

[72] D. Chiriu et al. "Time through colors: A kinetic model of red vermilion darkening from Raman spectra". In: *Dyes and Pigments* 184 (2021), p. 108866. ISSN: 0143-7208. DOI: https://doi.org/10.1016/j.dyepig.2020.108866. URL: https://www.sciencedirect.com/science/article/pii/S0143720820315631.

[73] Daniele Chiriu et al. "Raman identification of cuneiform tablet pigments: emphasis and colour technology in ancient Mesopotamian mid-third millennium". In: *Heliyon* 3.3 (2017), e00272. ISSN: 2405-8440. DOI: https://doi.org/10.1016/j.heliyon.2017.e00272. URL: https://www.sciencedirect.com/science/article/pii/S2405844016319181.

[74] Francesca Assunta Pisu et al. "Fresco Paintings: Development of an Aging Model from 1064 nm Excited Raman Spectra". In: *Crystals* 11.3 (2021). ISSN: 2073-4352. DOI: 10.3390/cryst11030257. URL: https://www.mdpi.com/2073-4352/11/3/257.

[75] Jin Yu, Warren S. Warren, and Martin C. Fischer. "Visualization of vermilion degradation using pump-probe microscopy". In: *Science Advances* 5.6 (2019), eaaw3136. DOI: 10.1126/sciadv.aaw3136. eprint: https://www.science.org/doi/pdf/10.1126/sciadv.aaw3136. URL: https://www.science.org/doi/abs/10.1126/sciadv.aaw3136.

[76] Tana E. Villafaña et al. "Historical Pigments Revealed by Pump-Probe Microscopy". In: *Frontiers in Optics 2012/Laser Science XXVIII*. Optica Publishing Group, 2012, p. LM3I.5. DOI: 10.1364/LS.2012.LM3I.5. URL: https://opg.optica.org/abstract.cfm?URI=LS-2012-LM3I.5.

[77] Martin C. Fischer et al. "Invited Review Article: Pump-probe microscopy". In: *Review of Scientific Instruments* 87.3 (2016), p. 031101. DOI: 10.1063/1.4943211. URL: https://aip.scitation.org/doi/abs/10.1063/1.4943211.

[78] Jason K. Cooper et al. "Physical Origins of the Transient Absorption Spectra and Dynamics in Thin-Film Semiconductors: The Case of $BiVO_4$". In: *The Journal of Physical Chemistry C* 122.36 (2018), pp. 20642–20652. DOI: 10.1021/acs.jpcc.8b06645.

[79] Rudi Berera, Rienk van Grondelle, and John T. M. Kennis. "Ultrafast transient absorption spectroscopy: principles and application to photosynthetic systems". In: *Photosynthesis Research* 101 (2009). DOI: 10.1007/s11120-009-9454-y.

[80] Elsa M. Garmire. "Photonics: Linear and Nonlinear Interactions of Laser Light and Matter". In: *Physics Today* 55.3 (2002), pp. 68–68. DOI: 10.1063/1.1472399. URL: https://doi.org/10.1063/1.1472399.

[81] K. Elert and C. Cardell. "Weathering behavior of cinnabar-based tempera paints upon natural and accelerated aging". In: *Spectrochimica Acta Part A: Molecular and Biomolecular Spectroscopy* 216 (2019), pp. 236–248. ISSN: 1386-1425. DOI: https://doi.org/10.1016/j.saa.2019.03.027. URL: https://www.sciencedirect.com/science/article/pii/S138614251930263X.

[82] Marie Radepont et al. "Thermodynamic and experimental study of the degradation of the red pigment mercury sulfide". In: *J. Anal. At. Spectrom.* 30 (3 2015), pp. 599–612. DOI: 10.1039/C4JA00372A. URL: http://dx.doi.org/10.1039/C4JA00372A.

[83] C. Hogan and F. Da Pieve. "Colour degradation of artworks: an ab initio approach to X-ray, electronic and optical spectroscopy analyses of vermilion photodarkening". In: *J. Anal. At. Spectrom.* 30 (3 2015), pp. 588–598. DOI: 10.1039/C4JA00327F. URL: http://dx.doi.org/10.1039/C4JA00327F.

[84] RUTHERFORD J. GETTENS, ROBERT L. FELLER, and W. T. CHASE. "VERMILION AND CINNABAR". In: *Studies in Conservation* 17.2 (1972), pp. 45–69. DOI: 10.1179/sic.1972.006. URL: https://doi.org/10.1179/sic.1972.006.

[85] Marie Radepont. "Understanding of chemical reactions involved in pigment discoloration, in particular in mercury sulfide (HgS) blackening". In: 2013.

[86] Paolo Ballirano, Michela Botticelli, and Adriana Maras. "Thermal behaviour of cinnabar, α-HgS, and the kinetics of the β-HgS (metacinnabar) - α-HgS conversion at room temperature". In: *European Journal of Mineralogy* 25.6 (Mar. 2014), pp. 957–965. DOI: 10.1127/0935-1221/2013/0025-2341. URL: http://dx.doi.org/10.1127/0935-1221/2013/0025-2341.

[87] Robert L. Feller. "Studies on the Darkening of Vermilion by Light". In: *Report and Studies in the History of Art* 1 (1967), pp. 99–111. ISSN: 00801240, 23729007. URL: http://www.jstor.org/stable/42618061.

[88] Katrien Keune and Jaap J. Boon. "Analytical Imaging Studies Clarifying the Process of the Darkening of Vermilion in Paintings". In: *Analytical Chemistry* 77.15 (2005). PMID: 16053284, pp. 4742–4750. DOI: 10.1021/ac048158f. URL: https://doi.org/10.1021/ac048158f.

[89] Xiaoming Duan and Xiaojun Li. "Exploring the influence of water molecules on the stability of the cinnabar oxides". In: *Chemical Physics Letters* 747 (2020), p. 137351. ISSN: 0009-2614. DOI: https://doi.org/10.1016/j.cplett.2020.137351. URL: https://www.sciencedirect.com/science/article/pii/S0009261420302669.

[90] Jin Yu, Warren S. Warren, and Martin C. Fischer. "Visualization of vermilion degradation using pump-probe microscopy". In: *Science Advances* 5.6 (2019), eaaw3136. DOI: 10.1126/sciadv.aaw3136. eprint: https://www.science.org/doi/pdf/10.1126/sciadv.aaw3136. URL: https://www.science.org/doi/abs/10.1126/sciadv.aaw3136.

[91] M. Spring and R. Grout. "The Blackening of Vermilion: An Analytical Study of the Process in Paintings". In: *National Gallery Technical Bulletin* 23 (2002), pp. 50–61. DOI: https://doi.org/10.1002/col.5080050319.

[92] John K. McCormack. "The darkening of cinnabar in sunlight". In: *Mineralium Deposita* 35 (2000), pp. 796–798.

[93] F. Da Pieve et al. "Casting Light on the Darkening of Colors in Historical Paintings". In: *Phys. Rev. Lett.* 111 (20 Nov. 2013), p. 208302. DOI: 10.1103/PhysRevLett.111.208302. URL: https://link.aps.org/doi/10.1103/PhysRevLett.111.208302.

[94] Marine Cotte et al. "Blackening of Pompeian cinnabar paintings: X-ray microspectroscopy analysis." In: *Analytical chemistry* 78 21 (2006), pp. 7484–92.

[95] Neiman MK, Balonis M, and Kakoulli I. "Cinnabar alteration in archaeological wall paintings: an experimental and theoretical approach." In: *Appl Phys A Mater Sci Process* (2015). DOI: https://doi.org/10.1007/s00339-015-9456-x..

[96] Marie Radepont et al. "The use of microscopic X-ray diffraction for the study of HgS and its degradation products corderoite (-Hg3S2Cl2), kenhsuite (-Hg3S2Cl2) and calomel (Hg2Cl2) in historical paintings". In: *J. Anal. At. Spectrom.* 26 (5 2011), pp. 959–968. DOI: 10.1039/C0JA00260G. URL: http://dx.doi.org/10.1039/C0JA00260G.

[97] D. Chiriu et al. "Time through colors: A kinetic model of red vermilion darkening from Raman spectra". In: *Dyes and Pigments* 184 (2021), p. 108866. ISSN: 0143-7208. DOI: https://doi.org/10.1016/j.dyepig.2020.108866. URL: https://www.sciencedirect.com/science/article/pii/S0143720820315631.

[98] R. W. Potter and H. L. Barnes. "Phase relations in the binary Hg-S". In: *American Mineralogist* 63.11-12 (Dec. 1978), pp. 1143–1152. ISSN: 0003-004X.

[99] Frank W Dickson and George Tunell. "The stability relations of cinnabar and metacinnabar". In: *American Mineralogist: Journal of Earth and Planetary Materials* 44.5-6 (1959), pp. 471–487.

[100] Margareta Svensson, Anders Düker, and Bert Allard. "Formation of cinnabar—estimation of favourable conditions in a proposed Swedish repository". In: *Journal of Hazardous Materials* 136.3 (2006), pp. 830–836. ISSN: 0304-3894. DOI: https://doi.org/10.1016/j.jhazmat.2006.01.018. URL: https://www.sciencedirect.com/science/article/pii/S0304389406000409.

[101] Willemien Anaf, Koen Janssens, and Karolien De Wael. "Formation of Metallic Mercury During Photodegradation/Photodarkening of -HgS: Electrochemical Evidence". In: *Angewandte Chemie International Edition* 52.48 (2013), pp. 12568–12571. DOI: https://doi.org/10.1002/anie.201303977. URL: https://onlinelibrary.wiley.com/doi/abs/10.1002/anie.201303977.

[102] E. Doni et al. "Electronic energy levels of cinnabar (α-HgS)". In: *Phys. Rev. B* 20 (4 Aug. 1979), pp. 1663–1668. DOI: 10.1103/PhysRevB.20.1663. URL: https://link.aps.org/doi/10.1103/PhysRevB.20.1663.

[103] M. Cardona et al. "Electronic, vibrational, and thermodynamic properties of metacinnabar β-HgS, HgSe, and HgTe". In: *Phys. Rev. B* 80 (19 Nov. 2009), p. 195204. DOI: 10.1103/PhysRevB.80.195204. URL: https://link.aps.org/doi/10.1103/PhysRevB.80.195204.

[104] P.R. Jubu et al. "Tauc-plot scale and extrapolation effect on bandgap estimation from UV–vis–NIR data – A case study of -Ga2O3". In: *Journal of Solid State Chemistry* 290 (2020), p. 121576. ISSN: 0022-4596. DOI: https://doi.org/10.1016/j.jssc.2020.121576. URL: https://www.sciencedirect.com/science/article/pii/S0022459620304060.

[105] J. Tauc, R. Grigorovici, and A. Vancu. "Optical Properties and Electronic Structure of Amorphous Germanium". In: *physica status solidi (b)* 15.2 (1966), pp. 627–637. DOI: https://doi.org/10.1002/pssb.19660150224. eprint: https://onlinelibrary.wiley.com/doi/pdf/10.1002/pssb.19660150224. URL: https://onlinelibrary.wiley.com/doi/abs/10.1002/pssb.19660150224.

[106] SUNIL KUMAR, M. KHORASANINEJAD, and M. M. ADACHI. "Probing ultrafast carrier dynamics, nonlinear absorption and refraction in core–shell silicon nanowires". In: *Pramana* 79 (2012). DOI: 10.1007/s12043-012-0337-y.

[107] Kathryn E. Knowles, Melissa D. Koch, and Jacob L. Shelton. "Three applications of ultrafast transient absorption spectroscopy of semiconductor thin films: spectroelectrochemistry, microscopy, and identification of thermal contributions". In: *J. Mater. Chem. C* 6 (44 2018), pp. 11853–11867. DOI: 10.1039/C8TC02977F. URL: http://dx.doi.org/10.1039/C8TC02977F.

[108] Janneke Ravensbergen et al. "Unraveling the Carrier Dynamics of BiVO4: A Femtosecond to Microsecond Transient Absorption Study". In: *The Journal of Physical Chemistry C* 118.48

(2014), pp. 27793–27800. DOI: 10.1021/jp509930s. URL: https://doi.org/10.1021/jp509930s.

[109] Mohammad Adnan and G. Vijaya Prakash. "Study of Surface and Bulk Recombination Kinetics of Two-Dimensional Inorganicâ"Organic Hybrid Semiconductors under Linear and Nonlinear Femtosecond Transient Absorption Analysis". In: *The Journal of Physical Chemistry C* 125.22 (2021), pp. 12166–12174. DOI: 10.1021/acs.jpcc.1c02351. URL: https://doi.org/10.1021/acs.jpcc.1c02351.

[110] Mi He et al. "Third-order nonlinear optical properties of WTe2 films synthesized by pulsed laser deposition". In: *Photon. Res.* 7.12 (Dec. 2019), pp. 1493–1500. DOI: 10.1364/PRJ.7.001493. URL: http://opg.optica.org/prj/abstract.cfm?URI=prj-7-12-1493.

[111] Mohammad Adnan and G. Vijaya Prakash. "Study of Surface and Bulk Recombination Kinetics of Two-Dimensional Inorganicâ"Organic Hybrid Semiconductors under Linear and Nonlinear Femtosecond Transient Absorption Analysis". In: *The Journal of Physical Chemistry C* 125.22 (2021), pp. 12166–12174. DOI: 10.1021/acs.jpcc.1c02351.

[112] Kuai Yu, Lakshminarayana Polavarapu, and Qing-Hua Xu. "Excitation wavelength and fluence dependent femtosecond transient absorption studies on electron dynamics of gold nanorods". In: *J Phys Chem A* 115 (2011). DOI: 10.1021/jp108176h.

[113] Jiong Yang, Renjing Xu, and Jiajie Pei. "tuning of exciton and trion emissions in monolayer phosphorene". In: *Light: Science Applications* 4 (2015). DOI: 10.1038/lsa.2015.85.

[114] Paolo Giannozzi et al. "QUANTUM ESPRESSO: a modular and open-source software project for quantum simulations of materials". In: *Journal of Physics: Condensed Matter* 21.39 (Sept. 2009), p. 395502. DOI: 10.1088/0953-8984/21/39/395502. URL: https://doi.org/10.1088/0953-8984/21/39/395502.

[115] J. P. Perdew and Alex Zunger. "Self-interaction correction to density-functional approximations for many-electron systems". In: *Phys. Rev. B* 23 (10 May 1981), pp. 5048–5079. DOI: 10.1103/PhysRevB.23.5048. URL: https://link.aps.org/doi/10.1103/PhysRevB.23.5048.

[116] G. Kresse and J. Furthmüller. "Efficient iterative schemes for ab initio total-energy calculations using a plane-wave basis set". In: *Phys. Rev. B* 54 (16 Oct. 1996), pp. 11169–11186. DOI: 10.1103/PhysRevB.54.11169. URL: https://link.aps.org/doi/10.1103/PhysRevB.54.11169.

[117] P. E. Blöchl. "Projector augmented-wave method". In: *Phys. Rev. B* 50 (24 Dec. 1994), pp. 17953–17979. DOI: 10.1103/PhysRevB.50.17953. URL: https://link.aps.org/doi/10.1103/PhysRevB.50.17953.

[118] R. Zallen. *II-VI Semiconducting compounds*. Benjamin,NY: D.G. Thomas, 1967, p. 877.

[119] J. William Shank. In: *Leonardo* 22.2 (1989), pp. 267–268. ISSN: 0024094X, 15309282. URL: http://www.jstor.org/stable/1575245 (visited on 10/06/2022).

[120] J.R. Barnett, Sarah Miller, and Emma Pearce. "Colour and art: A brief history of pigments". In: *Optics Laser Technology* 38.4 (2006). Colour and Design in the natural and man-made worlds, pp. 445–453. ISSN: 0030-3992. DOI: https://doi.org/10.1016/j.optlastec.2005.06.005. URL: https://www.sciencedirect.com/science/article/pii/S0030399205001076.

[121] Geert Van der Snickt et al. "Characterization of a Degraded Cadmium Yellow (CdS) Pigment in an Oil Painting by Means of Synchrotron Radiation Based X-ray Techniques". In: *Analytical Chemistry* 81.7 (2009). PMID: 19278249, pp. 2600–2610. DOI: 10.1021/ac802518z. URL: https://doi.org/10.1021/ac802518z.

[122] Jennifer Mass et al. "SR-FTIR imaging of the altered cadmium sulfide yellow paints in Henri Matisse's Le Bonheur de vivre (1905–6) – examination of visually distinct degradation regions". In: *Analyst* 138 (20 2013), pp. 6032–6043. DOI: 10.1039/C3AN00892D. URL: http://dx.doi.org/10.1039/C3AN00892D.

[123] E Pouyet et al. "2D X-ray and FTIR micro-analysis of the degradation of cadmium yellow pigment in paintings of Henri Matisse". In: *Applied Physics A* 121 (2015). DOI: 10.1007/s00339-015-9239-4.

[124] Geert Van der Snickt et al. "Combined use of Synchrotron Radiation Based Micro-X-ray Fluorescence, Micro-X-ray Diffraction, Micro-X-ray Absorption Near-Edge, and Micro-Fourier Transform Infrared Spectroscopies for Revealing an Alternative Degradation Pathway of the Pigment Cadmium Yellow in a Painting by Van Gogh". In: *Analytical Chemistry* 84.23 (2012). PMID: 22931047, pp. 10221–10228. DOI: 10.1021/ac3015627. URL: https://doi.org/10.1021/ac3015627.

[125] Daniela Comelli et al. "Degradation of Cadmium Yellow Paint: New Evidence from Photoluminescence Studies of Trap States in Picasso's Femme (Époque des "Demoiselles d'Avignon")". In: *Analytical Chemistry* 91.5 (2019). PMID: 30706704, pp. 3421–

3428. DOI: 10.1021/acs.analchem.8b04914. URL: https://doi.org/10.1021/acs.analchem.8b04914.

[126] R.W. Traill R.J.; Boyle. "Hawelite, Isometric Cadmium Sulphide, A New Mineral." In: *Am. Mineral. J. Earth Planet. Mater* (1955).

[127] N. Armani et al. "Role of thermal treatment on the luminescence properties of CdTe thin films for photovoltaic applications". In: *Thin Solid Films* 515.15 (2007). Proceedings of Symposium O on Thin Film Chalcogenide Photovoltaic Materials, EMRS 2006 Conference, pp. 6184–6187. ISSN: 0040-6090. DOI: https://doi.org/10.1016/j.tsf.2006.12.080. URL: https://www.sciencedirect.com/science/article/pii/S0040609006016312.

[128] Yuzun Fan et al. "Effect of calcination on the photocatalytic performance of CdS under visible light irradiation". In: *Journal of Alloys and Compounds* 509.5 (2011), pp. 1477–1481. ISSN: 0925-8388. DOI: https://doi.org/10.1016/j.jallcom.2010.10.044.

[129] Letizia Monico et al. "Role of the Relative Humidity and the Cd/Zn Stoichiometry in the Photooxidation Process of Cadmium Yellows (CdS/Cd1xZnxS) in Oil Paintings". In: *Chemistry – A European Journal* 24.45 (2018), pp. 11584–11593. DOI: https://doi.org/10.1002/chem.201801503.

[130] M.M. Mikhailov et al. "The effects of heating on $BaSO_4$ powders' diffuse reflectance spectra and radiation stability". In: *Dyes and Pigments* 163 (2019), pp. 420–424. ISSN: 0143-7208. DOI: https://doi.org/10.1016/j.dyepig.2018.12.022. URL: https://www.sciencedirect.com/science/article/pii/S0143720818307484.

[131] G. RIVEROS et al. "ELECTRODEPOSITION AND CHARACTERIZATION OF ZnX (X=Se, Te) SEMICONDUCTOR THIN FILMS". en. In: *BoletÃn de la Sociedad Chilena de QuÃmica* 47 (Dec. 2002), pp. 411–429. ISSN: 0366-1644. URL: http://www.scielo.cl/scielo.php?script=sci_arttext&pid=S0366-16442002000400013&nrm=iso.

[132] R.E. Marotti et al. "Bandgap energy tuning of electrochemically grown ZnO thin films by thickness and electrodeposition potential". In: *Solar Energy Materials and Solar Cells* 82.1 (2004). CANCUN 2003, pp. 85–103. ISSN: 0927-0248. DOI: https://doi.org/10.1016/j.solmat.2004.01.008. URL: https://www.sciencedirect.com/science/article/pii/S0927024804000091.

[133] R. Henríquez et al. "Optical properties of CdSe and CdO thin films electrochemically prepared". In: *Thin Solid Films* 518.7 (2010). Photovoltaics, solar energy materials and thin films - IMRC 2008, Cancun, Mexico, pp. 1774–1778. ISSN: 0040-6090. DOI: https://doi.org/10.1016/j.tsf.2009.09.030. URL: https://www.sciencedirect.com/science/article/pii/S0040609009014771.

[134] P K Nair et al. "Formation of conductive CdO layer on CdS thin films during air heating". In: *Semiconductor Science and Technology* 16.8 (June 2001), pp. 651–656. DOI: 10.1088/0268-1242/16/8/302. URL: https://doi.org/10.1088/0268-1242/16/8/302.

[135] Anna Maria Gueli, Salvatore Gallo, and Stefania Pasquale. "Optical and colorimetric characterization on binary mixtures prepared with coloured and white historical pigments". In: *Dyes and Pigments* 157 (2018), pp. 342–350. ISSN: 0143-7208. DOI: https://doi.org/10.1016/j.dyepig.2018.04.068. URL: https://www.sciencedirect.com/science/article/pii/S0143720817324683.

[136] Anna Cesaratto et al. "Analysis of cadmium-based pigments with time-resolved photoluminescence". In: *Anal. Methods* 6 (1 2014), pp. 130–138. DOI: 10.1039/C3AY41585F. URL: http://dx.doi.org/10.1039/C3AY41585F.

[137] B. S. Zou, V. V. Volkov, and Z. L. Wang. "Optical Properties of Amorphous ZnO, CdO, and PbO Nanoclusters in Solution". In: *Chemistry of Materials* 11.11 (1999), pp. 3037–3043. DOI: 10.1021/cm9810990. URL: https://doi.org/10.1021/cm9810990.

[138] Austin Nevin et al. "Time-Resolved Photoluminescence Spectroscopy and Imaging: New Approaches to the Analysis of Cultural Heritage and Its Degradation". In: *Sensors* 14.4 (2014), pp. 6338–6355. ISSN: 1424-8220. DOI: 10.3390/s140406338. URL: https://www.mdpi.com/1424-8220/14/4/6338.

[139] Velaga Srihari et al. "Raman Scattering of Cadmium Oxide: in B1 Phase". In: *AIP Conference Proceedings* 1349.1 (2011), pp. 845–846. DOI: 10.1063/1.3606122.

[140] A.K. Kumar S.; Ojha. "Synthesis, characterizations and antimicrobial activities of well dispersed ultra-long CdO nanowires. " In: *AIP Adv.* 3.052109 (2013). URL: https://doi.org/10.1063/1.4804930..

[141] Z. V. Popović et al. "Infrared and Raman Spectra of CdO". In: *physica status solidi (b)* 165.2 (1991), K109–K112. DOI: https://doi.org/10.1002/pssb.2221650249. eprint: https://onlinelibrary.wiley.com/doi/pdf/10.1002/pssb.

2221650249. URL: https://onlinelibrary.wiley.com/doi/abs/10.1002/pssb.2221650249.

[142] T. T. K. Chi et al. "Off-resonance Raman analysis of wurtzite CdS ground to the nanoscale: structural and size-related effects". In: *Journal of Raman Spectroscopy* 42.5 (2011), pp. 1007–1015. DOI: https://doi.org/10.1002/jrs.2793. eprint: https://analyticalsciencejournals.onlinelibrary.wiley.com/doi/pdf/10.1002/jrs.2793. URL: https://analyticalsciencejournals.onlinelibrary.wiley.com/doi/abs/10.1002/jrs.2793.

[143] Francesca Rosi et al. "UV–Vis-NIR and micro Raman spectroscopies for the non destructive identification of Cd1xZnxS solid solutions in cadmium yellow pigments". In: *Microchemical Journal* 124 (2016), pp. 856–867. ISSN: 0026-265X. DOI: https://doi.org/10.1016/j.microc.2015.07.025. URL: https://www.sciencedirect.com/science/article/pii/S0026265X1500171X.

[144] Guillaume Falgayrac, Sophie Sobanska, and Claude Brémard. "Heterogeneous microchemistry between $CdSO_4$ and $CaCO_3$ particles under humidity and liquid water". In: *Journal of Hazardous Materials* 248-249 (2013), pp. 415–423. ISSN: 0304-3894. DOI: https://doi.org/10.1016/j.jhazmat.2013.01.029. URL: https://www.sciencedirect.com/science/article/pii/S0304389413000472.

[145] Laura Giacopetti et al. "First principles study of the optical emission of cadmium yellow: Role of cadmium vacancies". In: *AIP Advances* 8.6 (2018), p. 065202. DOI: 10.1063/1.5018512.

[146] H.G.M. Schönemann A.; Edwards. "Raman and FTIR microspectroscopic study of the alteration of Chinese tung oil and related drying oils during ageing". In: *Anal. Bioanal. Chem.* (2011). DOI: doi:10.1007/s00216-011-4855-0.

[147] Seungsoo Kim et al. "In vivo three-dimensional spectroscopic photoacoustic imaging for monitoring nanoparticle delivery". In: *Biomed. Opt. Express* 2.9 (Sept. 2011), pp. 2540–2550. DOI: 10.1364/BOE.2.002540. URL: https://opg.optica.org/boe/abstract.cfm?URI=boe-2-9-2540.

[148] Srivalleesha Mallidi et al. "Multiwavelength Photoacoustic Imaging and Plasmon Resonance Coupling of Gold Nanoparticles for Selective Detection of Cancer". In: *Nano Letters* 9.8 (2009). PMID: 19572747, pp. 2825–2831. DOI: 10.1021/nl802929u. URL: https://doi.org/10.1021/nl802929u.

[149] Jie Hui et al. "Bond-selective photoacoustic imaging by converting molecular vibration into acoustic waves". In: *Photoacoustics* 4.1 (2016), pp. 11–21. ISSN: 2213-5979. DOI: https://doi.org/10.1016/j.pacs.2016.01.002. URL: https://www.sciencedirect.com/science/article/pii/S2213597916300027.

[150] "Initial results of in vivo non-invasive cancer imaging in the human breast using near-infrared photoacoustics". English. In: *Optics express* 15.19 (2007), pp. 12277–12285. ISSN: 1094-4087. DOI: 10.1364/OE.15.012277.

[151] Liming Nie and Xiaoyuan Chen. "Structural and functional photoacoustic molecular tomography aided by emerging contrast agents". In: *Chem. Soc. Rev.* 43 (20 2014), pp. 7132–7170. DOI: 10.1039/C4CS00086B. URL: http://dx.doi.org/10.1039/C4CS00086B.

[152] Alice Dal Fovo et al. "First combined application of photoacoustic and optical techniques to the study of an historical oil painting". In: *European Physical Journal Plus* 136 (July 2021). DOI: 10.1140/epjp/s13360-021-01739-8.

[153] George J. Tserevelakis et al. "Revealing Hidden Features in Multilayered Artworks by Means of an Epi-Illumination Photoacoustic Imaging System". In: *Journal of Imaging* 7.9 (2021). ISSN: 2313-433X. DOI: 10.3390/jimaging7090183. URL: https://www.mdpi.com/2313-433X/7/9/183.

[154] George J. Tserevelakis et al. "Hybrid autofluorescence and photoacoustic label-free microscopy for the investigation and identification of malignancies in ocular biopsies". In: *Opt. Lett.* 45.20 (Oct. 2020), pp. 5748–5751. DOI: 10.1364/OL.403435. URL: https://opg.optica.org/ol/abstract.cfm?URI=ol-45-20-5748.

[155] George J. Tserevelakis et al. "Photoacoustic imaging methodology for the optical characterization of contact lenses". In: *Opt. Lett.* 42.20 (Oct. 2017), pp. 4111–4114. DOI: 10.1364/OL.42.004111. URL: https://opg.optica.org/ol/abstract.cfm?URI=ol-42-20-4111.

[156] Alice Dal Fovo et al. "Combined photoacoustic imaging to delineate the internal structure of paintings". In: *Opt. Lett.* 44.4 (Feb. 2019), pp. 919–922. DOI: 10.1364/OL.44.000919. URL: https://opg.optica.org/ol/abstract.cfm?URI=ol-44-4-919.

[157] George Tserevelakis et al. "Photoacoustic imaging reveals hidden underdrawings in paintings". In: *Scientific Reports* 7 (Apr. 2017), p. 747. DOI: 10.1038/s41598-017-00873-7.

[158] George J. Tserevelakis et al. "Non-invasive photoacoustic detection of hidden underdrawings in paintings using air-coupled transducers". In: *Ultrasonics* 98 (2019), pp. 94–98. ISSN: 0041-624X. DOI: https://doi.org/10.1016/j.ultras.2019.06.008. URL: https://www.sciencedirect.com/science/article/pii/S0041624X19300666.

[159] George J. Tserevelakis et al. "Combined multiphoton fluorescence microscopy and photoacoustic imaging for stratigraphic analysis of paintings". In: *Opt. Lett.* 44.5 (Mar. 2019), pp. 1154–1157. DOI: 10.1364/OL.44.001154. URL: https://opg.optica.org/ol/abstract.cfm?URI=ol-44-5-1154.

[160] Antonina Chaban et al. "Agar Gel as a Non-Invasive Coupling Medium for Reflectance Photoacoustic (PA) Imaging: Experimental Results on Wall-Painting Mock-Ups". In: *Journal of Imaging* 8 (Aug. 2022), p. 235. DOI: 10.3390/jimaging8090235.

[161] George J. Tserevelakis et al. "Uncovering the hidden content of layered documents by means of photoacoustic imaging". In: *Strain* 55.2 (2019). e12289 STRAIN-1393.R1, e12289. DOI: https://doi.org/10.1111/str.12289. eprint: https://onlinelibrary.wiley.com/doi/pdf/10.1111/str.12289. URL: https://onlinelibrary.wiley.com/doi/abs/10.1111/str.12289.

[162] George J. Tserevelakis et al. "On-line photoacoustic monitoring of laser cleaning on stone: Evaluation of cleaning effectiveness and detection of potential damage to the substrate". In: *Journal of Cultural Heritage* 35 (2019). Modern and Contemporary Art, pp. 108–115. ISSN: 1296-2074. DOI: https://doi.org/10.1016/j.culher.2018.05.014. URL: https://www.sciencedirect.com/science/article/pii/S1296207417308105.

[163] Athanasia Papanikolaou et al. "Development of a hybrid photoacoustic and optical monitoring system for the study of laser ablation processes upon the removal of encrustation from stonework". In: *Opto-Electronic Advances* 3 (Feb. 2020). DOI: 10.29026/oea.2020.190037.

[164] H.-I. W. Lihong V. Wang. *Biomedical Optics: Principles and Imaging*. Wiley Online Library, 2007.

[165] George Tserevelakis, Paraskevi Pouli, and Giannis Zacharakis. "Listening to laser light interactions with objects of art: a novel photoacoustic approach for diagnosis and monitoring of laser cleaning interventions". In: *Heritage Science* 8 (Oct. 2020), p. 98. DOI: 10.1186/s40494-020-00440-w.

[166] L. V. Wang and Hsin-I Wu. *Biomedical Optics: Principles and Imaging*. 2012.

[167] C. Conti et al. "Subsurface analysis of painted sculptures and plasters using micrometre-scale spatially offset Raman spectroscopy (micro-SORS)". In: *Journal of Raman Spectroscopy* 46 (Mar. 2015). DOI: 10.1002/jrs.4673.

[168] Alessandra Botteon et al. "Exploring street art paintings by microspatially offset Raman spectroscopy". In: *Journal of Raman Spectroscopy* 49 (July 2018). DOI: 10.1002/jrs.5445.

[169] Notburga Gierlinger and Manfred Schwanninger. "The potential of Raman microscopy and Raman imaging in plant research". In: *Spectroscopy-an International Journal* 21 (Jan. 2007), pp. 69–89. DOI: 10.1155/2007/498206.

[170] D. Chiriu et al. "Beyond the surface: Raman micro-SORS for in depth non-destructive analysis of fresco layers". In: *Microchemical Journal* 153 (2020), p. 104404. ISSN: 0026-265X. DOI: https://doi.org/10.1016/j.microc.2019.104404. URL: https://www.sciencedirect.com/science/article/pii/S0026265X19325172.

[171] Claudia Conti et al. "Contrasting confocal XRF with micro-SORS: a deep view within micrometric painted stratigraphy". In: *Anal. Methods* 10 (31 2018), pp. 3837–3844. DOI: 10.1039/C8AY00957K. URL: http://dx.doi.org/10.1039/C8AY00957K.

[172] Nicolae Buzgar and Andrei Apopei. "The Raman study of certain carbonates". In: *Anal. Şt. Univ. „Al. I. Cuza" Iaşi* LV (Jan. 2009), pp. 97–112.

[173] Iker Marcaida et al. "In situ non-invasive multianalytical methodology to characterize mosaic tesserae from the House of Gilded Cupids, Pompeii". In: *Heritage Science* 7 (Jan. 2019), p. 3. DOI: 10.1186/s40494-019-0246-1.

[174] Vanessa Antunes et al. "Characterization of gypsum and anhydrite ground layers in 15th and 16th centuries Portuguese paintings by Raman Spectroscopy and other techniques". In: *Journal of Raman Spectroscopy* 45 (May 2014). DOI: 10.1002/jrs.4488.

[175] Daniele Chiriu, Carlo Carbonaro, and P.C. Ricci. "Defect Related Emission in Calcium Hydroxide: The Controversial Band at 780 cm1". In: *Crystals* 10 (Apr. 2020), p. 266. DOI: 10.3390/cryst10040266.

5 APPENDIX

5.1 PUBLICATIONS

1. Francesca Assunta Pisu et al. "Defect Related Emission in Calcium Hydroxide: The Controversial Band at 780 cm^{-1}". In: Crystals 10.4 (2020). issn: 2073-4352. doi: 10.3390/cryst10040266 ;

2. Francesca Assunta Pisu et al. "Fresco Paintings: Development of an Aging Model from 1064 nm Excited Raman Spectra". In: Crystals 11.3 (2021). issn: 2073-4352. doi: 10.3390/cryst11030257

3. Francesca Assunta Pisu et al."Degradation of CdS Yellow and Orange Pigments: A Preventive Characterization of the Process through Pump–Probe, Reflectance, X-ray Diffraction, and Raman Spectroscopy". In: Materials(2022), doi: 10.3390/ma15165533;

4. Francesca Assunta Pisu et al. "Transient absorption study on Red Vermilion darkening in presence of chlorine ions and after UV exposure". In: analitical Chemistry, (2022), doi: 10.1016/j.jphotochem.2022.114291;

5. Daniele Chiriu, Marco Pala, Francesca Assunta Pisu, Carlo Ricci, Carlo Maria Carbonaro"Time through colors: A kinetic model of red vermilion darkening from Raman spectra", In: Dyes and pigments(2020), doi: 10.1016/j.dyepig.2020.108866

6. Daniele Chiriu, Jonathan Desogus, Francesca Assunta Pisu"Beyond the surface: Raman micro-SORS for in depth non-destructive analysis of fresco layers"; In: Micorchemical Journal(2020); doi: 10.1016/j.microc.2019.104404.

7. Daniele Chiriu, Pisu Francesca Assunta, Pier Carlo Ricci, Carlo Maria Carbonaro"Application of Raman Spectroscopy to Ancient Materials: Models and Results from Archaeometric Analyses"; In: Materials(2020); doi: 10.3390/ma13112456

8. Carlo Nocco, Francesca Assunta Pisu, Daniele Chiriu, Depalmas Anna, Sergio A. B. Lins, Antonio Brunetti"Multispectral analysis of miniature nuragic bronze flasks"; In: Heritage(2021); doi:10.3390/heritage4030095.

9. Francesca Assunta Pisu et al. “Cadmium yellow pigments in oil paintings: optical degradation studies”; submitted to “Heritage”

10. Francesca Assunta Pisu et al. “ Stratigraphy of ancient frescoes: a new approach with photoacoustic and SORS imaging “; In: “Journal of Imaging”(2023), doi: 10.3390/jimaging9010016.

5.2 CONFERENCES AND SYMPOSIA

- E-MRS Spring Meeting, Talk contribution: “Studies on CdS pigment degradation through pump-probe, reflectance, and Raman spectroscopy”
- MetroArcheo2022, Talk contribution: “Degradation study of pigments through transient absorption and colorimetry”
- EDUC Cultural and Heritage Event of Research Networking, Nanterre, France.

5.3 INTERNATIONAL EXPERIENCES

- 3 months at The Royal Institute for Cultural Heritage-KIK-IRPA (Bruxelles), under the supervision of the lead of painting laboratory Dott. Steven Saverwyn.
- 3 months at the Foundation for Research and Technology - Hellas, FORTH centre (Crete), under the supervision of Dott. George Tserevelakis.

Acknowledgements

I would like to thank INFN for the financial support of this PhD.
Special thanks go to my supervisor D. Chiriu and the entire Treetop group for guidance and support.
Further thanks go to the FORTH research group and the KIK IRPA painting laboratory research group for giving me the opportunity during the PhD to work at their laboratories and increasing my knowledge on diagnostics.